DEFORMATION-INDUCED BULK INVAR AND ELINVAR EFFECTS IN THERMOELASTIC SHAPE-MEMORY ALLOYS

A Dissertation

by

DOMINIC F. GEHRING

Submitted to the Office of Graduate and Professional Studies of
Texas A&M University
in partial fulfillment of the requirements for the degree of

DOCTOR OF PHILOSOPHY

Chair of Committee,	Ibrahim Karaman
Committee Members,	Raymundo Arroyave
	Karl T. Hartwig
	Lin Shao
Head of Department,	Ibrahim Karaman

December 2020

Major Subject: Materials Science and Engineering

Copyright 2020 Dominic Gehring

ABSTRACT

Thermal expansion control is key to further optimization of systems with large heat gradients or changes in temperature, and where extreme precision is required. Manipulation of this property in materials has traditionally been limited as thermal expansion responds mainly to significant composition changes. Various special exceptions including Invar alloys provide some ability to address specific requirements. Discovery of giant thermal expansion anisotropy is a significant new development, enabling alloys with tailorable thermal expansion properties. Measurements at the crystalline scale through x-ray diffractography has shown that this occurs in thermoelastic martensites in the NiTi, TiNb, and NiTiPd families. The directionality of the various expansion rates in the crystal structure can be predicted through the lattice mismatch between martensite and its parent phase. This anisotropic crystalline response can be harnessed by use of deformation to produce reorientation and net alignment (texture) of martensitic polycrystals.

Examination of bulk material has demonstrated directional linear thermal expansions ranging from -30 to +40 ppm in TiNb alloy, -15 to +30 ppm in NiTi alloy, and -6 to +13 ppm in NiTiPdTa alloy between 0 and 100 °C. The strength of expansion response in the bulk material is dependent on the degree of texturing; this allows for selection of specific expansion rates via mechanical processing. Further examination also shows a strong directional effect on the elastic properties in the deformed material, which is driven at least partly by these same mechanisms. Extension to nickel-rich NiTi alloy revealed that this same anisotropic behavior can be retained in a largely austenitic alloy, with the additional effect of generating a net Elinvar effect up to 300 °C. With development of the optimal design approaches for these alloys, the potential to revolutionize accommodation of thermal expansion and elastic properties in materials may be realized.

ACKNOWLEDGEMENTS

My deepest gratitude to my graduate advisor, Dr. Karaman, for his advice and tolerance, and for his long time support despite the circumstances which have encroached over the course of this time.

Likewise, my appreciation for the unending faith of my parents cannot be expressed.

I thank Dr. Timothy Brown for his long-time collaboration in keeping each other sane.

To all others with whom I have collaborated or socialized over the years, including many persons of my lab group and other members of the A&M community, my thanks are extended in making my time here more interesting and productive.

CONTRIBUTORS AND FUNDING SOURCES

Contributors

This work was supervised by a dissertation committee consisting of Professor I. Karaman [advisor] and Professors R. Arroyave and K.T. Hartwig of the Department of Materials Science and Engineering and Professor L. Shao of the Department of Nuclear Engineering.

Funding Sources

There are no outside funding contributions to acknowledge related to the research and compilation of this document.

NOMENCLATURE

CTE	Coefficient of Thermal Expansion
NTE	Negative Coefficient of Thermal Expansion
PTE	Positive Coefficient of Thermal Expansion
ZTE	Zero Coefficient of Thermal Expansion
A_S	Austenite Start Temperature
A_F	Austenite Finish Temperature
M_S	Martensite Start Temperature
M_F	Martensite Finish Temperature
SMA	Shape Memory Alloy
MT	Martensitic Transformation
iPF	Inverse Pole Figure
EvT	Elastic Modulus-Temperature Response
EDM	Electro-discharge Machining
WQ	Water Quenching
UHP	Ultra-high Purity Argon
XRD	X-ray Diffraction
TMA	Thermo-mechanical Analyzer
CTEAS	Coefficient of Thermal Expansion Analysis Suite
DSC	Differential Scanning Calorimetry
MAUD	Materials Analysis using Diffraction
EPS	Equivalent Plastic Strain

2Θ	Two-theta
LS	Linear-strain Correction Approach

TABLE OF CONTENTS

LIST OF FIGURES

Page

Page

Page

Page

LIST OF TABLES

CHAPTER I

INTRODUCTION

This chapter introduces the need and significance of the development of anisotropically-varying (anvar) alloys. The questions of thermal expansion and elastic responses to temperature are introduced, as well as the mechanics of previously known Invar and Elinvar alloys. The response to deformation of anvar alloys will be introduced with the fundamental idea of tailorable thermal expansion/stiffness materials. The objectives of the present study are stated, and an outline of the experimental work carried out to meet these objectives is given at the end of this chapter.

1.1 Motivation

The easiest way to simply any calculation is to assume that portions remain constant regardless of condition. This is a common practice for a variety of situations in both scientific and engineering disciplines; a number of nominally minor considerations are left out of the impending calculation on the convenience that either they are irrelevant or of insufficient difference to be important. For example, it is common to assume that fluid interfaces in systems are constant rather than reactive, or that a heat or mass flow remains in perfect steady state without variance. In the context of education and theoretical exercises this is perfectly acceptable; however as work transitions from simple conceptualization into actual design and development, and especially when confronting applications which demand precision, then such considerations may invalidate whole swaths of work if not addressed.

In materials engineering, two easily assumed areas of 'constancy' which become problematic in real terms relate to the evolution of atomic bonding as a function of ambient temperature. In the simple energy well concept of bonding [1], it is understood that the distance between atoms is inversely proportional to the total energy constrained by the bond between them, which in turn influences how strongly they interact with each other. The concept of 'temperature' refers simply to the sum total of the kinetic energy imparted to atoms within a system; an increase in temperature is associated with a proportional increase in this vibrational kinetic energy. When heat is added to the system and the temperature increases, this additional energy contributes to an increase in the bonding distance, which weakens the interactions between bonded atoms. The overall impact in macroscale material behavior is expressed in the near-universal tendency to gradually grow in dimension and decrease in stiffness as the temperature within the material increases.

Both changes will typically occur with exceedingly small magnitudes, on the order of millionths to thousandths of the base value per degree centigrade and can often be discounted in applications with sufficiently open tolerances. These small changes however become consequential in more demanding applications, especially in situations which impart large temperature differences, rapid temperature gradients, or where extremely fine tolerances are required. Areas of application readily spring to mind in the aerospace industry, especially when looking towards the requirements for enabling future hypersonic aircraft; the optics industry, where tolerances are very often especially small to prevent distortion; and in electronics, where large temperature differences can be found in small spaces. In both these examples and the broader industry materials which either themselves or in partnership with others display the needed invariance have long been in demand. The need for such invariant behavior is now seemingly on course to only become more necessary than ever as technology continues to advance, and applications become more demanding and precise so as to extract maximum possible performance.

The possession of material which shows the absolute thermal expansion invariance (invar) or elastic modulus invariance (elinvar) with temperature is surprisingly old among the advanced materials science topics, with the FeNi-based Invar alloy discovered in the 1890s, and subsequent FeNiCr Elinvar alloy descended from the Invar discovery first reported in the 1920s. Thus, the availability of such material has long been known, yet these classic examples suffer from shortcomings which have always held the door open for participation of materials which demonstrate superior behavior broadly or in some specific aspect. The main problems which limit both alloys are their high dependence on chemistry to elicit their desired properties, their small overall range of tailorable expansion rates, and their relatively low maximum working temperature ceiling.

An additional consideration which offers intriguing possibilities for design and application is the relative, rather than absolute, invariance in a system. Here, mixing parts with differing properties can allow for a net effect through a composite which is itself invariant even when the parts are not. It is in this realm that several newer additions to the temperature control aspect of materials science have been introduced. Examples in this field include ceramics which contract due to bond rotation, such as ZrW_2O_8, and carbon composites, which can exhibit near-zero and slightly negative expansion along certain directions due to the anisotropy of carbon bond interactions. Despite the good performance of these potential ingredients, the overall range of possible expansion rates which they contribute to remains narrow and this limits the number of invariant scenarios which they are able to contribute to.

An opposite approach is to create compliant networks where the difference in thermal expansion of components can with specifically engineered application of geometry yield a desired expansion rate. This normally comes with the tradeoff of compromising the overall strength of the system or sacrificing overall volume to create the necessary leverage and can often require complicated assembly procedures.

Due to their nature either as composites or as networks, many of the most recent approaches to thermal expansion control which have arisen are normally of relatively complex construction. This leaves room for a material which exhibits good absolute or relative invariant behavior to create a new niche in this field by being generated through more straightforward processing pathways.

1.1.2 Invar and Elinvar Mechanisms

The true explanation for the cause of the Invar effect observed in FeNi and FePt alloys is still a matter of some debate [2, 3]. The most commonly accepted explanation for FeNi appears however to be the one laid down by R. J. Weiss in 1963 [4]. In in FeNi, the gamma-FCC structure becomes dominant and manifests in two distinct magnetic configurations: the antiferromagnetic γ_1 and the ferromagnetic γ_2 [5]. While the γ_2 phase exists at the higher energy level, the actual difference in energy between the two phases is remarkably small (approximately 0.0355 eV) and requires only a migration of one electron to a new shell configuration to achieve a switch, without the need for a first-order transformation.

The Weiss Invar explanation relies on a small quirk that evolves in these two configurations: the γ_1 phase is 8% smaller in volume than the opposing γ_2 phase. The addition of the Ni element can stabilize the γ_2 phase so that this, despite being the larger-volume and higher-energy configuration normally, is the predominant configuration which exists in this alloy when thermal energy is at minimum at 0 K. What then occurs as temperature increases is a gradually increasing excitation of the γ_1 phase in opposition to the γ_2 phase, allowing for a larger fraction of this γ_1 phase to be present at higher temperatures. As the γ_1 phase comes into being, its accompanying lattice differential is expressed by locally shrinking the material around it. For a range of Ni content in this system the thermal expansion is lower than expected due to the contributions from some excitation. In the Invar alloy material (the classic example being $FeNi_{36}$), this rate of excitation switching pegs remarkably close to the rate of anharmonic growth, resulting in the near-zero rate of overall expansion. The opposite case somewhat reinforces the impact of this magnetovolume effect: when Ni alloying additions are not sufficient to stabilize the γ_2 phase, the thermal excitations are instead in the direction from γ_1 to γ_2 and the resulting expansion rates in these materials are actually abnormally high.

It should be noted that due to the postulated effect being attributed to electron state switching and spontaneous atomic scale switching, that the model proposed by Weiss remains phenomenological; the existence of the two states and their volume differences has not actually been proven experimentally. This has led to subsequent models since being introduced which attempt to better allow for calculation of the specific phenomena involved. However, for all of its lack of experimental verification, it does stand that the Weiss model does hold up well at predicting the general trend of behavior in Invar alloy. One of the main points which is predicted by the thermal excitation approach is the existence of some saturation point where excitation will cease to occur; in Invar this happens near 130 °C, at which point the material transitions to a normal rate of expansion for an iron alloy.

Application of alloying elements appears to have significant effects on the overall switching behavior. The addition of small amounts of Co to Invar alloy seems to encourage a slightly greater level of thermal excitation of the small-volume phase, reducing the already low expansion; this is termed Super Invar alloy. In another case laid out by Guilleaume in 1920, adding 36 wt% Ni and 12 wt% Cr to iron produces an alloy which does present with moderate rates of thermal expansion, but instead exhibits near perfect invariance of elastic modulus to a similar maximum temperature; this is the Elinvar alloy family [6, 7]. It can be supposed that the explanation for elinvar behavior in the Weiss theory again relates to a modification of the thermal excitation rate; normal invar alloy actually shows an increase in elastic modulus with temperature in the same region. This is to be expected; the shrinking of bond distance logically should also result in stronger interaction. It may be supposed that the role of Cr additions in elinvar alloy is to moderate the excitation rate so as to produce the correct sampling ratio to offset the normal anharmonic stiffness loss.

1.1.3 Deformation Response in Shape-Memory Martensites

Shape-memory alloys are characterized by the solid-state transformation between a higher-symmetry phase (the austenite) and a corresponding lower-symmetry phase (the martensite), often with the higher-symmetry phase energetically favored at higher temperatures than the martensite. In addition to the original NiTi alloy, shape-memory behavior has been identified in a number of systems, including β-Ti alloy, CoNi, CuAl, NiMn, and ZrCu-based configurations [8]. What has defined 'shape memory' material is the ability for specific forms of these alloys to recover some or all of the applied plastic deformation upon heating, creating a rather unique class of smart materials.

The basis for this strain recovery is founded in the nature of how this plastic deformation is accommodated within the material. The solid-state transition of austenite into martensite results in the creation of oriented variants of specific directions relative to the parent cell. These variants can form in one of two ways [9]. In the case where the energy of formation for martensite is imparted through stress (the stress-induced martensite), the local strain field renders it so that the martensite naturally aligns itself relative to the stress tensor; variants where the elongation of the martensite occurs relative to the austenite matrix in the tension direction, for example, will be favored and grow in the resulting material. This results in a sample which will be elongated relative to the original austenite matrix, and upon heating the restoration to the higher-symmetry shape would result in significant contraction along the direction of the tensile stress until the material returned to its original shape.

The ability for one variant to be favored over the formation of another is enabled by the presence of variant twinning; various orientations of martensite are connected to each other by twin boundaries, often within the same original grain. In unstressed thermal transformations, the martensite which forms in a given volume will seek to minimize the overall stress which is generated by the shape change which occurs during the transformation. As a monolithic change to one orientation configuration would result in large shape changes and resulting stresses, the tendency for martensite is to instead pair with other orientations via twin boundaries and then grow in multiple compatible orientations instead. When observing unstressed transformation grains of austenite will often be replaced by rows of distinct martensite variants separated by twin boundaries. This random distribution of different variants in the unstressed condition is referred to self-accommodated martensite.

In response to the application of stress onto the material, self-accommodated martensite is able to freely accommodate plastic deformation without requiring plastic slip through the process known as detwinning. In this process, variants which are favored by the applied stress (let us reuse the long orientation being favored in tension, as before) grow by the reorientation of the twinned variants which are of less favorable configuration. This results in the migration of the twin boundaries as the variants grow and shrink in proportion, until the twin boundaries are no longer able to move easily through compatible matrix. This is the second method of creating a favored variant orientation in material and will result in a net texturing after deformation before recovery.

There are a number of applications in shape-memory where variant orientation is of great interest [10-12]. Done with sufficient care and proper material, it is possible to create a single crystal of oriented martensite, as has been demonstrated in CuZnAl and CuAlBe alloys [9]. Even in polycrystalline alloy, properly induced deformation can strengthen the strain response of the material during recovery by orienting the variants with the largest shape change relative to the direction of response. However, the material limits must be well understood, as reorientation does have a limit before either the twin boundaries are unable to move further or all other variants have been exhausted. At this point, it becomes necessary for any further deformation to be accommodated by slip and dislocation movement, which can impair transformation recovery.

1.1.4 Anisotropically-varying (Anvar) Alloys

Thermal expansion in alloys, normally between 6 and 30 parts per million (ppm, or $10^{-6}\ {}^{m}/_{m\text{-}K}$), results from the range of expansion common to most metallic elements. Such behavior is normally quite symmetric because of many metals possessing cubic crystal structure, with some small anisotropy observable in hexagonal metals such as titanium or magnesium [13, 14]. As thermal expansion is most strongly affected by chemical composition in metals, few tools beyond Invar have traditionally been available to radically change the expansion of a given alloy system or extend the expansion range of alloys in general.

In metallic alloys, a new class of materials has recently been discovered that exhibit anisotropy in the lattice level CTEs. In our study published in 2016 [15], we demonstrated that this anisotropy can be exploited in polycrystals through crystallographic texturing upon deformation processing. This yields a tailorable bulk thermal expansion with a staggering thermal expansion and contraction ranges, projected to achieve any value between -40 and +50 ppm in bulk material depending on the alloy type and ability to control crystallographic texture in polycrystals.

The common feature of these metallic alloys with anisotropic CTE appears to be the fact that they all undergo martensitic transformation, and that the lower symmetry martensite phase possesses the anisotropic CTE tensor. Some of these martensitic materials are shape memory alloys (SMAs) such as NiTi, NiTiPd, CoNiGa, NiMnGa, and TiNb alloys, while others include equally martensitic materials with thermoelastic transformations such as elemental α-uranium and the perovskite lead titanate. The underlying physics responsible for anisotropic CTE, specifically in martensitic materials, has not been fully understood.

The mechanism, whatever its form, appears to manifest in a manner similar to the mechanism described above in the Invar alloys with the addition of a directional component to account for the non-cubic symmetry of the lower-temperature phase. The comparison of the lattice parameter mismatch between austenite and martensite phases can be used to predict the sign and relative magnitude of the thermal expansion rate for any given direction of the martensite lattice. If the interatomic distance along a given lattice vector in martensite is greater than the interatomic distance along the equivalent vector in austenite the martensite lattice along this particular direction is observed to contract when heated. Likewise, when the martensite lattice is shorter than that of the equivalent austenite direction, then the martensite displays large expansion during heating. These samples being tested are martensitic and below the A_s temperature, indicating transformation is not the responsible mechanism.

In polycrystals, use of thermomechanical processing to control crystallographic texture allows for exploitation of this lattice CTE anisotropy in bulk samples. Martensite phases can easily be textured in polycrystals through martensite variant reorientation/detwinning under low applied strain levels, often with little or no accompanying deformation slip. This was demonstrated in our initial study on this topic. In the proof-of-concept, tensile deformation of a polycrystalline NiTiPd SMA led to sufficient martensite reorientation for the thermal expansion along the tensile axis to change from 14 ppm to -3 ppm after 5% axial deformation had been achieved. In materials with sufficient ductility, simple deformation processing techniques such as rolling and drawing are capable of producing the necessary deformation for sufficient crystallographic texturing, making fabrication of anisotropically varying (anvar) CTE alloys easily scalable. The was again shown as a proof-of-concept by rolling of $TiNb_{22}$ at% alloy, and was further demonstrated in $Ni_{50.6}Ti$ alloy by another group after publication of our study [16]. These anvar alloys appear to fully fill the previously noted niche available for a material which demonstrates either absolute or relative invar behavior, while requiring relatively simple preparation.

1.2 Objectives

The responses described in Section 1.1.4 illustrate a new and exciting class of materials behavior which remains to be explored, and as such a number of unresolved questions remain to be answered before a full and complete picture can be considered available. The purpose of this work is to more completely explore the underlying crystalline thermal expansion anisotropy as a function of composition and thermomechanical processing applied, and how the application of deformation affects this responding evolution in the bulk material behavior regarding CTE and elastic modulus. It is hypothesized that much of these behaviors can be directly related to each other through the relative alignment (texture) of the martensite in polycrystalline materials.

The overall objectives of the current study are:

1. The underlying properties of the crystalline martensite should be understood in regard to the thermal expansion anisotropy. To measure this, the martensitic lattice parameters, strain change with temperature should be measured or estimated. To examine the lattice parameters and strain evolution, X-Ray diffraction should be performed on samples of material. Different SMA alloy systems (NiTi, NiTiPd, TiNb) should be studied to examine what changes occur due to chemistry, ordering, and crystal structure. Beyond chemical influences, pre-strained tension samples and highly rolled samples shall also be examined in order to determine if there are any significant effects which are imparted onto the crystalline behavior due to introduction of slip and dislocations.
2. The bulk thermal expansion response of the various materials to deformation should also be examined. This should be done via tension and rolling deformation methods to

examine both at small levels of uniaxial strain and large levels of multiaxial compression in a dynamic environment to determine how the deformation response contrasts with itself under such wildly different conditions. Also of interest is the rate of change in the CTE and any changes in the first derivative values in CTE change with amount of deformation to glean information regarding the modes of deformation and response which are providing the strongest contributions within a given deformation range.

3. As the texture is hypothesized to be a central determinant in the overall material behavior, then naturally a full or as full as possible understanding of the texture and texture evolution should be sought in the material being studied. Texture shall be examined using X-ray diffraction at various angles with the data being further analyzed via software to determine the representative textures found in the materials. Examination of the texture against crystalline and bulk CTE anisotropy will indicate whether the texture correctly links the various scale responses.

4. Elastic anisotropy is known to exist in shape-memory martensites [17-23], and it is expected that as a natural evolution of orienting the CTE anisotropy that elastic modulus values along given directions will also evolve as a function of deformation. With a sufficiently strong correlation, it may also be tuned in a manner similar to that of CTE, which has not been definitely shown previously. Thus, this evolution and its connection to texture are examined for this work by extending the methodology used to examine the CTE in tension deformation. Responses to rolling deformation are also examined via tension for previously rolled materials.

5. As the stiffness of a bond is correlated to the distance between nearest neighbors and the existence of thermal expansion anisotropy would imply that the nearest neighbor distance should change in abnormal ways [24, 25], it is expected that deformation should also have a notable effect on the EvT response in material. Attempts have been made by outside groups, some successful, at generating elinvar-type alloys in SMA by arresting the transformation, in essence aiming to generate a strain glass through chemical doping [26]. The stiffness response change as a function of temperature will also be measured by extension of the tension methodology beyond CTE during iterated deformation, and by examination of rolled material to determine whether significant changes are induced by said deformation.

6. Continuing discussion in literature regarding the nature and properties of GUM metals and strain glasses leave open the possibility that the anisotropy interactions of the martensitic nanodomains with the majority austenite play a role in their behaviors [26-28]. This is especially true under deformation, where ease of reorientation and slip of the austenitic matrix may allow for extremely high orientation of the nanodomains in the material. This directionality should play a direct role in the anisotropy of CTE seen in deformed GUM metal. Examination of whether this martensite response extends beyond fully-martensitic materials can be done by applying significant rolling deformation to austenitic nickel-rich NiTi alloys and examining the resulting bulk responses in both CTE and stiffness as a function of temperature and applied deformation amount.

With these objectives, the outline of this dissertation is as follows:

Chapter II: Introduction of the direct influence for this study containing experimental evidence for the tailorable thermal expansion effect and elucidation on the fundamental principles for the thermal excitation method used as the phenomenological model for the underlying martensite behaviors examined here.

Chapter III: Experimental methods and materials that are used in this study.

Chapter IV: Investigation of the tensile deformation response by NiTi. Here the underlying crystalline lattice strain change to temperature is examined directly as a function of both composition and applied prestrain to determine the effects on underlying martensitic CTE. In tension the fundamental mechanical properties in response to deformation are examined, followed by measurements of the resulting CTE and elastic properties along the tension direction as a function of deformation.

Chapter V: The same examinations are applied for NiTiPd alloy to contrast the crystalline CTE and bulk deformation responses due to the changes induced by the introduction of alloying elements.

Chapter VI: Investigation of the tensile deformation response by TiNb. Here the underlying crystalline lattice strain change to temperature is examined directly as a function of both composition and applied prestrain to determine the effects on underlying martensitic CTE. In tension the fundamental mechanical properties in response to deformation are examined, followed by measurements of the resulting CTE along the tension direction as a function of deformation. Further examination of the texture determines the validity of the multiscale connection and prediction of the orthonormal CTE as a function of deformation is provided.

Chapter VII: An examination of the bulk orthonormal CTE response in NiTi as a function of applied rolling reduction, and investigation of the potential of higher maximum working temperatures via martensite stabilization.

Chapter VIII: Examination of TiNb selected for rolling to verify batch-to-batch responses relative to material used in Chapter VI, followed by measurement of the orthonormal CTE response to rolling deformation and texture resulting from such. Additional results are provided regarding the responses to higher-temperature processing and thermal cycling stability.

Chapter IX: An investigation of the response in nickel-rich NiTi alloy after significant rolling deformation regarding its phase and calorimetric properties, followed by examination of its planar CTE and elastic properties as a function of temperature applied to the sample.

Chapter X: Main conclusions

Chapter XI: Summary of future directions and approaches

CHAPTER II

DIRECT BACKGROUND*

As this particular topic is relatively new, the main background writings which inform this work are the relevant portions of Dr. James A. Monroe's doctoral dissertation [29] and the resulting summary of the tailorable thermal expansion effect coauthored with the same person published in 2016 [15]. To provide this background information, the latter is included below to provide context:

2.1 Tailorable Thermal Expansion Alloys

Control of thermal expansion mismatch is a critical goal of engineering design in a wide range of applications, particularly in cases where system components are small, are subject to large changes (gradients) in temperatures, or require extreme dimensional stability over a wide range of temperatures. Thermal expansion compensation often requires materials with either negative or (close to) zero thermal expansion (NTE or ZTE, respectively).

---

*Reprinted with permission from "Tailored thermal expansion alloys" by Monroe, J.A., Gehring, D., Karaman, I., Arroyave, R., Brown, D. W., Clausen, B., 2016. Acta Materialia 102, pp. 333-341, Copyright 2015 by Acta Materialia Inc. published by Elsevier Ltd. DOI: 10.1016/j.actamat.2015.09.012

The most widely known mechanisms that yield negative thermal expansion (NTE) include the magneto-volume effect, atomic radius contraction upon electronic transitions and flexible networks [1]. The magneto-volume effect, first discovered in 1897 [1], is found in FeNi-based Invar alloys that are widely used for thermal expansion compensation due to its high strength and ductility. Invar's low thermal expansion originates from instabilities between different magnetic configurations that at the same time result in significant magnetostriction effects [4, 30]. Recently, clear links have been made between the magneto-volume effect and the martensitic phase transformations exhibited by FeNi alloys [2, 30]. In these systems, only compositional changes that affect magnetic ordering and unit cell volume can tailor Invar's thermal expansion characteristics.

Another mechanism for NTE is encountered in $Sm_{2.75}C_{60}$, one of the materials with the largest known NTE. In this case, the observed NTE arises from atomic radius contraction due to valence electron exchange. Unfortunately, this effect only occurs below 32 K [31] and is therefore of limited technological value. Other material systems exhibit NTE through atomic rotations and transverse atomic vibrations in flexible networks that occupy different atomic configurations with increasing temperature. For example, the ZrW2O8 [32-34] and ReO3 families of ceramics show isotropic NTE via octahedral site rotations that cause uniform contraction in the cubic unit cell. Transverse atomic vibrations in non-cubic crystalline metal oxides (such as $Mg_2Al_4Si_5O_{18}$ cordierite [35, 36], $LiAlSiO_4$ beucriptite [35, 36], $NaZr_2P_3O_{12}$ [35, 36] and $PbTiO_3$ perovskite [36]) and carbon structures [37] (such as graphite, carbon fibers and nanotubes) result in NTE in certain material directions and positive thermal expansion (PTE) in others. Unfortunately, the application potential of NTE ceramics is limited due to their low fracture toughness [38], low thermal conductivity, and the need for chemical composition changes to tailor their coefficient of thermal expansion (CTE). While carbon reinforced composites are a more attractive alternative for tailored thermal expansion compensation, harnessing carbon's low CTE requires complex and expensive composite fabrication techniques.

In this work, a new method for easily tailoring the thermal expansion coefficient of alloys that exhibit martensitic transformation by harnessing their giant NTE and PTE associated with different crystallographic directions is presented. Interestingly, the NTE and PTE directions are not solely related to the martensite's crystal symmetry but can be predicted by comparing the high temperature austenite phase's lattice parameters with the low temperature martensite's lattice parameters. While the fundamental nature of this anisotropic thermal expansion is currently not understood, this simple correspondence successfully predicts the PTE and NTE directions of not only martensitic metals and alloys such as NiTiPd, TiNb, CoNiGa, NiTi [39], and a-Uranium [40], but also functional ceramics such as $PbTiO_3$ that undergo martensitic transformation. These different materials represent various crystallographic symmetries, composition, chemical ordering, and bonding types while sharing martensitic transformation and thermal expansion anisotropy. The ability to tailor an alloy's CTE using simple mechanical deformation promises exceptional control over thermal expansion compensation design in the automotive, aerospace, marine, electronic, power generation and transmission, and scientific instrumentation industries.

2.2 Experimental procedures and calculations used in this background work

We selected three different alloy systems exhibiting martensitic transformation in order to demonstrate the CTE anisotropy of martensitic alloys regardless of the crystal structure of martensite, or whether the alloy is ordered or not. In addition, we show that different, but simple thermo-mechanical processing methods can be used to tailor the CTE of these alloys between large positive and large negative values, by crystallographically texturing martensite through martensite reorientation/detwinning mechanisms. These alloy systems are $Ni_{19.5}Ti_{50.5}Pd_{30}$ in polycrystalline form, $Co_{49}Ni_{21}Ga_{30}$ as single crystals, and $Ti_{78}Nb_{22}$ in polycrystalline form. Figure 2.1 displays the comparison between the austenite (blue) and martensite (green) phases for these three alloys. The three alloys were selected as representative systems to illustrate the universal nature of the CTE anisotropy and tailorable CTE in martensitic materials. Using Figure 2.1, the lattice parameter correspondence between austenite and martensite will be shown to correlate with the observed thermal expansion anisotropy below.

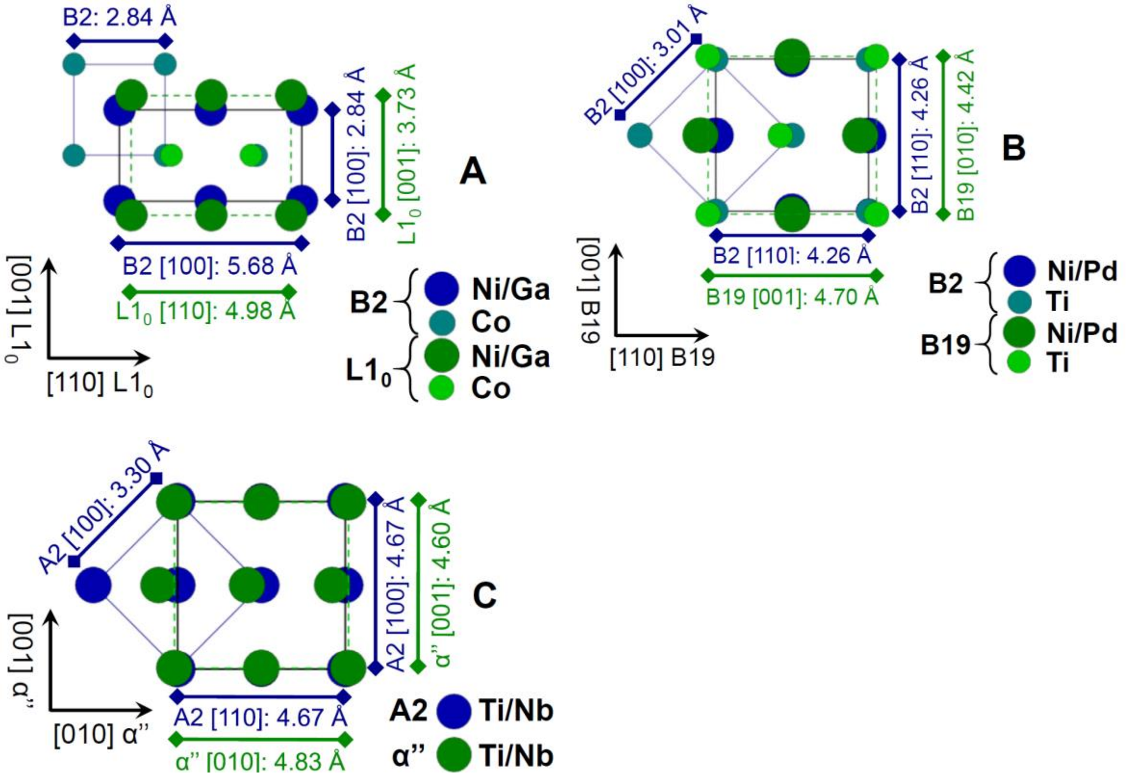

Figure 2.1 Crystallographic relationships between phases. Cubic austenite (ordered B2 CoNiGa (A) and NiTiPd (B) and disordered A2 TiNb (C)), and martensite (ordered tetragonal L10 CoNiGa (A), ordered orthorhombic B19 NiTiPd (B), and disordered orthorhombic α'' TiNb (C)) of the materials studied in the present work

$Co_{49}Ni_{21}Ga_{30}$ single crystal samples were grown in a He environment using the Bridgman technique. 4 x 4 x 8 mm samples were wire electro-discharge machined (EDM) from the larger single crystals and etched to remove the EDM recast layer. The samples were then homogenized at 1473 K for 4 h, followed by water quenching (WQ) under ultra-high purity (UHP) argon in quartz ampules. These samples were mostly used for neutron diffraction experiments in order to demonstrate the CTE anisotropy in an example tetragonal (L_{10}) martensite system. For the NiTiPd alloy, the ingots with the composition of $Ni_{19.5}Ti_{50.5}Pd_{30}$ were vacuum induction melted in a graphite crucible and cast into a water-cooled copper mold. The ingots were homogenized and encased in a steel can prior to 900 °C extrusion with a 7 to 1 reduction in area. Dog-bone tension samples were then wire EDMed from the extruded rods for tensile processing. Elemental Ti and Nb were arc melted under argon gas to obtain samples with the composition of $Ti_{78}Nb_{22}$. The ingot was then sealed in a quartz tube under UHP argon and heat treated at 1273 K for 24 h. 0.5 mm thick $Ni_{19.5}Ti_{50.5}Pd_{30}$ and $Ti_{78}Nb_{22}$ samples were wire EDM cut and polished to a mirror finish prior to the diffraction experiments.

Lattice parameters for $Ni_{19.5}Ti_{50.5}Pd_{30}$ and $Ti_{78}Nb_{22}$ were determined at discrete temperatures using X-ray diffraction (XRD), while $Co_{49}Ni_{21}Ga_{30}$ was characterized using neutron diffraction. During the diffraction experiments, all samples were first cooled to the lowest diffraction temperature and heated to each subsequent measurement temperature. XRD was conducted using Cu K-a radiation on a Bruker AXS X-Ray Diffractometer with a hot stage fitted with a platinum heating strip. Temperature was controlled and measured using a thermocouple fixed to the sample's surface. The lattice parameters were determined using TOPAZ software by fitting a pseudo-Voigt function to individual XRD peaks and using Bragg's law to calculate the atomic plane spacing. Texture analysis was also performed on the 0%, 25% and 50% rolled $Ti_{78}Nb_{22}$ samples. A three-axis goniometer stage in the Bruker AXS Diffractometer was used to rotate the sample. Inverse pole figures were created from the texture data using MTEX data analysis code.

Neutron diffraction was conducted using the Spectrometer for Materials Research at Temperature and Stress (SMARTS) instrument [41] and the High Intensity

Powder Diffractometer (HIPD) at the Lujan Neutron Scattering Center at the Los Alamos Neutron Science Center (LANSCE). The Lujan Center is a pulsed spallation source of a “white” neutron beam. SMARTs and HIPD operate on a 10 °C water moderator providing useful neutrons in the range of 0.5e4 Å. Sample cooling on SMARTS was achieved under vacuum using a helium closed-cycle refrigerator (CCR) capable of reaching temperatures down to 50 K. Sample cooling on HIPD was achieved down to 4 K using a similar CCR with He exchange gas. Time of flight (TOF) data was collected on stationary detector banks comprised of 3He fill aluminum tubes. Lattice spacing was determined by single peak fits of the TOF data using the rawplot subroutine of the General Structure Analysis System (GSAS) software developed at Los Alamos [42]. The materials d-spacing at various temperatures was used to calculate the thermal lattice strain along specific crystal orientations and determine the thermal expansion anisotropy.

For thermal expansion tensor calculations, the Lagrangian or engineering thermal expansion (a) along any unit vector (n_i) in a solid is given by $\alpha \equiv \frac{1}{l_0}\frac{\delta l}{\delta T} = \frac{\delta \varepsilon}{\delta T} = \alpha_{ij} n_i n_j$ where l_o is the original material length along n_i, l is the temperature dependent material length along n_i, ε is the thermally induced lattice strain along n_i, and a_{ij} is the thermal expansion tensor. a_{ij} is anisotropic in crystalline structures with their respective forms given by Ref. [43]. By setting n_i parallel to the plane normals and l equal to the planar spacing, the temperature dependent lattice spacing can be used to calculate a along different crystallographic directions. The best way to determine lattice spacing is through X-ray or neutron diffraction experiments where each diffraction peak represents the distance between crystallographic planes. While the minimum number of diffraction peaks required to determine the complete thermal expansion tensor is equal to the number of independent thermal expansion components of a, a least squares refinement of several peaks is preferred [39] to increase accuracy. The corresponding thermal expansion tensor components for each material studied in this work are presented in the next section.

Processing to achieve tailored thermal expansion was conducted on $Ni_{19.5}Ti_{50.5}Pd_{30}$ by pulling in tension and $Ti_{78}Nb_{22}$ by room temperature rolling. Tensile processing was achieved by incremental strain tests on a servo-hydraulic MTS test frame and the thermal expansion response was measured at each deformation increment. Displacement was measured using an MTS high temperature extensometer fitted with ceramic extension rods in direct contact with the sample. Heating and cooling were achieved by conduction through the grips. Copper coils were wrapped around the grips to flow liquid nitrogen for cooling and band heaters around the coils for heating. The homogenized $Ti_{78}Nb_{22}$ ingot was wire EDM cut into 4mm thick coins and subsequently rolled to 20%, 50% and 80% thickness reduction at room temperature. 5 mm long compression samples were wire EDM cut along the rolling and transverse sample directions for thermal expansion measurement on a TA Instruments Thermo-Mechanical Analyzer (TMA).

2.3 Discussion of study results

The thermal expansion of the respective martensitic crystal structures of the $Ni_{19.5}Ti_{50.5}Pd_{30}$, $Ti_{78}Nb_{22}$ and $Co_{49}Ni_{21}Ga_{30}$ alloys was determined by measuring the lattice spacing at various temperatures using X-ray and neutron diffraction measurements. Figure 2.2 displays the diffraction patterns of $Ni_{19.5}Ti_{50.5}Pd_{30}$ at 300 K, $Ti_{78}Nb_{22}$ at 300 K, and $Co_{49}Ni_{21}Ga_{30}$ at 4 K highlighting reflections for the orthorhombic B19, orthorhombic disordered and tetragonal $L1_0$ martensites, respectively. The strains $\varepsilon(T) = (l(T) - l_0)/l_0$ between different lattice planes for $Co_{49}Ni_{21}Ga_{30}$, $Ti_{78}Nb_{22}$ and $Ni_{19.5}Ti_{50.5}Pd_{30}$ are displayed in Figure 2.3 with lo taken from the diffraction patterns in Figure 2.2

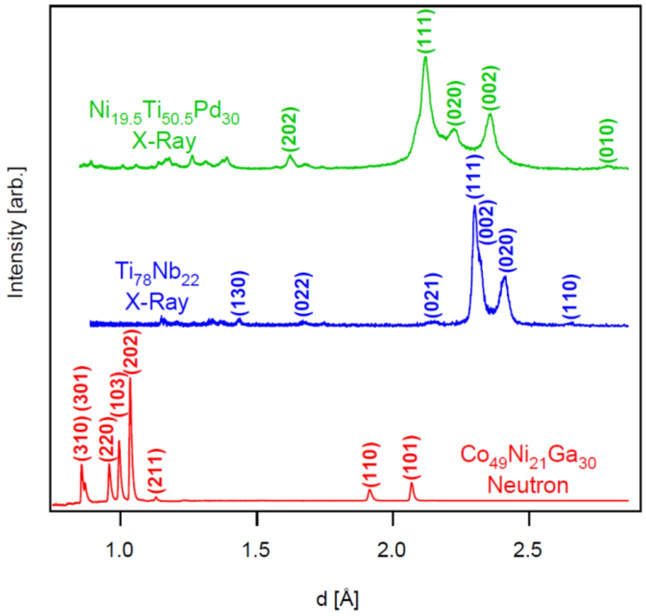

Figure 2.2: Indexed diffraction patterns for martensite phases. $Ni_{19.5}Ti_{50.5}Pd_{30}$ and $Ti_{78}Nb_{22}$ at 300 K from the XRD experiments and $Co_{49}Ni_{21}Ga_{30}$ martensite at 4 K. The martensite phase structures are ordered B19 orthorhombic for NiTiPd, disordered orthorhombic for TiNb, and $L1_0$ for CoNiGa.

The markers correspond to the data points taken from several planar spacing reflections. All the experimental temperatures are below the martensitic transformation finish temperature for each material, i.e. 316 K for $Co_{49}Ni_{21}Ga_{30}$ [44], 500 K for $Ti_{78}Nb_{22}$ [45] and 500 K for $Ni_{19.5}Ti_{50.5}Pd_{30}$ [46].

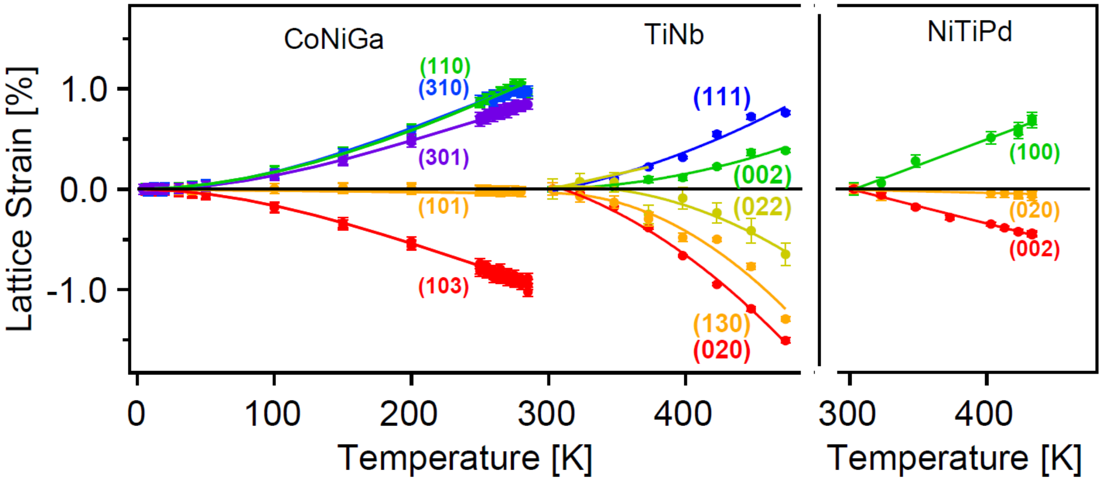

Figure 2.3 Thermal expansion along different crystallographic planes in the three different alloys in the present study. Lattice strains between different crystallographic planes are shown for martensitic $Co_{49}Ni_{21}Ga_{30}$ between 4 K - 285 K, $Ti_{78}Nb_{22}$ between 303 K-473 K, and $Ni_{19.5}Ti_{50.5}Pd_{30}$ between 303 K - 433 K, based on their transformation temperatures from martensite to austenite, which dictate the highest temperature the martensite lattice strains can be determined.

The $Ni_{19.5}Ti_{50.5}Pd_{30}$ response is linear within the measurement uncertainty in the studied temperature range with expansion between the (100) planes and contraction between the (020) and (002) planes. The distances between the (110), (310) and (301) $Co_{49}Ni_{21}Ga_{30}$ planes increase while those between the (103) planes decreases and the distance between the (101) planes does not change. The $Ti_{78}Nb_{22}$‘s (020), (130), (021) and (022) planes contract while the (002) and (111) planes expand with increasing temperature. Second order polynomial fits of the $Co_{49}Ni_{21}Ga_{30}$ and $Ti_{78}Nb_{22}$ strain data and linear fits of the $Ni_{19.5}Ti_{50.5}Pd_{30}$ strain data, solid lines in Figure 2.3, were used to determine the components of the thermal expansion tensors.

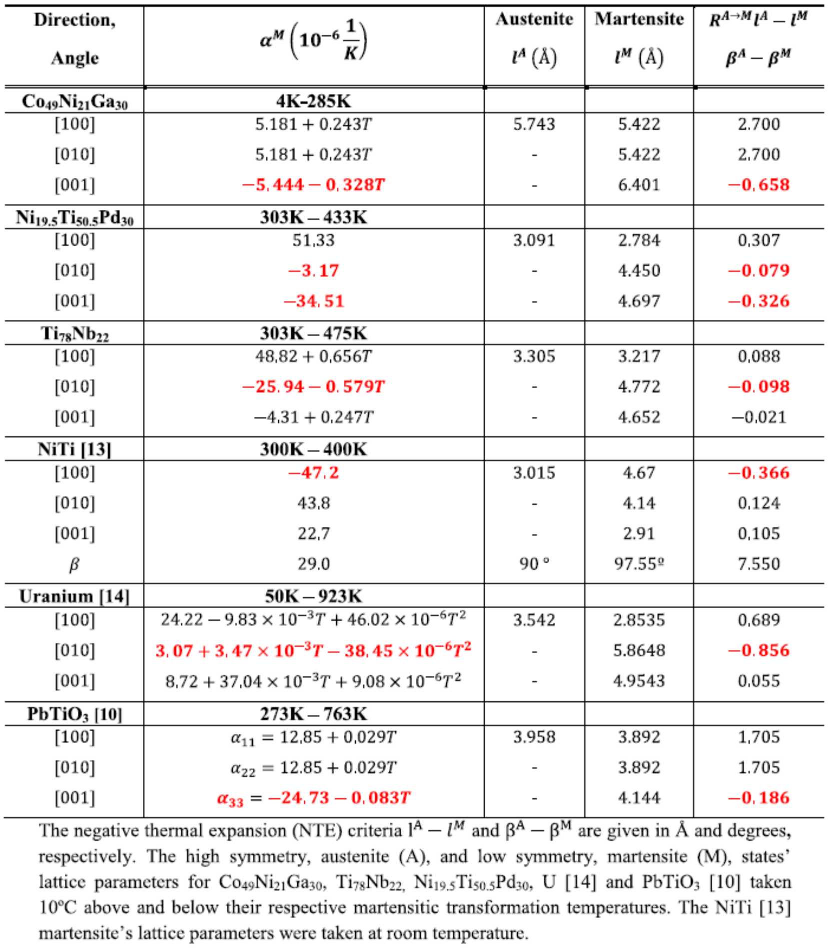

Direction, Angle	$\alpha^M \left(10^{-6}\frac{1}{K}\right)$	**Austenite** l^A (Å)	**Martensite** l^M (Å)	$R^{A\to M}l^A - l^M$ $\beta^A - \beta^M$
$Co_{49}Ni_{21}Ga_{30}$	**4K-285K**			
[100]	$5.181 + 0.243T$	5.743	5.422	2.700
[010]	$5.181 + 0.243T$	-	5.422	2.700
[001]	$\mathbf{-5,444 - 0,328}\boldsymbol{T}$	-	6.401	$\mathbf{-0,658}$
$Ni_{19.5}Ti_{50.5}Pd_{30}$	**303K – 433K**			
[100]	$51{,}33$	3.091	2.784	0,307
[010]	$\mathbf{-3,17}$	-	4.450	$\mathbf{-0.079}$
[001]	$\mathbf{-34,51}$	-	4.697	$\mathbf{-0,326}$
$Ti_{78}Nb_{22}$	**303K – 475K**			
[100]	$48{,}82 + 0{,}656T$	3.305	3.217	0,088
[010]	$\mathbf{-25,94 - 0,579}\boldsymbol{T}$	-	4.772	$\mathbf{-0,098}$
[001]	$-4{,}31 + 0{,}247T$	-	4.652	−0,021
NiTi [13]	**300K – 400K**			
[100]	$\mathbf{-47,2}$	3.015	4.67	$\mathbf{-0,366}$
[010]	$43{,}8$	-	4.14	0,124
[001]	$22{,}7$	-	2.91	0,105
β	29.0	90 °	97.55º	7.550
Uranium [14]	**50K – 923K**			
[100]	$24.22 - 9.83 \times 10^{-3}T + 46.02 \times 10^{-6}T^2$	3.542	2.8535	0,689
[010]	$\mathbf{3,07 + 3,47 \times 10^{-3}}\boldsymbol{T}\mathbf{ - 38,45 \times 10^{-6}}\boldsymbol{T^2}$	-	5.8648	$\mathbf{-0,856}$
[001]	$8{,}72 + 37{,}04 \times 10^{-3}T + 9{,}08 \times 10^{-6}T^2$	-	4.9543	0,055
$PbTiO_3$ [10]	**273K – 763K**			
[100]	$\alpha_{11} = 12{,}85 + 0{,}029T$	3.958	3.892	1,705
[010]	$\alpha_{22} = 12.85 + 0.029T$	-	3.892	1.705
[001]	$\boldsymbol{\alpha_{33}} = \mathbf{-24,73 - 0,083}\boldsymbol{T}$	-	4.144	$\mathbf{-0,186}$

The negative thermal expansion (NTE) criteria $l^A - l^M$ and $\beta^A - \beta^M$ are given in Å and degrees, respectively. The high symmetry, austenite (A), and low symmetry, martensite (M), states' lattice parameters for $Co_{49}Ni_{21}Ga_{30}$, $Ti_{78}Nb_{22}$, $Ni_{19.5}Ti_{50.5}Pd_{30}$, U [14] and $PbTiO_3$ [10] taken 10°C above and below their respective martensitic transformation temperatures. The NiTi [13] martensite's lattice parameters were taken at room temperature.

Table 2.1 Thermal expansion, austenite and martensite lattice parameters, and lattice parameter comparison for three alloys studied in the present work and three additional materials from literature.

Table 2.1 displays the experimentally measured thermal expansion coefficients along martensite's principal crystallographic directions of [100], [010] and [001], corresponding to martensite's a_{11}, a_{22}, and a_{33}, respectively.

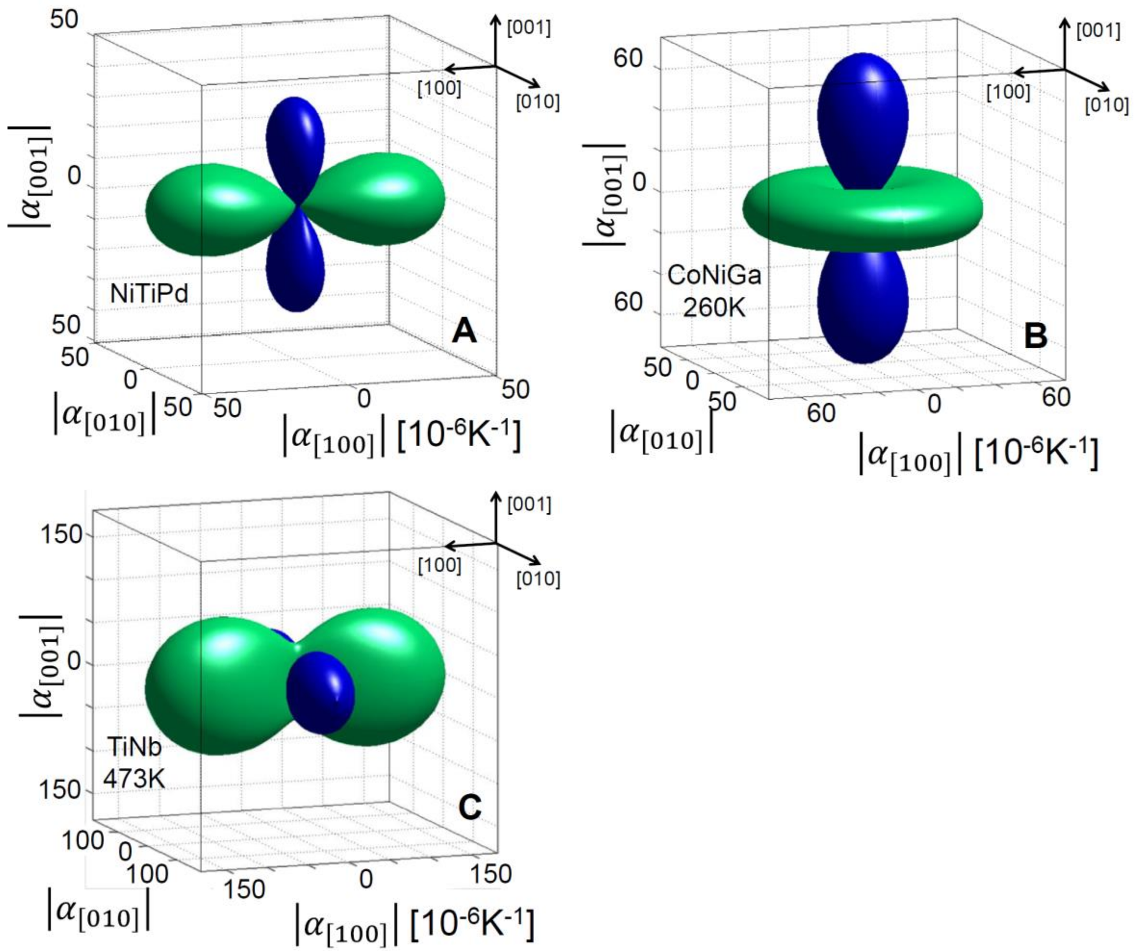

Figure 2.4 Graphical representation of the thermal expansion magnitudes for $Ni_{19.5}Ti_{50.5}Pd_{30}$ (A), $Co_{49}Ni_{21}Ga_{30}$ (B), and $Ti_{78}Nb_{22}$ (C). Three dimensional ellipsoids showing the positive (green) and negative (blue) thermal expansion magnitudes along different crystallographic directions for orthorhombic $Ni_{19.5}Ti_{50.5}Pd_{30}$ across all experimental temperatures shown in Fig. 3, tetragonal $Co_{49}Ni_{21}Ga_{30}$ at 260 K and orthorhombic $Ti_{78}Nb_{22}$ at 473 K. These figures were created using Coefficient of Thermal Expansion Analysis Suite (CTEAS) software.

Figure 2.4(a-c) displays the CTE magnitudes for (A) $Ni_{19.5}Ti_{50.5}Pd_{30}$, (B) $Co_{49}Ni_{21}Ga_{30}$ at 260 K, and (C) $Ti_{78}Nb_{22}$ at 473 K, determined from the thermal expansion measurements displayed in Fig. 3. The green and blue ellipsoids correspond to positive and negative thermal expansion values, respectively. The orthorhombic $Ni_{19.5}Ti_{50.5}Pd_{30}$ alloy exhibits positive thermal expansion along the [100] direction and negative thermal expansion along the [001] direction. $Ni_{19.5}Ti_{50.5}Pd_{30}$'s [010] direction has a very small negative thermal expansion. The tetragonal $Co_{49}Ni_{21}Ga_{30}$ alloy exhibits uniform positive thermal expansion along the [100] and [010] directions and negative thermal expansion along the [001] direction. While $Ti_{78}Nb_{22}$ shares its orthorhombic crystal symmetry with $Ni_{19.5}Ti_{50.5}Pd_{30}$, it only shows contraction along the [010] axis and expansion along the [100] and [001] axes. This indicates that the crystal symmetry is not the only factor that influences the thermal expansion anisotropy in these martensitic alloys. While they may have different values, the thermal expansion values inherit the symmetry of the crystal phase with the orthorhombic $Ti_{78}Nb_{22}$ and $Ni_{19.5}Ti_{50.5}Pd_{30}$ having different values in each crystallographic direction and the tetragonal $Co_{49}Ni_{21}Ga_{30}$ being isotropic in the [100]-[010] plane. The largest magnitudes of positive and negative thermal expansion are $Ti_{78}Nb_{22}$'s giant +181 x 10^{-6} K^{-1} and -142 x 10^{-6} K^{-1} at 473 K.

2.4 Description of tailored thermal expansion

The giant thermal expansion anisotropy observed at the atomic level can be leveraged to tune the alloys' macroscopic thermal expansion through control of the crystallographic texture via thermo-mechanical deformation.

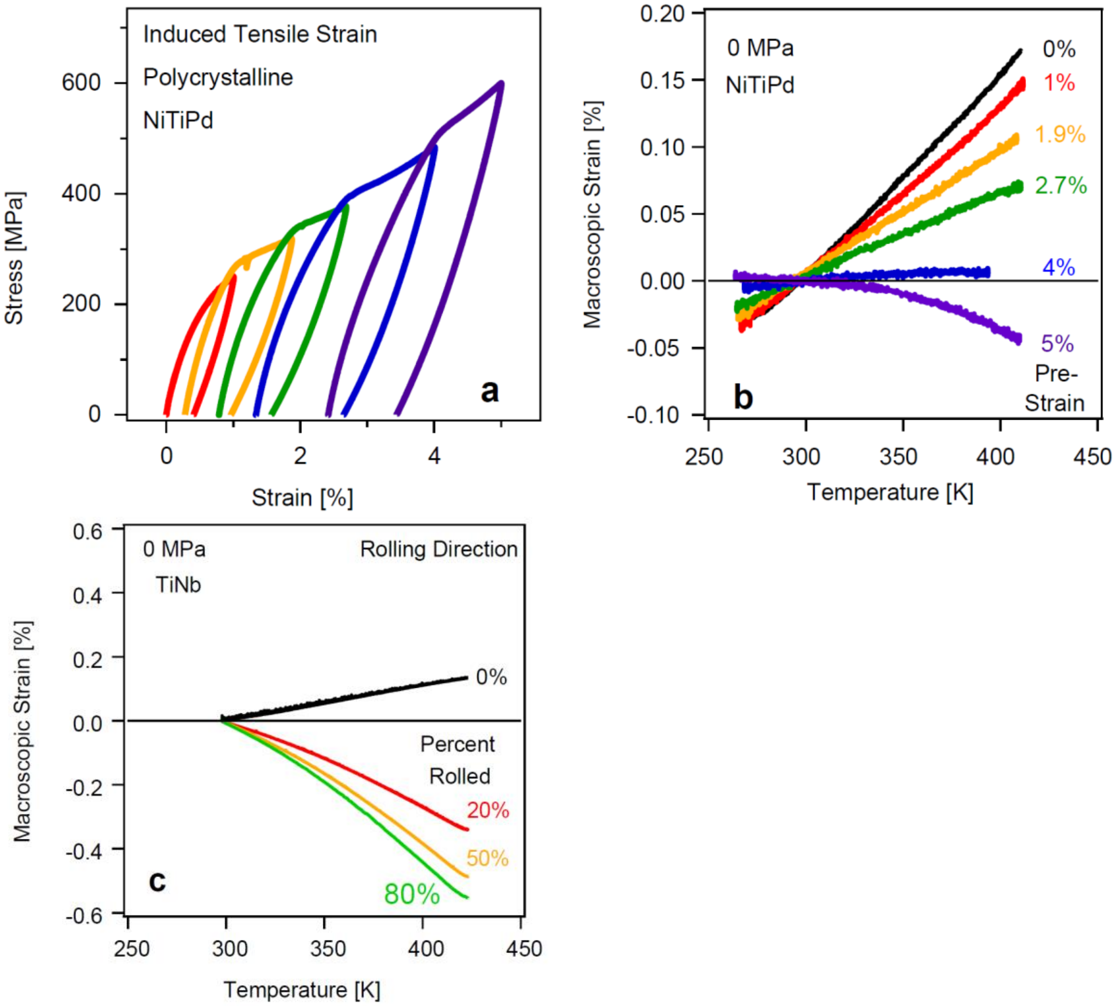

Figure 2.5 The incremental stress-strain response, (a), of a $Ni_{19.5}Ti_{50.5}Pd_{30}$ polycrystal. Macroscopic strain vs temperature response of (b) tensile pre-strained $Ni_{19.5}Ti_{50.5}Pd_{30}$ shown in (a), and (c) cold rolled $Ti_{78}Nb_{22}$ before and after deformation.

Figure 2.5(a) shows the stress-strain response of $Ni_{19.5}Ti_{50.5}Pd_{30}$ as the sample is loaded, unloaded, and loaded again, under tension, at room temperature. In between each incremental loading-unloading cycle, the sample was thermally cycled within the martensitic phase under zero stress to obtain the bulk samples' macroscopic thermal expansion characteristics. Figure 2.5(b) displays the macroscopic strain vs. temperature response for the polycrystalline $Ni_{19.5}Ti_{50.5}Pd_{30}$ strained incrementally between 0% and 5% tensile strain in Figure 2.5(a). The 0% strained condition expands with increasing temperature as expected from traditional alloys. Increasing the pre-strain from 1% to 4% strain decreases the material's dependence on temperature as the CTE approaches zero. At 5% strain, the response crosses from positive thermal expansion to negative thermal expansion at the macroscopic scale. A similar decrease in CTE is observed for cold rolled $Ti_{78}Nb_{22}$ along the rolling direction as displayed in Figure 2.5(c). The 0% rolled sample has a normal positive thermal expansion response while increasing deformation percent from 20% to 80% decreases the thermal expansion values to large negative magnitudes.

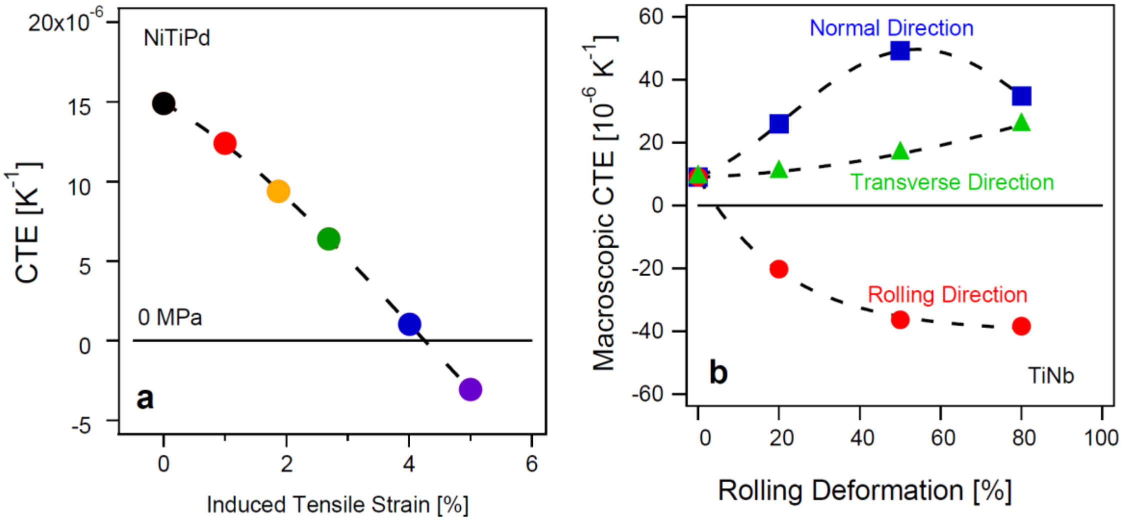

Figure 2.6 Macroscopic coefficients of thermal expansion vs. deformation percent for bulk $Ni_{19.5}Ti_{50.5}Pd_{30}$ (a) and $Ti_{78}Nb_{22}$ alloys (b).

The resulting thermal expansion coefficients vs. induced deformation percent are shown in Figure 2.6(a) for $Ni_{19.5}Ti_{50.5}Pd_{30}$ and Figure 2.6(b) for $Ti_{78}Nb_{22}$. The $Ni_{19.5}Ti_{50.5}Pd_{30}$ linear CTE decreases with increasing imposed strain and ultimately exhibits negative thermal expansion at the macroscopic scale. The thermal expansion along the rolling, transverse and normal sample directions are displayed for $Ti_{78}Nb_{22}$. The rolling direction's CTE decreases asymptotically from 9 x 10^{-6} K^{-1} to -40 x 10^{-6} K^{-1}. The transverse and normal directions both increase with increasing deformation with the normal direction changing the most from 9 x 10^{-6} K^{-1} to 50 x 10^{-6} K^{-1}. It should be noted that the reason for the apparent decrease in CTE with the 80% rolled sample measurement along the normal direction is not currently known, further diffraction studies on the samples rolled to different thickness reductions are underway to reveal the potential reasons.

2.5 Further discussion of study results

In addition to $Ni_{19.5}Ti_{50.5}Pd_{30}$, $Ti_{78}Nb_{22}$ and $Co_{49}Ni_{21}Ga_{30}$ material systems presented above, some other material systems known to exhibit NTE and PTE anisotropic thermal expansion below their martensitic transformation temperatures are thermoelastic alloys and ceramics, such as NiTi [39] and $PbTiO_3$ [36], and non-thermo-elastic a-Uranium [40]. These and the materials studied in this work represent pure metals (U), disordered alloys (TiNb), B2 ordered alloys (NiTi and NiTiPd), Heusler alloys (CoNiGa), and ceramics ($PbTiO_3$). Table 1 lists the experimentally determined thermal expansion along martensite's crystallographic directions from diffraction experiments with NTE values highlighted in red. The two tetragonal crystal structures, $Co_{49}Ni_{21}Ga_{30}$ and $PbTiO_3$, exhibit contraction along the [001] direction and expansion along the [100] and [010] directions while the monoclinic material, NiTi, exhibits NTE only along the [100] direction. The three orthorhombic materials show different behavior from each other with $Ni_{19.5}Ti_{50.5}Pd_{30}$ contracting along the [100] and [010] directions while U and $Ti_{78}Nb_{22}$ contract only along [010].

Aside from PTE and NTE anisotropy, a common thread between these various materials is the martensitic transformation. A martensitic transformation is a diffusionless solid-solid phase transformation between a high temperature austenite phase and a low temperature martensite phase. The austenite phase in all these materials has cubic symmetry that exhibits isotropic PTE while the martensite phase has lower symmetry, such as tetragonal; orthorhombic; or monoclinic, and exhibits PTE and NTE anisotropy along different crystallographic directions. The correspondence between these two crystal phases (i.e. austenite and martensite) can be determined using a simple rotation matrix, $R^{A \rightarrow M}$ presented in Table 2, that maps distances from austenite's to martensite's principal coordinate system. These rotation matrices will be used to compare austenite and martensite lattice parameters below.

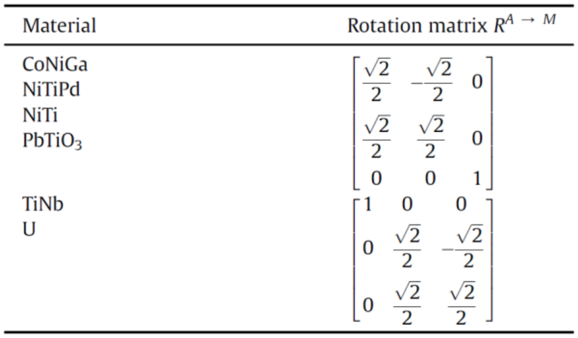

Material	Rotation matrix $R^{A \rightarrow M}$
CoNiGa NiTiPd NiTi $PbTiO_3$	$\begin{bmatrix} \frac{\sqrt{2}}{2} & -\frac{\sqrt{2}}{2} & 0 \\ \frac{\sqrt{2}}{2} & \frac{\sqrt{2}}{2} & 0 \\ 0 & 0 & 1 \end{bmatrix}$
TiNb U	$\begin{bmatrix} 1 & 0 & 0 \\ 0 & \frac{\sqrt{2}}{2} & -\frac{\sqrt{2}}{2} \\ 0 & \frac{\sqrt{2}}{2} & \frac{\sqrt{2}}{2} \end{bmatrix}$

Table 2.2 Rotation matrices that map the austenite to the martensite basis in martensitically transforming materials.

The lattice parameters for the high temperature austenite, l^A, and low temperature martensite, l^M, phases of these five different materials are presented in Table 1 along with a lattice parameter comparison $R^{A \rightarrow M} l^A - l^M$ along the given crystallographic directions. For all materials presented, the martensite's crystallographic NTE directions correspond to the crystallographic directions that are smaller in austenite than martensite, i.e. where $R^{A \rightarrow M} l^A < l^M$, and PTE directions correspond to directions that are larger in austenite than martensite, i.e. where $R^{A \rightarrow M} l^A > l^M$. This criterion can be observed graphically by comparing the austenite-martensite lattice schematics for CoNiGa, NiTiPd and TiNb displayed in Figure 2.1 The difference in angle, $\beta^A - \beta^M$, was also determined for monoclinic NiTi. The directions with negative values of $R^{A \rightarrow M} l^A <$

l^M (shown in red) are those that experimentally exhibit NTE and vice versa. The existence of positive and negative thermal expansion anisotropy in this wide variety of material systems and its connection to the austenite-martensite lattice parameter correspondence points to a mechanism potentially linked to the martensitic transformation. This observation also suggests that the Invar effect recently discovered in cold rolled $Ti_{23}Nb_{0.7}Ta_2Zr_{1.2}O$ alloys may be a result of stress induced martensite in addition to the strain glass transition as described in Ref. [27].

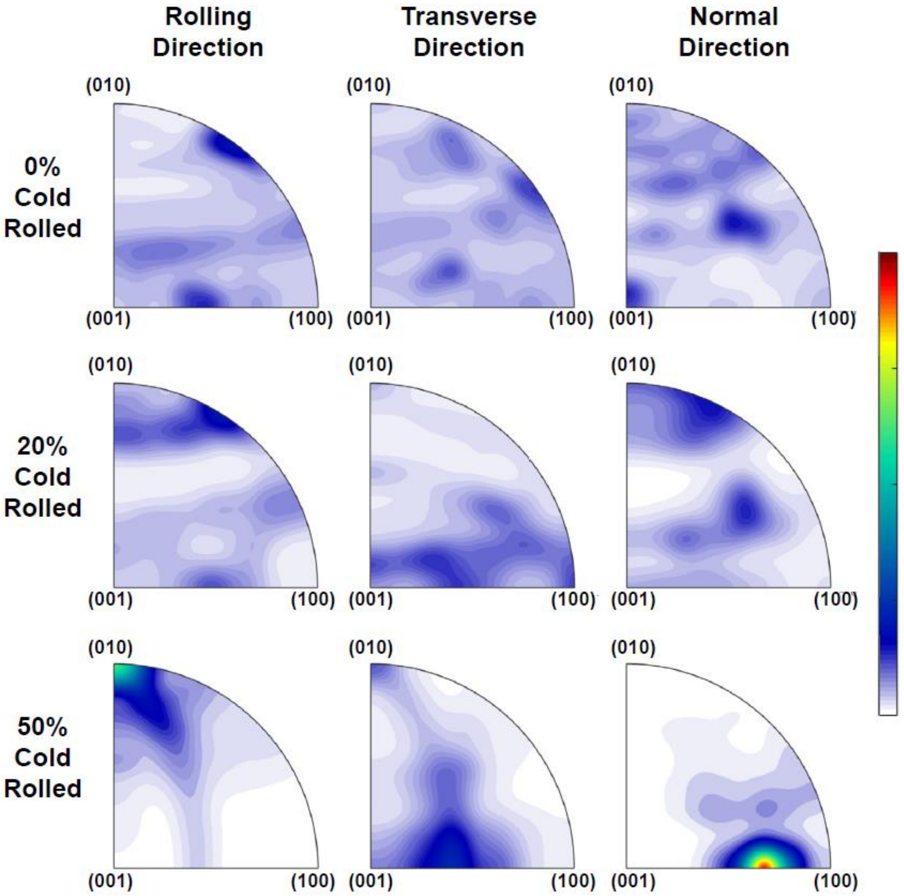

Figure 2.7 Inverse pole figures of as-received and rolled $Ti_{78}Nb_{22}$ showing the texture evolution from 0%, 20% and 50% cold rolling.

The tailored directional macroscopic CTE responses are achieved here by orienting the martensite variants along the sample directions via thermo-mechanical deformation. Figure 2.7 displays inverse pole figures along the rolling, transverse, and normal directions of $Ti_{78}Nb_{22}$ at 0%, 20% and 50% rolling deformation. The 0% rolled material shows nearly random weak texture with martensite variants mostly randomly oriented within the sample. This is corroborated by the isotropic macroscopic CTE exhibited by the 0% rolled condition in Figure 2.6. The 50% rolled condition on the other hand exhibits strong (010) texture along the rolling direction, (307) texture in the transverse direction and (101) texture along the normal direction. The $Ti_{78}Nb_{22}$ crystal's largest negative thermal expansion direction is [010], as shown in Figure 2.4(c). The intensity of (010) poles along the sample's rolling direction increases with higher rolling reduction. Therefore, the lattice level negative thermal expansion in Table 1 and Figure 2.3, creates the negative thermal expansion observed at the macroscopic scale, Fig. 5C. The [307] and [101] directions exhibit positive thermal expansion with the [101] direction having a larger CTE magnitude than [307], as shown in Figure 2.4(c). This correlates strongly with the textures observed in the transverse and normal sample directions, respectively. The transverse and normal directions exhibit positive thermal expansion at all rolling deformation levels. The transverse direction's CTE increases with increasing deformation but remains smaller in magnitude than the normal direction's CTE. As a result of the texturing process, the macroscopic thermal expansion of this material is “programmed” or tuned by the rolling deformation.

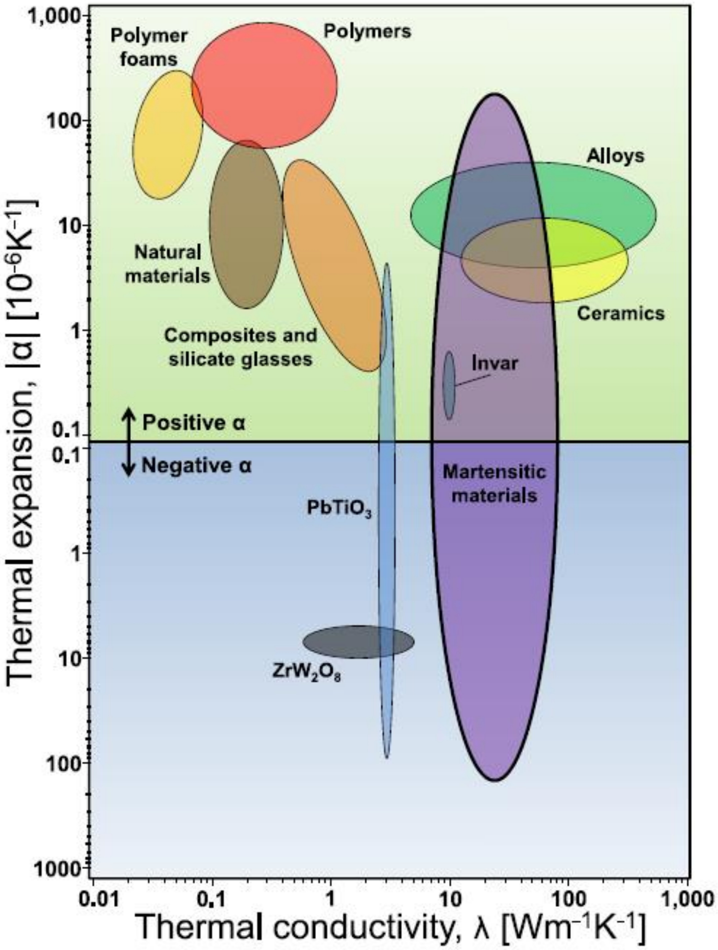

Figure 2.8 Thermal expansion vs. thermal conductivity for various materials. This chart compares the thermal expansion and conductivity of negative thermal expansion $PbTiO_3$, ZrW_2O_8 and martensitic materials to traditional positive thermal expansion materials in the Granta Design CES materials database.

Figure 2.8 displays the linear thermal expansion coefficient vs. thermal conductivity for various material types. Highlighted in purple is the current thermal expansion region that a single crystal martensitic material could potentially exhibit. The thermal expansion characteristics for this new class of tailored thermal expansion alloys can match those of polymers, ceramics, and other metals over a much wider range than composite materials. The thermal expansion anisotropy is key to obtaining a tailored thermal expansion coefficient in a single material without changing the chemical composition. This is a response that materials exhibiting isotropic thermal expansion characteristics, such as Invar and ZrW_2O_8, cannot achieve. This new approach for tailoring CTEs in bulk materials can provide the means to tightly control a metal's thermal expansion response beyond any currently known material, without the tradeoffs associated with changing material composition or complex composite fabrication. More importantly, the decoupling between composition and macroscopic CTE dramatically increases the materials design space as composition could potentially be adjusted to meet specific functional requirements not necessarily related to the need to compensate thermal expansion.

2.6 Conclusions on tailorable thermal expansion based on background results

In conclusion, the controlled crystallographic texturing of martensite variants can be used to tailor the thermal expansion response of martensitic materials through simple thermomechanical processing. In principle, any texturing method could be used to tune the macroscopic thermal expansion coefficient of these materials. This ability to control the CTE of these materials through texture is associated with the highly anisotropic nature of the thermal expansion tensor in the martensite phase. It was also shown that NTE or PTE crystallographic directions were connected to the crystallographic relationship between the austenite and martensite lattices, pointing to a possible mechanism linked to the martensitic transformation shared by these materials. It is believed that these criteria can be applied to a much wider range of materials that undergo martensitic transformation, although there is still much to be understood about the fundamental physical basis for the observed phenomenon. The degree of control over the macroscopic thermal expansion response of the materials presented in this work suggests a revolutionary and inexpensive approach to tune the CTE of materials for use in applications that are sensitive to temperature changes or gradients.

CHAPTER III

EXPERIMENTAL MATERIALS AND METHODS

The aim of this chapter is to present details on the fabrication and processing of the materials used in this study, as well as the thermomechanical testing methods, characterization, and examination tools and methods utilized.

3.1 Materials Selection and Preparation

The materials which have been used for this characterization to this point have been members of the following alloy systems: TiNb binary, NiTi intermetallic, and NiTiPd intermetallic. Each holds specific and distinct differences in martensite layout and overall properties which through comparing and contrasting the three respective systems should provide a broad overview of the expected behavior from martensitic anisotropy.

TiNb was selected as a candidate alloy because of its nature as a beta-titanium shape memory alloy. Addition of several different elements such as Sn, Nb, Ta, and others will stabilize the BCC β-phase at increasingly lower temperatures as more stabilizer is introduced; below the beta-phase formation temperature the atomic radius mismatch distorts the hexagonal close-packed structure of α-phase Ti into the martensites used for SMA behavior [28, 29]. The β-Ti family of alloys show characteristic SMA behaviors, but are not intermetallic as in NiTi, allowing for the exploration of a wider composition range (in TiNb, the orthorhombic α" phase is present from approximately 12 to 26 atomic percent Nb content) with accompanying large changes in behavior. Of greatest interest is the change in the A_s temperature in the system illustrated in Figure K-1 below. A_s can be observed reducing the Nb content below 22 at% allows for effective pre-transformation working temperatures in excess of 200 °C, which can be considered quite high for a normal SMA.

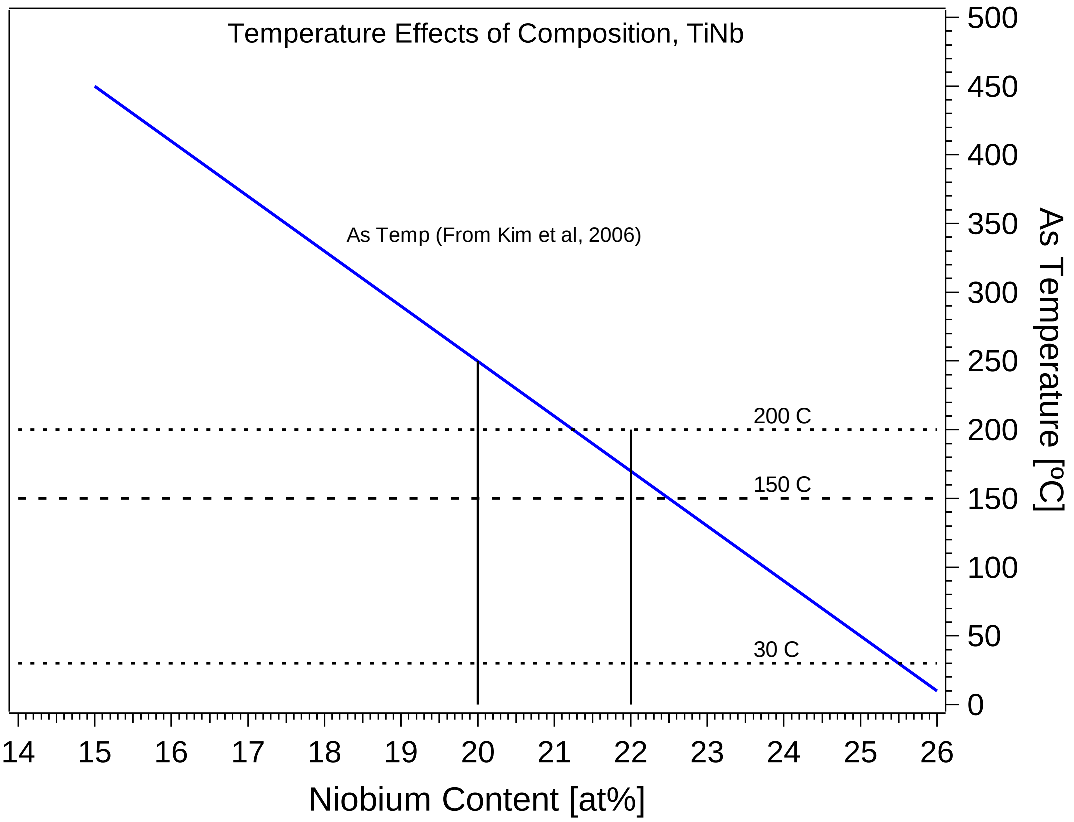

Figure 3.1 Change in the A_S temperature of TiNb as a function of Nb content [at%]. Data taken from reference [45].

To promote consistency and encourage maximum homogeneity of Nb distribution, the TiNb was heat treated using an identical pathway. Ingots (with varying shape) of Titanium Niobium binary alloy with nominal compositions of $Ti_{85}Nb_{15}$, $Ti_{80}Nb_{20}$,

$Ti_{79}Nb_{21}$, $Ti_{78}Nb_{22}$, and $Ti_{76}Nb_{24}$ (at%) were created by Sophisticated Alloys, Inc. via arc melting of elemental Ti and Nb with 99.99% purity in an argon atmosphere. The as-received material was sealed in quartz tubes while wrapped in tantalum foil under ultra-high purity (UHP) argon and homogenized by being heated to 1000 °C for a minimum of 24 hours before water quenching. After water quenching, the ingots would then be cut in various ways to accommodate the specific use requirements which will be discussed later.

In contrast to TiNb, both NiTi and NiTiPd have structures which are atomically ordered; that is to say atoms are not found at any position in the crystal, but rather at specific locations. For NiTi, the martensite phase is the B19' monoclinic geometry, while for NiTiPd it is instead an orthorhombic layout. NiTiPd, such as the $NiTiPd_{25}Ta_{0.5}$ used in this study, allows for a higher A_s than the binary NiTi material in addition to the distortions changing the phase structure geometry. NiTiPd is expected to offer an interesting bridge between NiTi and TiNb from an analysis perspective, being both ordered and orthorhombic when the others possess only one trait each.

The NiTi material used in this study was cut from the same master block with nominal composition of $Ni_{50}Ti_{50}$ at%. A separate block provided Ni-rich $Ni_{50.3}Ti$ (at%) alloy. These samples were cut into rectangular pieces from their source blocks via EDM before then being wrapped in molybdenum foil and sealed in quartz tubes under either high vacuum or UHP argon backfilling after pumping down to high vacuum. All of these samples were then homogenized at 800 °C for 1 hour before water quenching and sectioning into samples. NiTiPdTa was extruded, homogenized, and tensile samples had been cut prior to acquisition.

3.2 X-Ray Diffractography

The foundational information to evaluate any portion of the central hypothesis requires that the crystalline properties be examined; namely the crystalline thermal expansion anisotropy should be known for any sample group, and any texture which can be reasonably captured should be so done. To this end, two forms of X-ray diffractography were harnessed.

3.2.1 Copper k-α wavelength XRD

For TiNb, 1 mm thick samples were wire EDM cut from TiNb15, 20, and 22 ingots after quenching and polished to a mirror finish prior to the diffraction experiments. Lattice parameters were determined at discrete temperatures (in 15°C intervals) in martensite using X-ray diffraction (XRD) with Cu K-α radiation on a Bruker AXS X-Ray Diffractometer. Heating was achieved through Joule heating using a hot stage fitted with a platinum heating strip, with temperature control provided via a thermocouple in contact with said strip. During the diffraction experiments, all samples were first measured at the minimum diffraction temperature and heated to each subsequent measurement temperature afterwards. The lattice parameters were determined using TOPAZ software by fitting a pseudo-Voigt function to individual XRD peaks and using Bragg's law to calculate the atomic plane spacing. The thermal expansion of a given crystallographic direction was calculated from the d-spacing of the corresponding plane and normalized relative to the d-spacing value at 30°C.

The material in TiNb 15, 20, and 22 which had been rolled for initial characterization was examined for overall deformation texture by way of this same XRD machine. In this test a polished sample which had been cut from the rolled material would be mounted on a pedestal atop the center of the 3-axis mount inside the machine. A scan would be performed, and the 4 strongest peaks observed would be selected for texture measurement. In this measurement, the sample would be measured at each two-theta position specified at 5-degree intervals while being rotated 360 degrees in the first rotational axis. This rotation would be repeated at every 5 degrees from 0 to 85 degrees orientation in the second rotational axis. This information would then be compiled by the Bruker software and output. It would then been processed to remove defocusing effects and estimate edge properties via the PopLA DOS program, before outputting its estimated pole figures. These were then read and interpreted by the MTEX 4.5.2 program run via Matlab 2018a to generate orientation density functions and inverse pole figures.

Two problems were observed as a result of this work when characterizing TiNb via X-ray diffraction using Cu k-alpha (~25 keV) photons. The key problem with using this particular energy output is its micrometer-depth penetration. It was observed that only surface thermal expansion was being measured. This is problematic for two reasons: firstly, temperature control on the surface is difficult, and more chronically oxide layers would from rather rapidly during heating especially on polished samples. Scans gave few usable peaks as the large grain size (> 1mm) of TiNb alloy limits the grain density at the surface. This severely hampered maximum possible accuracy in texture, as both monoclinic and orthorhombic structures have more degrees of freedom. The peaks which could be observed only decreased in intensity further as temperature increased, becoming impossible to properly identify well below the expected A_s temperature. It was determined that a more accurate measurement of the thermal expansion was required.

3.2.2 Synchrotron XRD Diffraction

To measure the composition effect on crystalline thermal expansion anisotropy, therefore, unheated and unstressed tension doglegs of all compositions (in TiNb, NiTi, and NiTiPd) were measured at beamline 11 ID-C of the Advanced Photon Source synchrotron at Argonne National Lab. This was used as the 105 keV photons which offer up to 4mm penetration allow for examination through the entire depth of the samples provided. By using the synchrotron beamline, more grains could be passed through to increase the number of observable peaks and the influence of thermal fluctuation at the surface is replaced with the full bulk response. For temperature control the samples were installed into a Linkam 600 optical furnace with the beam set to pass through the gauge center of the dogleg. The furnace was provided argon for use as a purge gas and liquid nitrogen for cooling and heated the sample by Ohmic heating over a large area in contact with one face of the dogleg. The beam after interaction with the sample was counted by an area detector located approximately 1.8 m downrange from the furnace and was calibrated by use of a cerium oxide diffraction sample.

Doglegs of TiNb15, 20, 22, and 24 were cooled to -170 °C and then heated to their limit temperatures in the synchrotron. These limit temperatures were determined by prior testing via thermomechanical analysis to determine the onset of mechanical transformation, with an additional reduction of 15 °C to minimize the chances of transformation to the parent phase during heating. The limit temperature exceeded the mounting temperature for TiNb15 (300 °C), and was 225, 175, 140, and 90 °C respectively for TiNb20, 21, 22, and 24. When heating from -170 °C to the limit temperature, scans were taken at 40 °C intervals for TiNb15, and 20 °C intervals for TiNb20 and 24. In TiNb22, the intervals ranged from 40 °C between scans below 50 °C furnace temperature, to 5 °C intervals when less than 20 °C from the limit temperature. In all samples the material was cooled to -170 °C by intervals, heated to the limit temperature by intervals, then cooled back to -170 °C by the same intervals as in heating. For TiNb22 and 24 this was performed twice, while for TiNb15 and 20 this was only carried out once. Identical tests were performed with NiTi and NiTiPdTa samples using a 70 and 90 °C heating limit, respectively.

The effect of deformation on crystalline expansion anisotropy was examined by use of several prestrained samples of both TiNb(20, 22) and NiTi. The TiNb22 samples were subjected to a two-cycle heat-cool with 20 °C interval as described above, while the TiNb24 sample received only one heating/cooling cycle as it had been previously heated. Deformed NiTi was subjected to the same test as in the undeformed case. Before heating, each deformed sample was mounted on one end to a simple rotation stage absent any furnace, allowing for the beam to pass through the center of the sample while the sample could be rotated around its tension axis. For each, the beam was applied in discrete steps of five degrees in rotation over an entire 360-degree overall rotation, allowing for the capture of 72 distinct points of reference in each rotation.

For the synchrotron data collected, indexing and calculation of the crystalline anisotropy was done via the General Structure Analysis System II, Revision 3139 (GSAS-II) program. In using this area detector measurements were integrated through a circle bounded by a maximum and minimum of 2.0 and 6.0 two-theta effective angles to create an equivalent intensity vs two-theta representations of the sample measurements. Examination of each of these two-theta graphs allowed for indexing and determination of the two-theta value for each peak; this could then be converted to an equivalent d-spacing for each peak HKL via Bragg’s Law. Calculating these d-spacings and the change in magnitude for each temperature against a reference (minimum) temperature allowed for determination of the lattice strain in the crystalline directions indicated by each peak. This information could then be further used by the Coefficient of Thermal Expansion Analysis Suite 0.61 (CTEAS) software to generate thermal expansion fits across temperature ranges and determine the tensor of the thermal expansion for said temperature(s). In addition, texture from the rotational scans would be calculated from the raw synchrotron data via the Materials Analysis via Diffraction v2.76 (MAUD) program. From this analysis texture maps would be generated via MTEX 4.5.2 run inside Matlab 2018a.

3.3 Preparation of rolled samples, determination of transformation temperatures, and measurement of orthonormal CTE

3.3.1 Rolling of selected material

Samples not deformed via tension were instead prepared via rolling. This was selected as rolling provides consistent compressive stress applied simultaneously to both sides of a sample along a single line and can reach high deformation levels, allowing for examination of maximum response levels. Rolling was also of great interest during initial characterization as it can be easily scaled for industrial processing and use, meaning successful results by this method should be nearly-instantly usable in such a context.

For TiNb, the homogenized ingots were wire electro-discharge machining (EDM) cut into 4 mm thick square samples and subsequently rolled to 20%, 50% and 80% thickness reductions at room temperature. These three levels, in addition to undeformed material, were considered a good balance between materials use and enough tests to see a reasonable picture of the CTE evolution. Square samples with side lengths between 5 and 9 mm were wire EDM cut parallel to the rolling direction for thermal expansion measurements

In addition to TiNb, rolling was also conducted in NiTi using 1-inch squares of 4 mm initial thickness and reduction levels of 0, 5, 10, 15, 20, 25, and 30% rolling reduction. Each of these samples would similarly have TMA samples cut and measured with 7mm side lengths as well as 1.5 mm diameter disc samples for calorimetry.

3.3.2 Differential scanning calorimetry

Aforementioned discs of rolled NiTi as well as undeformed NiTi and NiTiPdTa samples were placed into aluminum pans and subjected to calorimetry measurements via a TA Instruments Q2000 differential scanning calorimeter (DSC) equipped with nitrogen purge gas and either a mechanical chiller or liquid nitrogen to provide cooling for the sample, depending on laboratory. Each sample was subjected to 3 cycles at 10 °C/min of heating and cooling between the designated maximum and minimum temperatures available to the respective machine. Low temperatures ranged from -100 to -50 °C, and high temperatures from 300 to 400 °C. Collected data was examined using Microsoft Excel.

3.3.3 Thermo-mechanical analysis

Thermomechanical analysis of rolled samples was performed on a TA Instruments Q400 Thermo-Mechanical Analyzer (TMA). Samples would be mounted upon a ceramic base, near to a thermocouple located within an electric furnace unit and contacted on top by a glass thermal expansion probe connected to an electronically measured balance. After closing the furnace unit, the atmosphere would be purged with use of nitrogen gas.

Due to the inconsistent heat flow which occurs in TiNb transformation, the austenite start temperatures (As) of the homogenized samples were primarily determined using thermomechanical analysis by running a sample to the maximum furnace temperature and examining when mechanical transformation was indicated by the large strain change which accompanied it in the measured sample dimensions. Using this method, transformation temperatures for TiNb alloys were determined as 155°C for $Ti_{78}Nb_{22}$, 225°C for $Ti_{80}Nb_{20}$, and >400°C (due to equipment limitation) for $TiNb_{15}$.

For characterization of thermal expansion each TMA sample was cooled to -25°C and then held isothermally for 2 minutes. The samples were then heated at 5°C/min to a reference temperature below their As for each alloy. These reference temperatures were 140°C for TiNb22, 210°C for TiNb20, and 350°C for TiNb15. The material was then held for 5 minutes at the maximum temperature before being cooled back to -25°C. The linear CTEs along three orthogonal directions were calculated as an average of the endpoint-to-endpoint linear slope of three subsequent heating and cooling steps from 25°C to 100°C in each direction.

For NiTi testing the furnace was cooled to -40°C and then held isothermally for 2 minutes. The furnace was then heated at 5°C/min to 70°C unless otherwise noted. The furnace was then held for 5 minutes at the maximum temperature before being cooled back to -40°C. This measurement was performed twice along the rolling direction, followed by one cycle each in the transverse and normal directions. The linear CTEs along these three directions were calculated as an average of the endpoint-to-endpoint linear slope during cooling from 60 to -15°C as measured during the second through fourth thermal cycles. However, in this case two temperature limits were attempted. In the first attempt, the stabilized A_S temperatures observed in DSC for a given reduction amount were used as the limit, and for a secondary TMA sample cut from each processing level the maximum heating temperature was simply 70 °C. This allowed for examination as to whether staying below the undeformed A_S of NiTi would have any effect.

3.4 Tension examination methods

3.4.1 Monotonic and iterated deformation for thermal expansion

For tension testing in TiNb micro-tension (gauge length 8 mm, gauge width 3 mm) dogleg shaped columns were cut through the material via wire EDM. These columns were then sectioned into tension samples of 1 mm (TiNb15) or 1.5 mm thickness and samples at the surfaces of the ingot where quench rates would be inconsistent were removed from the sample pool. The brass layer deposited on the surfaces by EDM was retained after cutting as it gives a consistent roughness, allowing for good resistance to extensometer slip. Identical methods were used for preparation of NiTi tension samples; the NiTiPd samples were acquired after having been previously prepared in the same manner. For NiTi, samples were reduced to between 0.8 and 1.5 mm thickness, while for NiTiPd samples were deliberately cut down to 0.5 mm thickness to reduce the total force before fracture and thus prevent grip slippage which occurred at the original 1.5 mm specification.

Examination was carried out through an iterated tension method. This was performed on a servo-hydraulic MTS test frame equipped with a high-temperature ceramic-extension-rod contact extensometer and with heating and cooling provided through the grips. Cooling was achieved by means of solenoid-gated liquid nitrogen fed through copper tubing wrapped around both the upper and lower grip, and heating was achieved by means of ohmic heating bands wrapped around the copper coils. Application of both cooling and heating in a specific grip was controlled by Eurotherm temperature controllers connected to thermocouples at the base of each grip. A contact thermocouple was attached at the center of each tension dogleg during installation to measure the approximate temperature of the material. As a final step during installation of each tension sample, the operating volume was wrapped in fiberglass insulation. To ensure firm contact of the extensometer rods the machine would be commanded to reach 100 N of force and return to standby while the response was monitored.

At this point room-temperature monotonic testing until sample failure could instead be carried out without need of the fiberglass insulation, if so desired. This allowed for capture of basic mechanical properties for the alloy systems being investigated.

The actual iterated tension experiment was constructed out as a series of consecutive cycles each constituting of a 'deformation' and 'temperature' step. In each cycle, the tension machine would be instructed to pull in displacement mode at 0.004 mm/s until reaching the specified engineering strain target as measured by the extensometer. Upon reaching the target strain, the machine would then unload in force mode at 20 N/s until it returned to the 10 N standby force. This constitutes the 'deformation' step. For the first cycle when no deformation is to be applied, the machine would instead pull in force mode to some arbitrary stress target - usually 100 MPa - to ensure the extensometer is seated fully and then returned to the standby force.

Following the return to standby force, the machine was then instructed to heat the grips up to the limit temperature outlined previously at 10 °C/min, followed by an isothermal step of between 2 and 5 minutes. Following this isothermal period, the machine was then instructed to cool the grips down the experimental minimum temperature (which varied depending on age of LN2 tank and other factors) at the same 10 °C/min. The temperature target was then held isothermally from 5 to 12 minutes to improve the achievable sample temperature minimum, which was normally ~10-15 °C above the target grip minimum. Following this, the machine would then return the grips to 30 °C, the deformation temperature, and hold isothermally for up to 4 minutes to bring the system back to equilibrium. This constitutes the 'temperature' step.

At this point the cycle ends, and the next deformation step to the new target can be started. During each step in the cycle the centerline temperature, force and extensometer readings are recorded continuously. As the uninterrupted temperature ramp is during cooling, this is the primary portion of the temperature cycle which was used to calculate the linear thermal expansion reported in this work. In this way the material was deformed iteratively in situ, and the thermal expansion response at each discreet step along the deformation pathway could then be examined.

3.4.2 Extension for examination of elastic modulus

To expand the examination beyond thermal expansion and measure the evolution of elastic modulus and elastic modulus with temperature, the program was further modified after the end of cooling to incorporate a 'stepwise pull' step. When active, the return to 30 °C outlined in the temperature step would be deferred to allow for a predetermined number of evenly spaced stepped heating intervals from the minimum to the maximum grip temperature. At the end of each interval the grips would be held isothermally for at least 3 minutes to allow the sample to equilibrate before the material would again be ramped to 100 MPa and back to 10 N at 20 N/sec. After reaching the maximum temperature the sample would then be allowed to return to 30 °C and the subsequent deformation step could then be initiated.

In all but the most original versions of this testing protocol, an additional 'pre-pull' to 100 MPa would be carried out before the main pull to 'reset' the material before acquiring the reported result. This often would be required on the first step after large amounts of cooling to fully reset the strain value and was extended to every point simply to homogenize methodology. In the most recent versions of this test, most notably Ext.66 and N4, additional pulls to arbitrary higher stress limits inside the elastic region were also incorporated into the stepwise pull step. These pulls would always follow the 100 MPa pulls, and also included a pre-pull to the same force target which immediately proceeded the 'data' pull.

For nickel-rich NiTi, the use of tension rather than TMA was selected for examination of properties. These samples were however deliberately cut with sufficient width to allow for tension samples to be cut in the transverse direction. This allowed for the examination of CTE and elastic modulus properties in both the rolling and transverse directions, rather than unidirectional or single-property evaluation seen in TiNb, NiTi, and NiTiPdTa.

3.5 Methods used in preliminary studies

While being simply variants of methods already described previously, some additional methods which have been utilized do deserve some additional elaboration here. Namely:

i. The first method is a planar directional study via TMA. In this test, $TiNb_{21}$ and $TiNb_{24}$ have been rolled to 50% reduction. After the rolling, TMA samples of 5 mm square and sample thickness are cut at orientations ranging from 0 through 90 degrees relative to the rolling direction, with the target being the inclusion of 10, 20, 30, 40, 45, 50, 60, 70, and 80 degrees orientation when material availability permits. Using the method outlined previously for use on the Q400 TMA, these samples are measured along both the orthogonal directions in the rolling plane. This allows for an examination of the evolution of the thermal expansion as a function of orientation in the rolling plane after significant deformation.

ii. For reasons similar to variant i. above, namely the pursuit of ways to tune the CTE after significant deformation rather than through the direct method, a new iterated tension method has been recently devised for use on rolled material. In this approach, the maximum heating temperature rather than the sample strain is being iterated. In this setup, the end point of a cycle is the heating not to 30 °C after cooling, but rather to the same maximum temperature as defined at the end of the initial heating. For each cycle, reaching the next heating target is then the first step followed by cooling and reheating. It is anticipated that this method, by triggering partial transformation of martensite into the parent phase with accompanying destruction of texture, can accomplish tailoring of CTE by increasing the CTE value above the baseline maximum negative CTE. This simultaneously raises the maximum usable temperature by redefining the A_s as being that of the remaining martensite still being athermally stabilized by the prior deformation. It is thus anticipated to be a powerful addition to the overall toolbox. This method has been only attempted as a proof-of-concept to this point and initial results have not been as anticipated.

iii. To create a preliminary examination of the effects caused by thermal cycling, some rolled TMA samples for $TiNb_{20}$ and $TiNb_{22}$ were placed into a heating sandwich comprised of two pieces of high-temperature polymer films heated by ohmic resistance controlled via an ARDUINO microcontroller coupled with a series of thermocouples measuring the film temperatures. To create one thermal cycle, the surrounding material would be heated to 80 °C and allowed to sit for a suitable time (approximately 10 minutes) so that the metal samples would be allowed to equilibrate with the films. At this stage, the heating would be deactivated while a fan would be turned on by the controller to accelerate the system’s return to room temperature. After the sandwich had come to nearly room temperature (30 °C) and another suitable time for equilibration had passed, the cycle would be considered complete and another would be started. This would be continued until the desired number of thermal cycles had passed, at which point the samples would be removed from the sandwich and their orthonormal CTEs would be examined via TMA using the methods outlined in 3.3.3. If more cycles were desired after this point, the samples would then be returned to the heating system.

CHAPTER IV

EXAMINATION OF CTE IN NITI AND EVOLUTION OF BULK CTE AND STIFFNESS AS A FUNCTION OF TENSION DEFORMATION

This chapter investigates the effects of temperature and different deformation amounts on equiatomic nickel-titanium alloy.

4.1 Synchrotron Examination of Undeformed Martensitic Equiatomic NiTi

The typical integrated two-theta estimation of the area detector data for various temperatures is presented in Figure 4.1(a). The indexed peaks are all for the B19' monoclinic martensite phase, and it can be observed that the count intensity diminishes slightly overall as the temperature of the sample decreases, with the highest count rates occurring above 10 °C. This is most likely caused by some degree of fogging and later freezing of ambient moisture despite the use of the nitrogen purge gas, which will slightly attenuate the beam. The lack of visible austenite peaks presents a strong argument that this material has quenched into very nearly complete martensite, which is a result reflected in all thermomechanical approaches studied in this chapter. Key peaks identified in the indexing of this two-theta scan include the orthonormal directions (002), (020), and (200), as well as the strong peaks $(11\bar{2})$, (012), (110), (022), and (220).

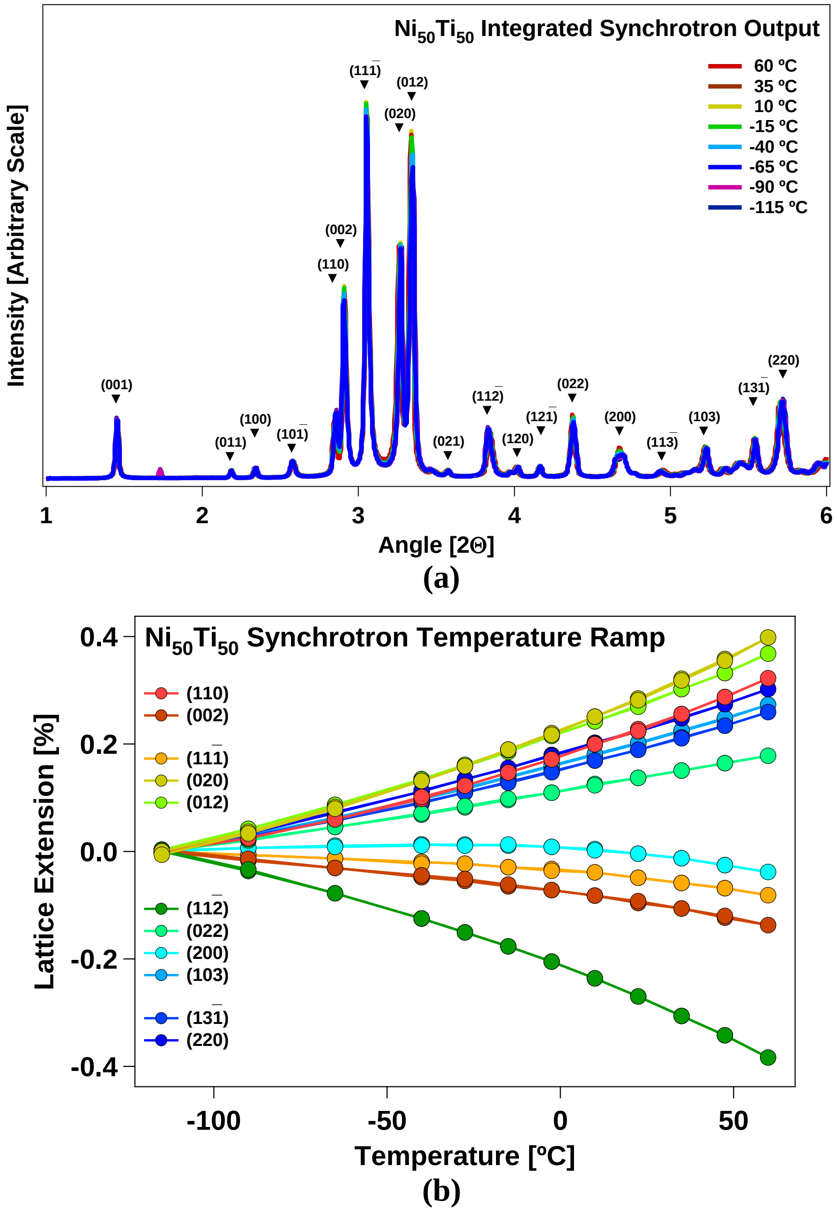

Figure 4.1 Undeformed equiatomic NiTi in synchrotron. (a) Two-theta estimation of the synchrotron area detection at various temperatures while being cooled from 60 °C, determined via integration of the detector from 1 to 6 Θ-degrees equivalent. Indexed peaks are indicated. (b) Crystalline strain-temperature response as determined in the same temperature range for indexed peaks.

Comparison of the peak locations for each of the temperatures scanned in equiatomic NiTi can, when set against the dimension of a reference temperature, allow for quantification of the change in crystalline lattice strain as a function of temperature. The results of this comparison when setting the initial -120 °C as the reference is illustrated in Figure 4.1(a). It can firstly be observed that the apparent thermal expansion (the slope of the strain vs temperature fit line shown in the figure for each peak) of the orthonormal (020) peak is strongly positive. This contrasts with the other orthonormal directions, which both demonstrate overall NTE across the temperature range. This behavior is also temperature dependent, as the NTE is much less or nearly zero for the (200) peak when below room temperature while the (002) peak shows a lesser response to the increase of temperature. It is highly apparent that the CTE response of the NiTi monoclinic crystal is not aligned with the orthonormal lattice parameters as it is in the NiTiPd or TiNb case, as the remaining two NTE peaks, $(11\bar{1})$ and $(11\bar{2})$ both are hybridized orientations. The implications of these two peaks demonstrating NTE, and the second showing greater NTE, is that wildcard having such influence upon the CTE of this crystal is the changing β angle which is slowly decreasing throughout this temperature range. This has the effect of amplifying the smaller NTE moments in these two directions. The effect of the angle change is variable, and it should be noted that it does have this same synergy in other orientations such as the $(13\bar{1})$ peak which interacts very differently with the β-angle. The other strong peaks – the (110), (012), (022), and (220) – all point towards interactions where the low/negative CTE in the a- and c-directions create a slight reduction on the positive thermal expansion contribution from the b-axis direction in the rest of the cell.

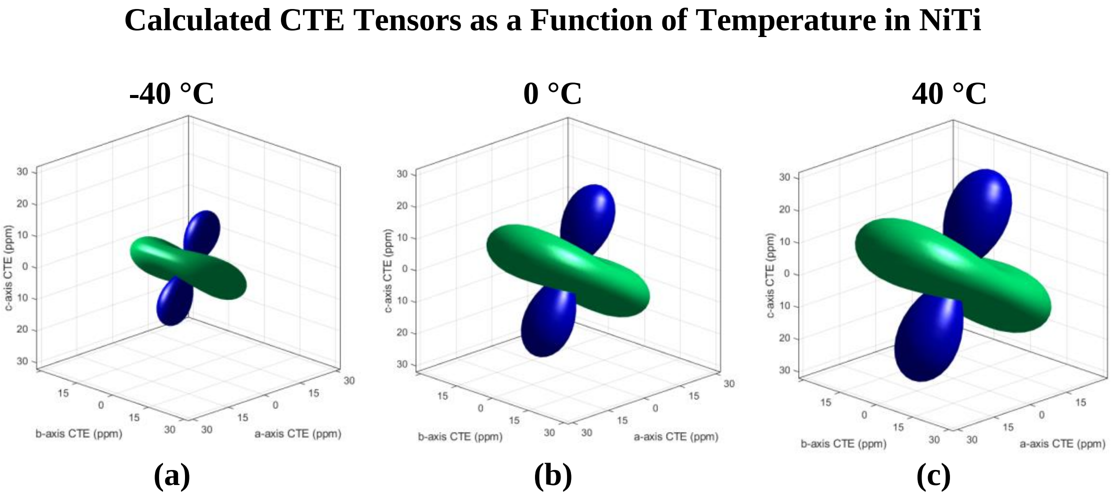

Figure 4.2 CTEAS Plotted Thermal Expansion Tensors for undeformed NiTi at various temperatures. Left to Right: -40, 0, 40 °C.

The result of these interactions can be further visualized by the CTEAS estimation of the crystalline thermal expansion tensor. Figure 4.2 gives the estimated tensor for (a) -40 °C, (b) 0 °C, and (c) 40 °C. The temperature dependence is quite visible, with the overall CTE magnitudes in any given direction increasing as the temperature is raised over the 80 °C window represented by these three diagrams. The direction of maximum negative CTE (blue) is indicated as being at an angle in the plane of the a- and c- axes, and is affected deleteriously by straying into orientations which include contributions from the b-axis, as predicted by the strain responses seen in Figure 4.2(b). The increased CTE magnitudes indicate a higher overall incremental influence from thermal sampling at elevated temperatures, and likely points towards a thermodynamic influence causing a decrease in the energetic barrier to switching. In any case, the apparently ideal orientation for peak NTE in bulk material will occur outside of the orthonormal c-axis orientation in the tension axis, which may be difficult to achieve as the deformation torque effect on the a-axis will be considerably less than that of the b- and c-axes, causing the texture to shift into a non-ideal configuration.

4.2 Influence of deformation upon crystalline CTE

Application of deformation, especially as deformation must be increasingly accommodated by slip and dislocation generation in the sample, is expected to increase the energetic barriers to thermal sampling and thus decrease the CTE anisotropy of the material. To verify this, four pre-deformed samples were examined by scanning in synchrotron at 20 °C intervals from -40 to 60 °C. The results are shown in Figure 4.3. The four subdiagrams (a) through (d) are set to the same strain and temperature ranges, allowing for easy visual comparison. Inspection of the four samples indicates a few changes in behavior. Firstly, it should be noted that for the final case – 30% cold rolling – there is a significant drop in image quality indicated by the significant decrease in the number of indexed peaks. This was caused by a both a notably decrease in peak-to-background ratios and peak broadening. Such decreases in image quality are to be expected as the rolling process results in higher effective deformation amounts. The 30% cold-rolling material should be considered as severely plastically deformed in the NiTi case and will have significantly smaller grains and quite high dislocation density, both of which will degrade and broaden the diffraction peaks.

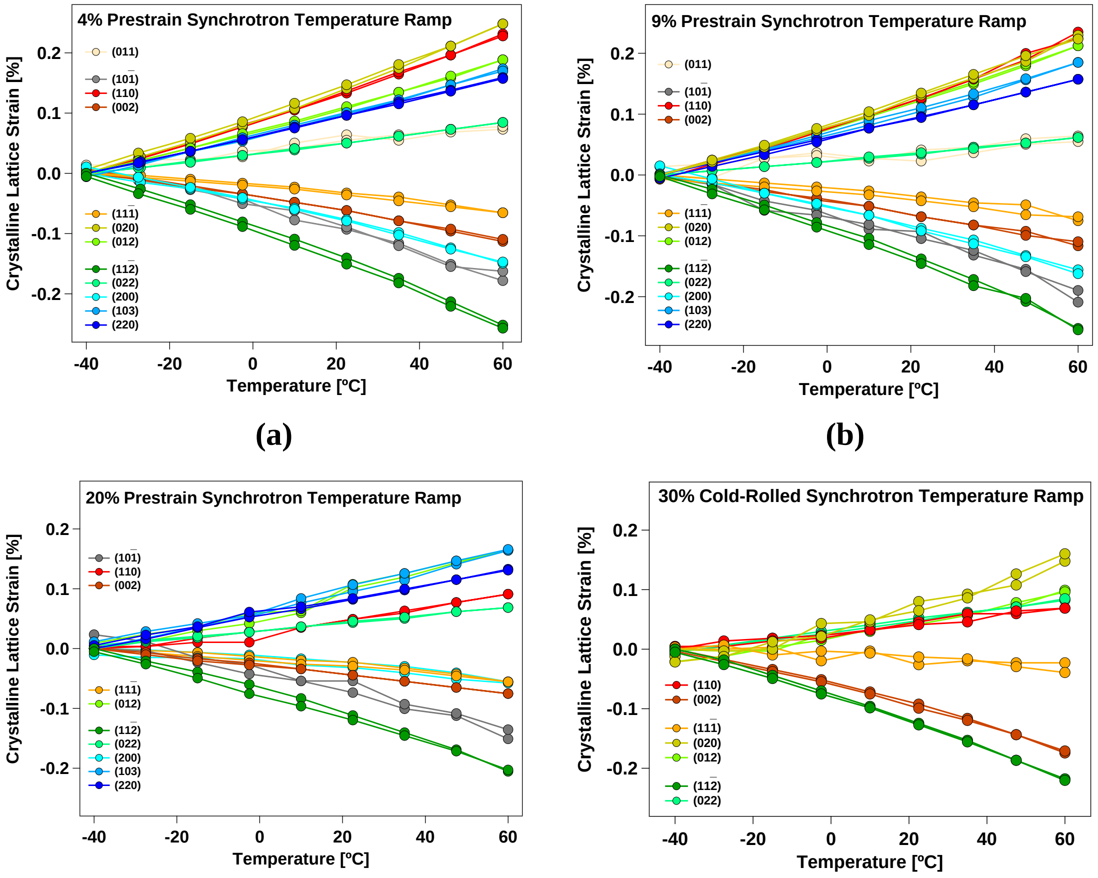

(a) **(b)**

(c) **(d)**

Figure 4.3 Comparison of crystalline strain-temperature responses in various deformed equiatomic NiTi samples. (a) 4% tension prestrain (b) 9% tension prestrain (c) 20% tension prestrain (d) 30% rolling reduction.

Despite this limitation, all samples still provide more than sufficiently good clarity to use for analysis. The differences in the overall CTE anisotropy between 4% and 9% prestrain are not immediately obvious, and they appear mainly to be remarkably similar results overall. However, there is a strong and obvious contrast between the 4% and 9% prestrains, and the 20% prestrain. Here the overall anisotropy is significantly decreased with the maximum NTE only realizing a -0.21% strain change in the same temperature window that results in a -0.25% change in the 4 and 9% cases. This similarly is reflected in the PTE orientations. This new behavior is aligned rather closely to the strain change observed in 30% cold-rolled material, which shows similar NTE magnitude, although interestingly with a significant degradation in the apparent maximum PTE of the (020) peak. This may be due to a low proportion of the (020) peak being aligned with the beam direction in the highly-rolled case, causing a bias in the response.

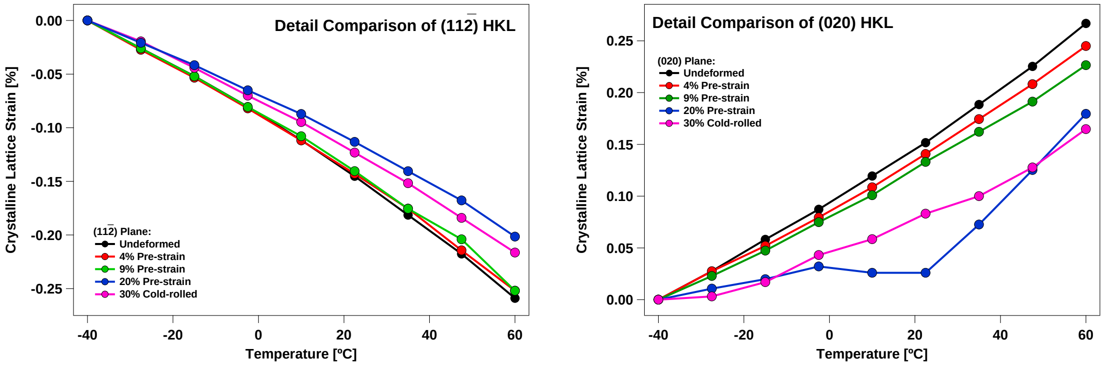

(a) **(b)**

Figure 4.4 Detail compare for the two largest CTE peaks in NiTi of the crystalline strain response verses temperature as a function of deformation. (a) $(11\bar{2})$ peak (b) (020) peak.

This anisotropy is examined further in Figure 4.4 where the largest NTE and PTE peaks, the $(11\bar{2})$ and (020) respectively, are compared directly for the various deformation forms. In Figure 4.4(a) it can be observed that the 4 and 9% strain cases result in only a small deviation in NTE from the undeformed NiTi strain response to temperature along the former direction. Again, the contrast in 20% prestrain is clear, with a significant deviation from the NTE observed in undeformed material. The rolled case, intriguingly, offers a smaller deviation in the observed NTE, despite the nominally higher deformation amount. The pattern holds again in the (020) case of Figure 4.4(b), although here it can be clearly seen that the comparison is made difficult by a systemic error which is occurring in both the 20% prestrain and 30% rolled cases. Again, it appears that significant deformation results in a harm to the precision of the peaks least inclined to align in the direction of deformation. However, when allowing for the increased uncertainty, it still appears that the higher deformation situations are once more the areas where significant anisotropy changes are encountered in the crystal.

4.3 Mechanical properties and iterated deformation response for thermal expansion

4.3.1 Mechanical response

Why this change in behavior appears to occur between 9 and 20% tension strain may be answered by examination of the monotonic tension response for equiatomic NiTi, shown in Figure 4.5(a). The tension response to increasing displacement can be broken into four approximate regions, classed as (I), (II), (III), and (IV). The (I) region represents the initial elastic response. This is followed by a low-force stress plateau in region (II), where variant reorientation and detwinning is the primary mode of deformation and occurs without significant strain hardening. The 4% prestrain sample originates from the late portion of this region. The following region (III) deformation sees a high rate of strain hardening which tapers towards the end of this region. It is expected to consist of a mixture of different deformation responses, with detwinning continuing to be dominant until the tapering is initiated at approximately 12% strain. This implies that the 9% prestrain case corresponds with this late detwinning deformation response but is still located well before the onset of primarily slip response. This contrasts with region (IV), which is dominated by plastic slip. The 20% prestrain lies well into this region. 30% cold-rolled material corresponds with an equivalent strain value well beyond the fracture strain in tension and is heavily dominated by slip as well.

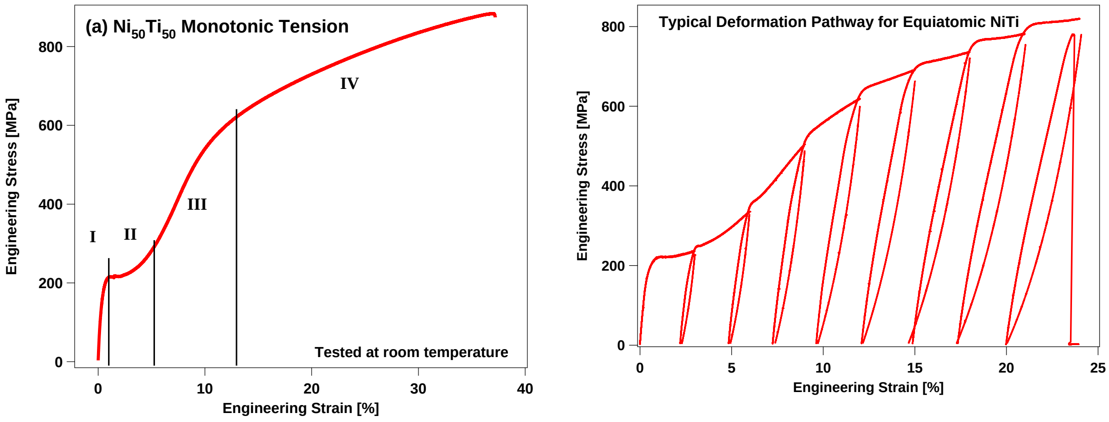

(a) **(b)**

Figure 4.5 Mechanical properties of equiatomic NiTi. (a) Typical monotonic tension response, with approximate regions of deformation behavior delineated. (b) Illustrative stress-strain response for the NiTi iterated tension deformation test process.

The deformation regions associated with each sample provides good guidance as to the underlying cause for the change in the CTE anisotropy with deformation amount.

The 4 and 9% prestrain cases represent primarily variant reorientation and detwinning, with a small amount of total slip and dislocation generation. The result is a minimal effect on the energetic barriers for thermal excitation and hence a small net change to the CTE response. This contrasts well with the 20% prestrain and 30% cold-rolled cases, which both being representative of slip-dominated processes result in large generation of dislocations and hence an increase to the energetic barrier for sampling and hence a lower overall rate of CTE as the compensatory transformation rate is decreased.

A typical engineering stress-strain response for the iterated deformation process is shown in Figure 4.5(b). Connecting the plastic deformation portions of the curves only, a quick comparison 4.5(a) shows that the stress-strain response matches well to the monotonic response. This appears to imply that the response to deformation is approximately equivalent between the different deformation approaches, and that the interruptions for heating and cooling applied in the iterative case are not creating significant effects on the mechanical response. Examination of the elastic response at the beginning and end of each deformation step indicates an increasingly large elastic hysteresis as both the maximum stress and total deformation amounts are increased.

4.3.2 Thermal expansion response to iterated deformation

The strain response of equiatomic NiTi to iterated deformation during cooling of the sample after heating to the maximum working temperature is demonstrated in Figure 4.6(a). The engineering strain change in undeformed material (black) demonstrates a linear positive thermal expansion response as expected. Also as expected, the material demonstrates decreasing tension direction CTE as deformation is applied to the sample, with the material transitioning to NTE. What is surprising, perhaps, is the rapidity of this NTE onset, as the deformation required to transition to zero net CTE is less than 3% total engineering strain (gold), and the net CTE appears to have dropped dramatically at only 1% applied strain (red) – a point at which very little total plastic strain has been applied after the initial elastic response. These first few strain curves indicate that the evolution of the texture – and hence CTE – in NiTi is quite rapid during the initial deformation stages.

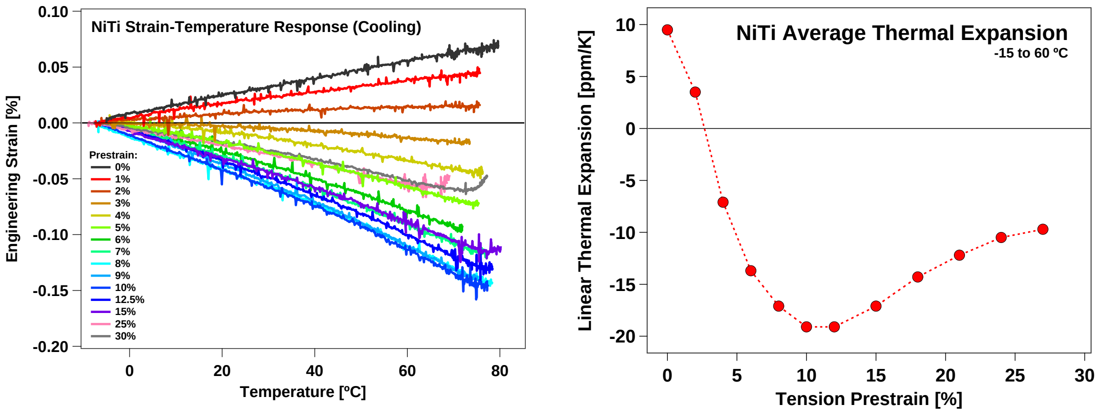

(a) **(b)**

Figure 4.6 Thermal Expansion Response of NiTi. (a) Strain-temperature response during cooling from the maximum heated temperature at each prestrain level. (b) Linear average thermal expansion measured in a 75 °C window as a function of sample prestrain.

This evolution of decreasing CTE only continues beyond the 3% tension strain required to elicit NTE behavior and shows that the NTE will decrease further until reaching approximately 9 to 10% tension strain. At this point, the engineering strain response appears to be unchanged between the two deformation levels, and continuing increases in the tension deformation result only in the strain response decreasing as a function of temperature. This is illustrated further in the adjusted CTE verses tension prestrain curve shown in Figure 4.6(b). Here the trends previously observed are confirmed, with the CTE rapidly evolving from 0 to 10% applied strain in the sample with a peak NTE of -18 ppmK^{-1}, followed afterwards by an apparent reversion in the CTE until reaching an apparent asymptote of approximately -10 ppmK^{-1} when approaching 30% engineering tension strain.

These CTE responses correspond well with the stress-strain response regions identified in the previous section in Figure 4.5(a). The most rapid evolution of the CTE occurs in the region (II) portion up to 5% strain, with a decreasing rate of NTE increase in the strain region between 5 and 10% during the region (III) deformation. The 10% strain point corresponds with the initiation of the stress taper in the late portion of the region (III) deformation and not the onset of the region (IV) deformation, serving as a reminder that these regions are delineated approximately. The full reversion does not begin in earnest until crossing 11% strain, which does correlate with crossing the transition into region (IV). The onset of slip-dominated deformation is deleterious to maximization of NTE, with a small transition occurring after the conclusion of primary variant reorientation and detwinning.

4.3.3 Evidence for texture-driven CTE via texture mapping

Examination of the textures which are present in the deformed samples via synchrotron provides additional illumination as to the overall orientation of the martensite in these materials. Figure 4.7 shows the textures along the tension direction as estimated by MAUD and plotted as inverse pole figures via MTEX. Each texture map is represented as a semicircle, where the extreme left and right points on the pole figure represents the [001] and [00$\bar{1}$] orientations, the center top of the figure represents the [010] orientation, and the bottom center represents the [100] orientation. Examining all four deformation cases, the primary orientation proclivity in all situations is towards the c-axis orientation, with the texture being most strong in the 9% strain case. In point of fact, the 9% case represents what is essentially an amplification of the texture observed in the 4% strain case, where the same orientations ([001] through to [111]) are more strongly represented and the other orthonormal directions ([100] and especially [010]) are diminished in comparison. This points again towards the continuance of variant reorientation and detwinning between 4 and 9% strain and the transition from region (II) to region (III) deformation.

Inverse Pole figures along Tension Axis for Deformed NiTi

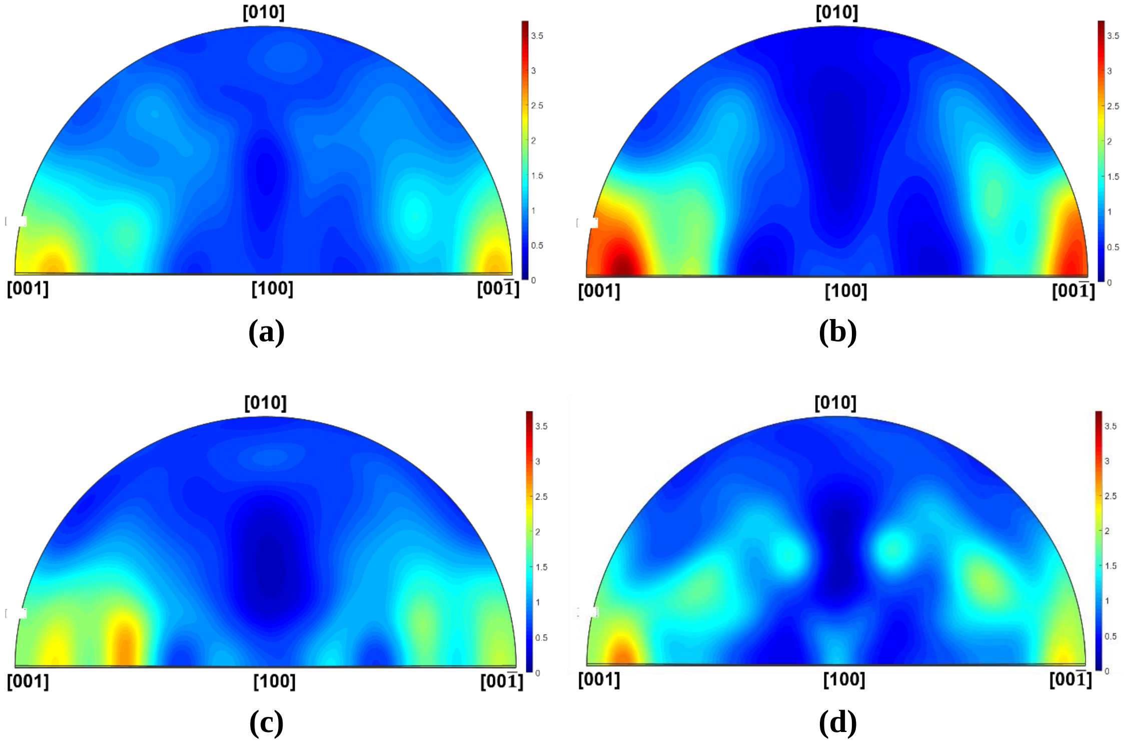

Figure 4.7 Z-axis (tension direction) texture estimation via MAUD of synchrotron texture scans for the deformed NiTi tension samples. (a) 4% tension pre-strain (b) 9% pre-strain (c) 20% prestrain (d) 30% cold-rolled.

Compared to the 4 and 9% strain cases, the 20% strain example more strongly recalls the texture seen in the 4% case, with remarkably similar net orientation peak strengths. In the 20% case there is more of a binodal nature to the overall alignment, with two subpeaks both visible located between the [100] and [001] – although these same subpeaks can be seen in the 4% case with more disparity in the strengths between them. Despite these small differences, the overall texture in 4 and 20% strain cases match quite strongly, and it should be noted that the expected net average CTE seen in Figure 4.6(b) is in close agreement at those two deformation levels. This appears to indicate a high degree of equivalency despite the quite different deformation circumstances.

Examination of the texture in the 30% rolled case indicates some change in the specific details of the texture map (such as lack of a bimodal peak near the <001> orientation, as well as a larger representation of orientations which lie closer to the [100]-[010] plane) but a high degree of similarity in the general contours. Examining all four texture maps, it appears that the cause behind the larger CTE observed in the 9% strain case is due not to a higher degree of a preferential orientation, but rather a significantly higher absence of orientations with large PTE moments. This is evidenced by the low relative values of orientations along the [100]-[010] plane and especially in the region of the [010] direction when compared to the other deformation levels. The texture maps shown here make a strong case that the evolution of texture in NiTi during tension is a rapid onset of orientation towards the c-axis via variant reorientation and detwinning, followed later by a ‘smearing’ effect whereby portions of the material are reoriented towards other directions by the act of slip in response to deformation, which while not destroying the preferential texture entirely is capable of reducing its overall strength. When combined with the slip effects upon the net CTE anisotropy, this likely serves as a strong explanation regarding the overall evolution of the CTE as a response to deformation.

4.4 Elastic Modulus Response to Deformation

While the CTE was measured during the continuous cooling of the sample, the elastic modulus instead measured in discreet temperature steps while the material was reheated from its minimum temperature. To eliminate instabilities caused by the large temperature changes, the sample was ‘pre-pulled’ to the maximum testing force to shake it down each time before the force ramp intended for measurement was performed. The elastic response of a NiTi tension sample subjected to 24% cumulative strain during deformation as a function of temperature is illustrated in Figure 4.8(a). Here the sample is subjected to a maximum stress value equivalent to approximately 90% of its anticipated yield strength during elastic loading.

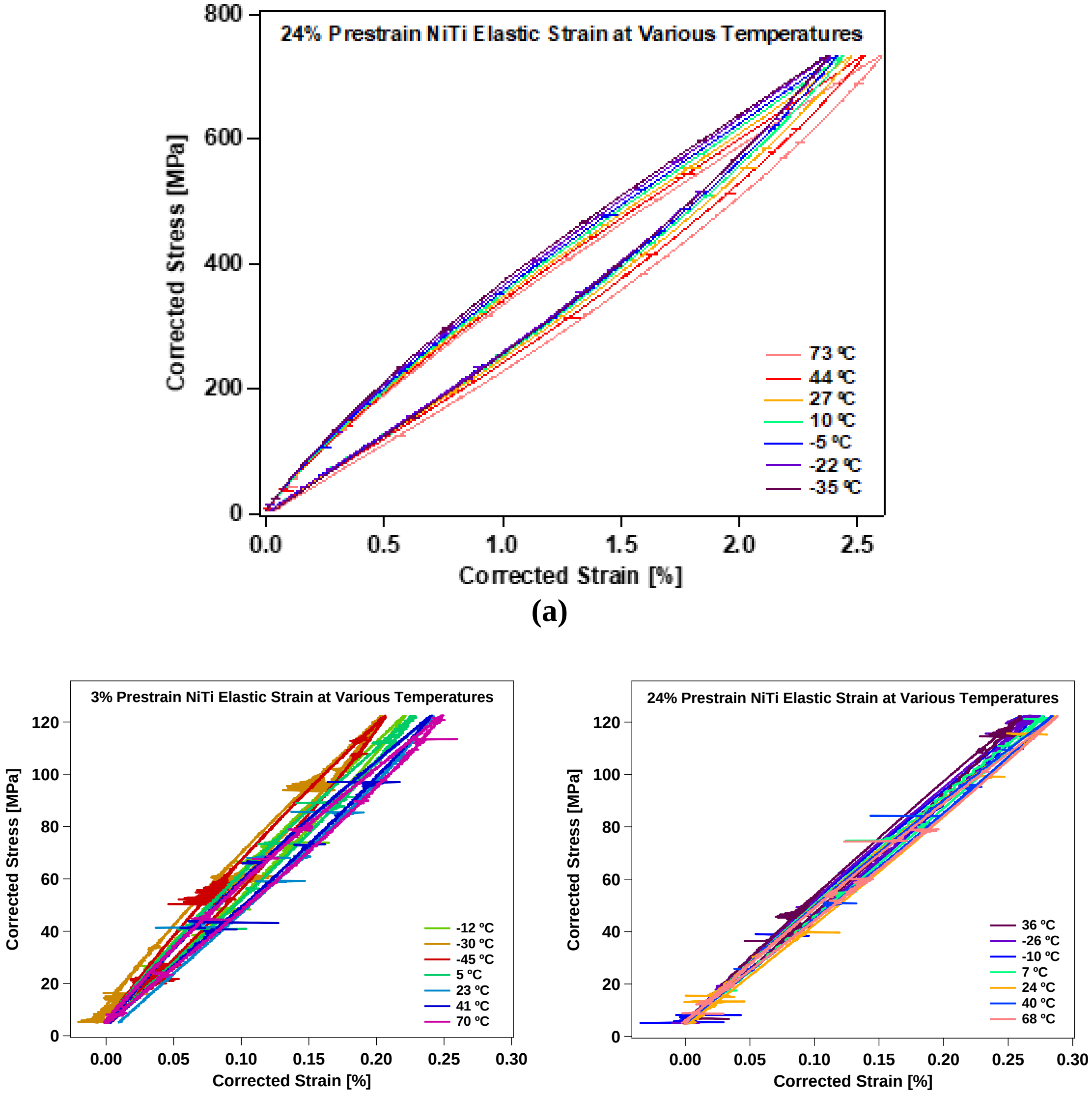

(a)

(b)

(c)

Figure 4.8 Illustration of the thermal elastic cycle response in NiTi at specific tension prestrain. (a) Adjusted stress-strain response during loading and unloading with a 700 MPa loaded stress target, with common start point to illustrate direction of change in overall elastic response with temperature. (b), (c) Detail to 120 MPa maximum, showing the response considered for comparison between deformation levels with 3% and 24% tension prestrain illustrated.

In examining these elastic response curves, some considerations are apparent. The first is the large elastic strain hysteresis observed earlier in Figure 4.5(b). The second is the existence of a small linear stress-strain region between approximately 0 and 150 MPa located at the beginning of each elastic loading curve. The third and most important in the context of examining the elastic modulus response to temperature, is the relatively small amounts of strain deflection experienced by the sample at the maximum load while the temperature increases. Over the approximately 100 °C temperature window examined, the total change in strain at the maximum stress is less than 0.3%. This equivalates to an average stiffness change over the temperature window of less than -30 MPa/K, which is less than have the rate of stiffness change in conventional steels. However, it can be practically observed that the quantification of the elastic modulus is difficult and likely uninformative in the presence of such large elastic hysteresis. To compensate and ensure accuracy, the approximately linear tangent region below 150 MPa will instead be examined.

Two examples are provided in Figures 4.8(b) and (c). In (b), the elastic response to temperature is illustrated for the 3% strain case, and in (c) the same is shown for the later 24% strain maximum in the same sample. Both illustrate roughly similar behaviors where the apparent elastic modulus decreases as the temperature increases as is conventionally expected although the rate of this change is significantly decreased in the latter case. Of importance when discussing the potential validity of this examination is the size of the apparent strain hysteresis in both cases and whether it should be considered disqualifying. When compared to the large hysteresis illustrated in the (a) subfigure it is clear that the relative amount of strain mismatch is lower in both these cases, with the hysteresis being nearly eliminated in the 24% strain situation. Moreover, the elastic hysteresis does not demonstrate multiple regions of response in the way seen in the (a) subfigure, and rather a small deflection of the overall apparently linear response. As such, it was judged that proceeding with the analysis in the tangent region would be a valid comparison, although care should be taken to verify that no elastic loading/unloading loop would become too irregular.

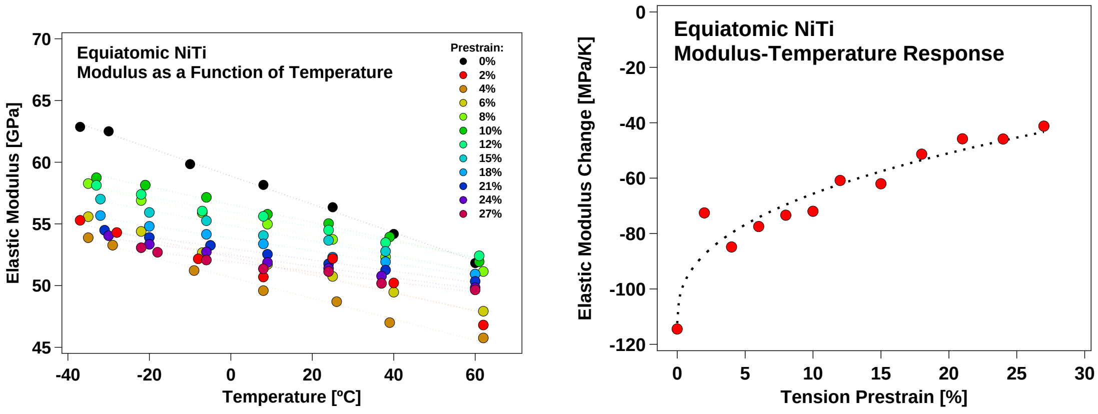

(a) (b)

Figure 4.9 Examination of NiTi elastic response to temperature. (a) Engineering elastic modulus measured as an average of the loading and unloading steps in the cycles illustrated previously compared as a function of temperature and prestrain. (b) Evolution of the overall average slope of the elastic modulus due to temperature, charted as a function of applied prestrain. Measured slope value of -35.7 MPa/K in 30% rolled NiTi indicates non-asymptotic behavior in the region studied.

The results of this analysis for NiTi are summarized in Figure 4.9(a). Here the adjusted elastic modulus values (Appendix A) are given as a function of temperature for each of the deformation strain conditions applied to the sample. The undeformed condition (black) demonstrates the largest rate of stiffness change per unit temperature, and at the same time no sign change for the stiffness response is visible unlike in the

CTE case. Despite that, there is a clear decrease in the slope of the stiffness as a function of temperature as the deformation increases. Of note is the evolution of the elastic modulus for a given temperature as a function of deformation – the value of the modulus at room temperature initially decreases, reaches a minimum between 4 and 6% strain, and then slowly increases afterwards. This points to a likely correlation between the region (II) reorientation and the elastic modulus where the increased orientation towards the c-axis exposes the lower net E, while the second mode of detwinning encountered in region (III) now masks it again. As the texture of the sample is not evolving away from this lower-modulus configuration, this is most likely due to changing interface conditions due to twin boundary movement.

Figure 4.9(b) shows the net change in stiffness per unit temperature as a function of deformation. Here the stiffness change initially decreases at a rapid rate, to be followed by a quasi-linear decrease which continues through to the fracture of the sample. The evolution can be analyzed in three regions, where region 1 occurs between 0 and 5% deformation strain, region 2 occurs from 5 to 10% tension strain, and region 3 encompasses all deformation strain from 10% to fracture. The rapid evolution in stiffness response during region corresponds well with the initial reorientation which again favors the region (II) identified as the primary mover for the single-temperature elastic modulus previously. This is followed by a transition/stabilization phase where the decrease becomes more linear during the region (III) deformation identified as still resulting in net CTE decrease previously. Beyond this, the stiffness response to temperature will continue to decrease monotonically during the deformation associated with late region (III) and encompassing all of region (IV). The implications of this are that the initial reorientation mechanics where much of the c-axis orientation shift occurs once again is responsible for the bulk of the stiffness change, which diminishing effect as this reorientation mechanic is exhausted. What does not agree with the CTE trendline is the linear continuation of the stiffness change decrease observed in the third region of Figure 4.9(b). Although the rate of change is expected to decrease upon transition to severely plastic deformation (evidenced by the small improvement in the stiffness-temperature change to -37 MPaK^{-1} in rolled NiTi) this change remains linear prior to fracture in tension. This points towards an additional interaction which serves as the primary driver of the stiffness response to temperature. At present this is indeterminate, although several candidates such as interface shifts due to temperature fluctuations and dislocation interactions with thermal excitations are can be readily identified.

4.5 Summary and Conclusions

In this chapter the crystalline strain response to temperature and deformation was examined via synchrotron in equiatomic NiTi martensite. This was followed by use of mechanical testing via tension to examine the monotonic and iterative response to deformation, and the evolution of bulk CTE in the material as a response to iterative deformation. Further examination of the temperature-dependent elastic properties was enabled by discreet measurements carried out in this tension examination and overall CTE and stiffness responses were compared to the mechanical strain hardening as well as estimated textures of deformed samples. The following conclusions were reached:

1. For equiatomic NiTi it is possible to produce what appears to be a fully martensitic microstructure. This martensite displays large strain anisotropy as a response to temperature, with the [010] direction showing large positive CTE and the [100] and [001] directions small NTE. Influence from the collapsing β angle during heating causes the maximum NTE direction to evolve along a non-orthonormal direction, resulting in both the primary PTE and NTE orientations not being orthonormally aligned in their respective planes.
2. Application of significant deformation upon NiTi through either uniaxial tension or rolling reduction can reduce the overall crystalline anisotropy to a certain extent. The cause of this is attributed to the generation of dislocations causing an increase in the local barriers to thermal sampling.
3. Thermal expansion in the tension orientation evolves rapidly through 10% strain, whereupon the net CTE magnitude decreases before approaching an apparent asymptote. This correlates strongly with the orientation of the martensite due to texturing. The cause for the CTE reversion beyond 10% strain appears to be ‘smearing’ of the reorientation texture due to plastic slip in the material.
4. Stiffness is influenced by the texture of the martensite, although only to a minimal degree.
5. The stiffness change due to temperature is significantly affected by the orientation of the martensite, but after the onset of slip is affected to a strong (and possibly complete) degree by another presently unknown mechanic. Despite this uncertainty, the NiTi material is capable of reducing the rate of its stiffness

change due to temperature by more than 60% over the course of tension deformation.

CHAPTER V

EVOLUTION OF THERMAL EXPANSION AND STIFFNESS IN NITI$_{49.5}$PD$_{25}$Ta$_{0.5}$ DUE TO VARIANT REORIENTATION IN TENSION

The addition of palladium (Pd) to NiTi binary alloy acts a substitute to the nickel content, with the effect of a notable increase in the overall transformation temperatures relative to the prior alloy, especially when Pd has become the majority non-Ti element in the alloy [47-50]. The contrasting effect of the Pd elemental addition is to induce a shift in the martensitic configuration such that its martensitic structure moves from the ordered monoclinic to an ordered orthorhombic phase, while retaining a body-centered cubic parent phase. As a result, examination of the similarities and contrasts between NiTi and a NiTiPd alloy in terms of their respective anvar characteristics can help to illustrate how these properties are likely to evolve between different shape-memory systems.

The alloy used for this study, which is of nominal composition NiTi$_{49.5}$Pd$_{25}$Ta$_{0.5}$ (at%), was selected mainly due to budgetary and availability considerations. Relative to equiatomic NiTi alloy, it is expected to show an increase in maximum pre-deformation A_S of approximately 50 °C due to the palladium content [47], with an A_S of approximately 125 °C rather than the 75 °C of the equiatomic NiTi observed previously. The addition of a microalloying amount of tantalum (Ta) was likely intended to study whether it would allow for the effective creation of solid-solution strengthening as a defense against functional instability during thermal cycling in a manner similar to scandium [50]. It is not believed that this addition will have significant effect in this work as the material was not given thermal training for solid solution strengthening, and resultingly the material will behave in a manner sufficiently similar to a nominal composition of $NiTi_{50}Pd_{25}$.

5.1 Crystalline structure and thermal expansion of NiTiPdTa

The integrated two-theta estimation of NiTiPdTa is shown in Figure 5.1.

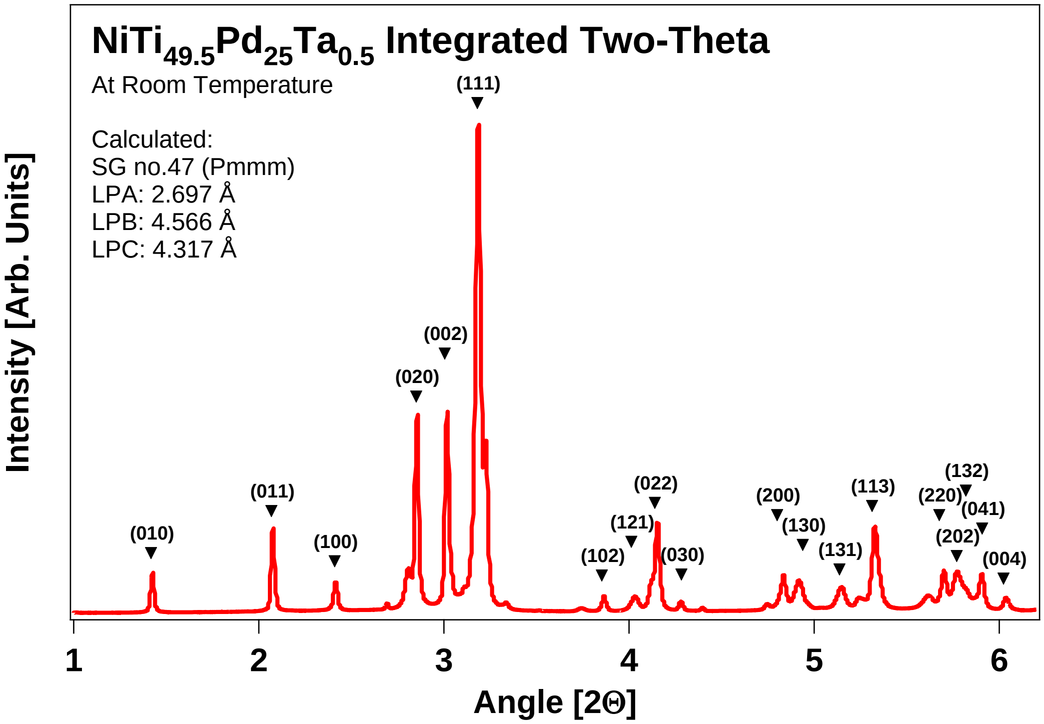

Figure 5.1 Two-theta estimation of the synchrotron area detection for NiTiPdTa used in this work at room temperature. Determined via integration of the detector from 1 to 6 degrees equivalent. Indexed peaks are indicated.

It can be seen that the material after quenching does manifest into its martensite phase, which has been calculated in this work as a *Pmmm* orthorhombic space group with a, b, and c lattice parameters of 2.697, 4.566, and 4.317 +/- 0.005 angstroms, respectively. This particular configuration lends itself well to clear delineation of the orthonormal HKL directions, as the (010), (100), and the (002) can all be found as their own distinct peaks, free of overlap with any other peaks.

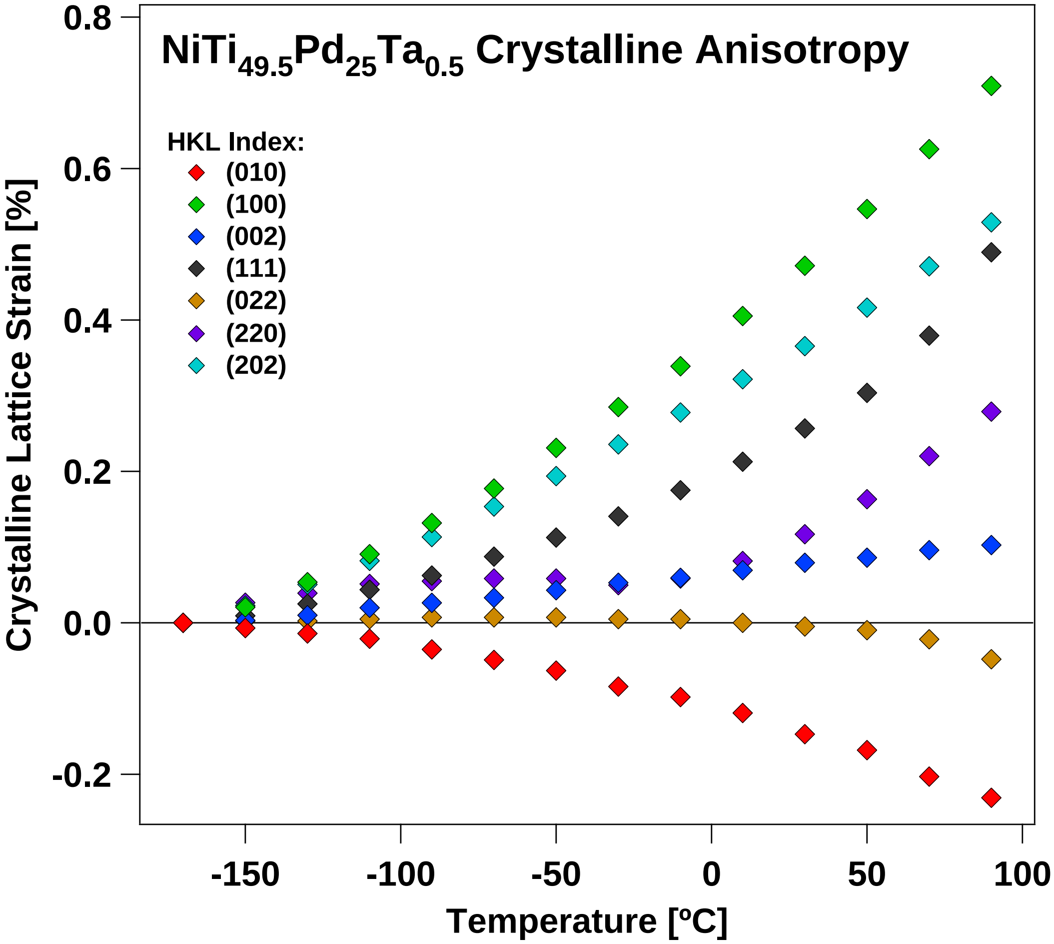

Figure 5.2 Crystalline stain–temperature response as determined by synchrotron for NiTiPdTa studied in this work. Orthonormal and major diagonal directions illustrated.

This clarity allows for the major HKL of the NiTiPdTa crystal to be easily estimated as a function of temperature, as can be seen in Figure 5.2. Here, the crystalline lattice strain relative to -170 °C in the orthonormal directions noted above as well as the (110), (111), (022), (220), and (202) peaks are all shown as a function of temperature. It can be noted firstly that relative to the orthonormal directions in NiTi alloy, the magnitude of the CTE which can be observed in the orthonormal directions of NiTiPdTa is considerably greater. In this material the behaviors of the [100] and [010] clearly dominate, as it can be seen in both the (022) and in the (202) peak travel that there are significant changes in their slope of strain as a function of temperature which reflect the accelerating rate of increase in CTE for both the (200) and (020) peaks. This overwhelms the relatively mild effect on the (022) and (202) peaks caused by the slight increase in CTE with temperature seen in the (002) peak. This stands in strong contrast when compared with the monoclinic NiTi martensite, which had its highest level of anisotropy in a non-orthonormal direction, due mainly to the influence of the change in the β-angle.

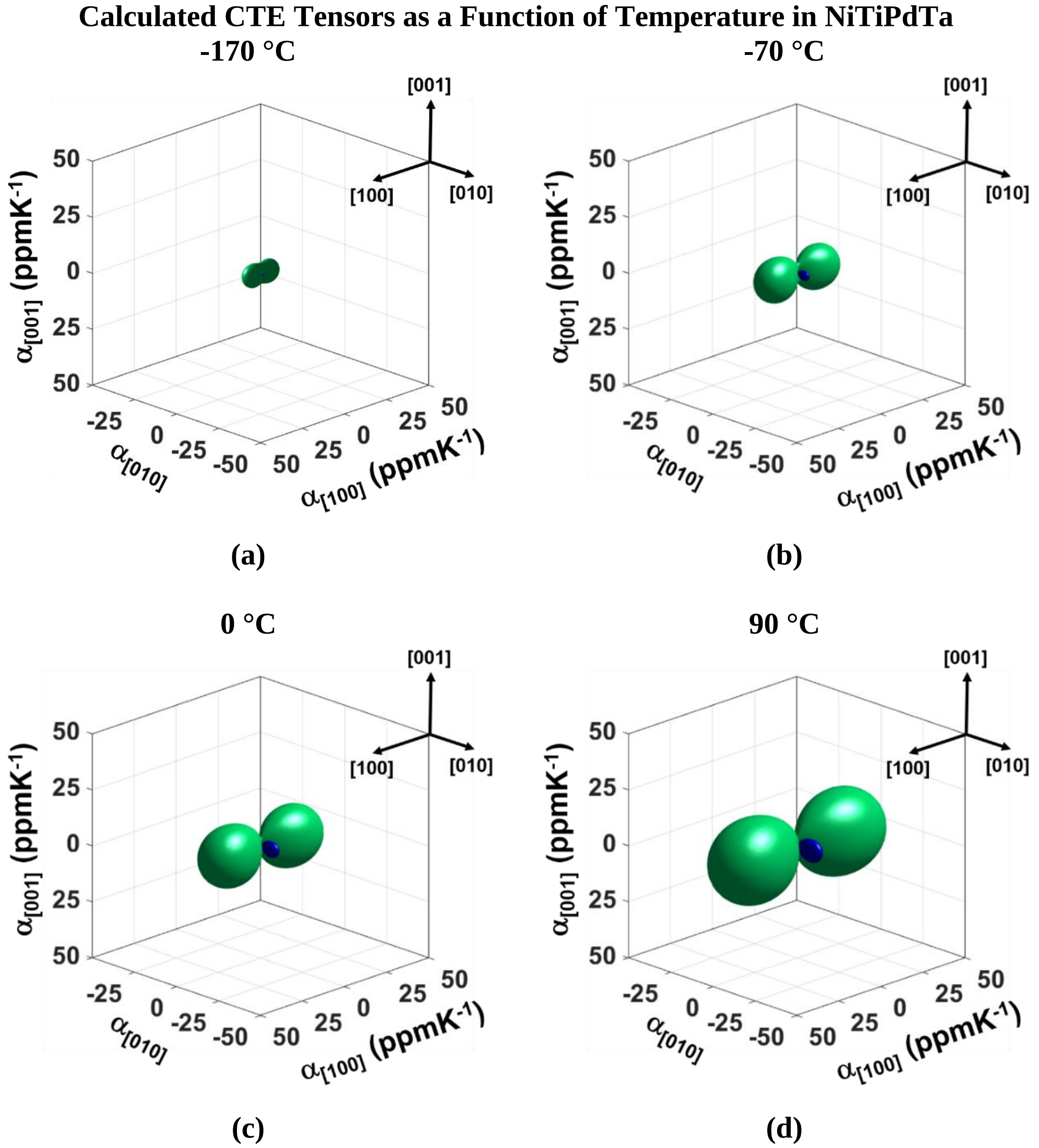

Figure 5.3 CTEAS plotted thermal expansion tensor at various temperatures.

Indeed, when examining the tensor of the thermal expansion at room temperature as calculated by the CTEAS software in Figure 5.3(a-d), it can be observed that the principle directions of the thermal expansion lie entirely along the principle axes. The point of greatest import for the tailorability of the thermal expansion lies along the b-axis, where it can be observed that the maximum magnitude of the negative thermal expansion at room temperature is only -12.2 ppm at room temperature, which is significantly less than the maximum negative CTE available in NiTi (-23.4 ppm) at the same temperature. If the percent utilization of the available negative thermal expansion due to deformation in tension is at all similar to the values confronted in NiTi, it would be reasonable to assume that the expected maximum negative thermal expansion magnitude would be approximately half that seen in the tension deformation of NiTi in the previous chapter.

5.2 Mechanical properties of NiTiPdTa

Figure 5.4(a) illustrates one thermal cycle of an undeformed sample of NiTiPdTa while held under a tension stress of 35 MPa (100 N), which was considered small enough to not provide any significant mechanical effect on the transformation temperatures.

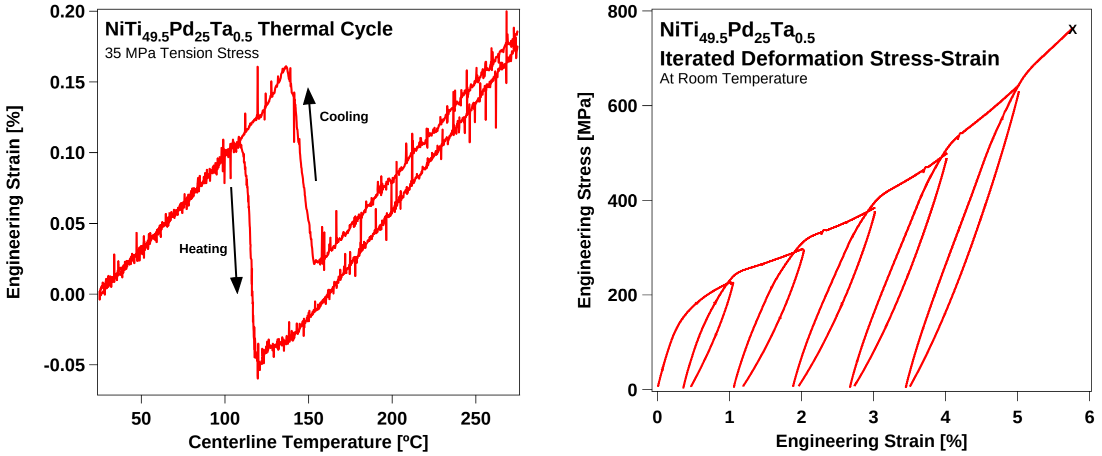

(a) (b)

Figure 5.4 Mechanical properties of NiTiPdTa. (a) Heat-cool cycle for undeformed NiTiPdTa while under small tensile loading. (b) Illustrative stress-strain response for the NiTiPdTa iterated tension deformation test process.

From this cycle it can be observed that the approximate A_S, A_F, M_S, and M_F temperatures of this alloy are 125, 135, 160, and 150 °C, respectively. These values are in approximate agreement with the expectations from literature [47, 48] and show that the effect from the Ta alloying addition is likely having minimal effect on the overall material. Relative to NiTi, the effect of the 25% Pd addition is indeed to increase the maximum temperature before transformation by approximately 50 °C and gives this material a working temperature window similar to most invar alloys.

Figure 5.4(b) shows the typical stress-strain path followed by a NiTiPdTa sample while undergoing iterative deformation as outlined previously. Similar to NiTi the monotonic tension behavior was found to be in good agreement with the iterated deformation curve and thus the stepped curve alone was included to demonstrate the mechanical response to deformation. Relative to NiTi, it can be seen that this alloy does not have a significant change in the stress required at the onset of reorientation, which is here obvious in a very small-slope increase of the stress (rather than a true plateau as in NiTi) from approximately 0.75 to 2% engineering tension strain. The key difference in the mechanical behaviors of the two alloys can instead be seen in the overall strengthening amounts per unit strain: in NiTiPdTa, the stress exceeds 750 MPa before its fracture will occur at approximately 6% engineering strain, while in NiTi such stresses are not seen until approximately 30% strain, which is well into the late plastic deformation region.

NiTiPdTa appears to show deformation between 2 and 6% strain which mimics the behavior observed in the ‘region III’ reorientation deformation in NiTi, which seems to indicate that at the point of fracture the primary mode of deformation in NiTiPdTa is still reorientation of martensitic variants and detwinning behaviors, rather than slip – somewhat boldly, it could be argued from this stress-strain behavior that the onset of slip is the initiation point for fracture in this material, a claim which is not contradicted by a strongly brittle fracture surface seen on these samples after failure. Again using NiTi as a reference, it would appear that due to the dominance of reorientation and detwinning mechanisms at the point of failure NiTiPdTa will still be undergoing an increase in negative CTE and will not yet reach a point of inflection as seen in NiTi above 9% strain.

5.3 Tensile Thermal Expansion Evolution in NiTiPdTa

Figures 5.5(a) and (b) illustrate the overall thermal expansion response as a function of tension prestrain in NiTiPdTa.

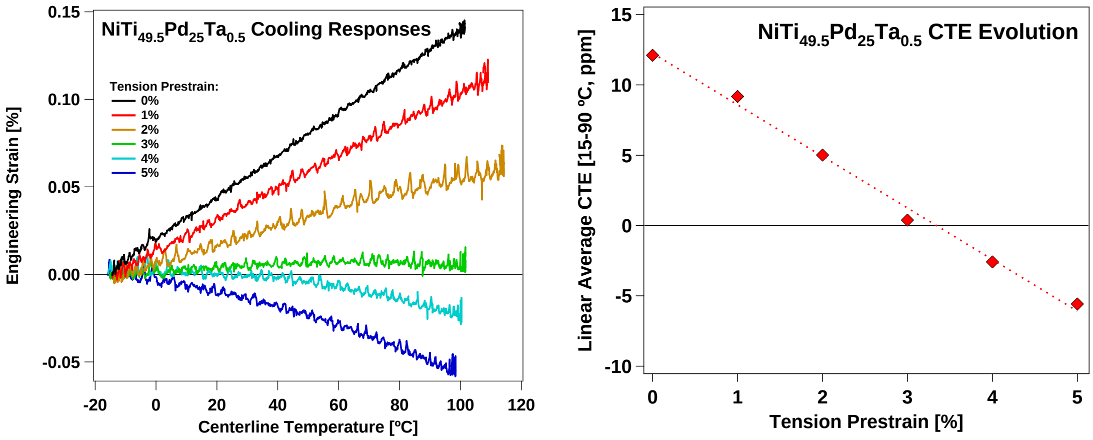

(a) (b)

Figure 5.5 Thermal Expansion Response of NiTiPdTa. (a) Strain-temperature response during cooling from the maximum heated temperature at each prestrain level. (b) Linear average thermal expansion measured in a 75 °C window as a function of sample prestrain.

When examining the strain verses temperature curves for 1-5% prestrain in 5.5(a), it can be observed that there is a degree of nonlinearity in the thermal expansion response over the whole temperature range being measured. More intriguingly the apparent inflection point into the low-temperature linear curve is not constant between these prestrains and appears to be reducing as the applied tension prestrain increases. The most likely explanation for this observed behavior is the increasing alignment of the [010] orientation into the tension direction, as it can be observed that the CTE magnitude increases in the (020) plane through the entire temperature range studied in tension. The reduction in randomly oriented variants most probably removes any countervailing effects and allows for the [010] crystalline nonlinearity to manifest at lower temperatures as its population fraction per unit area in the normal plane increases. Beyond this, the CTE does appear to decrease with increasing prestrain until fracture as expected.

Figure 5.5(b) shows that the overall evolution of CTE in NiTiPdTa is much slower than in NiTi, reaching a maximum average linear thermal expansion in a 75 °C window of only -6 ppm. Even when accounting for the slightly higher starting thermal expansion of the undeformed sample, this means the overall utilization of the potential negative CTE in NiTiPdTa is approximately 49%, against the 82% of NiTi when taking the maximum available crystalline NTE into account. Likely this is due to the premature ending of the reorientation/detwinning processes as a result of the low rupture strain. The CTE evolution was largely linear, similarly to NiTi through the Region III deformation process; it is likely that were slip to begin at 6% strain as postulated, then the CTE change would begin to level off in a similar manner; this indicates that not a large fraction of the remaining NTE would have been accessible regardless. This lower overall availability of the maximum anisotropy would be consistent with the higher bond strength and reorientation/detwinning stresses seen in NiTiPdTa as compared to NiTi.

5.4 Stiffness Response to Deformation

Figure 5.6(a) shows the change in the elastic stress-strain curve as a function of temperature for the 5% prestrain case in NiTiPdTa. It can firstly be noted that at such high input stresses there is a non-negligible elastic hysteresis as a result of various responses in the material to stress input. As such 500 MPa (which can only be reached in the 4 and 5% prestrain cases, regardless) are not used for analysis purposes, but they provide an illustration on the magnitude of the overall elastic modulus change due to temperature in this material. Here it can be observed that with a common origin on the loading curve (left side), the overall deflection as temperature increases is extremely small over the course of the nearly 120 °C temperature change; qualitatively, it can be seen that the overall change in the peak strain at this maximum stress is less than 2 hundredths of a percent.

When examining the relatively linear portion of the curves seen in 5.6(a), it can be observed that it persists to above 100 MPa. Thus, the examinations up to 100 MPa used for the analysis and illustrated in Figure 5.6(b) should be valid, and indeed it can be seen that in this case the elastic hysteresis, while not eliminated entirely, is sufficiently small as to allow for quantification of the linear average elastic modulus. Similarly, to the higher-stress case, it can again be observed that the overall change in the strain with temperature is extremely small in this 5% prestrain case.

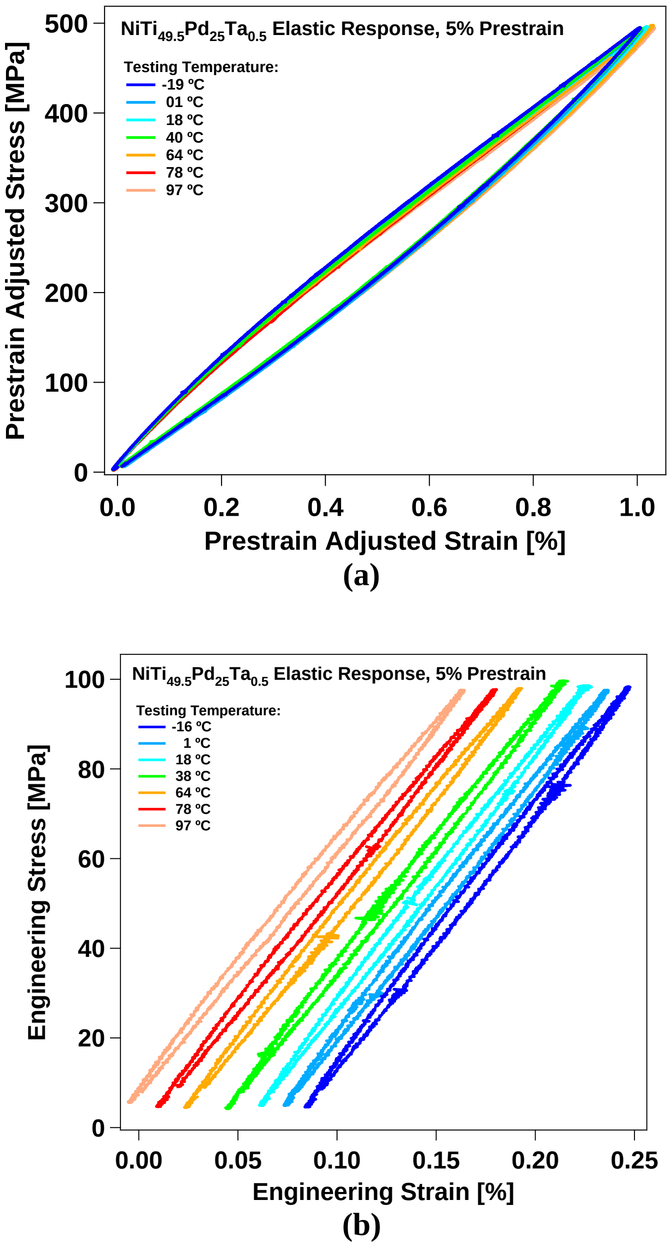

Figure 5.6 Illustration of the thermal elastic cycle response in NiTiPdTa at 5% tension prestrain. (a) Adjusted stress-strain response during loading and unloading with a 500 MPa loaded stress target, with common start point to illustrate direction of change in overall elastic response with temperature. (b) Detail to 100 MPa maximum, showing the response considered for comparison between deformation levels.

The effect of tension prestrain on the elastic modulus and the elastic modulus as a function of temperature can be seen in Figure 5.7(a). When examining the elastic modulus at a given temperature across all prestrains, it can be seen that there is something of a ‘v’ effect: the modulus appears to initially decrease in the first 2% of applied prestrain, before gradually increasing over subsequent prestrain steps. How much the modulus changes between prestrain amounts appears to be dependent on the modulus-temperature slope for that prestrain. As an example, in the case of 4 and 5% prestrain which present with what appear to be similar elastic modulus-temperature rates of change, the y-axis offset between the two sets of data appears to be constant.

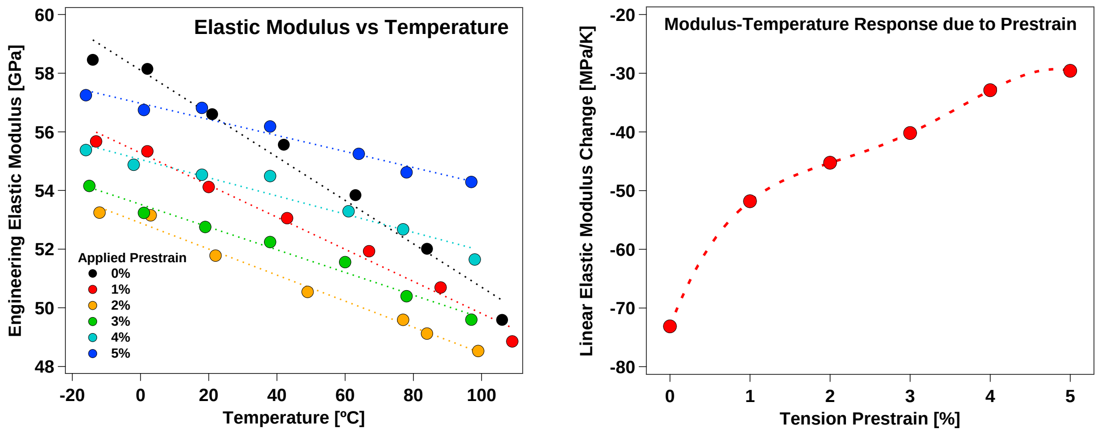

(a) **(b)**

Figure 5.7 Examination of NiTiPdTa elastic response to temperature. (a) Engineering elastic modulus measured as an average of the loading and unloading steps in the cycles illustrated in Figure A-5(b) compared as a function of temperature and prestrain. (b) Evolution of the overall average slope of the elastic modulus due to temperature, charted as a function of applied prestrain.

The change in the elastic modulus as a function of temperature does appear to decrease quite radically in these first few percent of tension prestrain, which is confirmed in Figure 5.7(b) where these average rates of change are plotted as a function of the applied prestrain. The largest change occurs between undeformed and 1% prestrain. Relative to NiTi NiTiPd appears to be less responsive to temperature at base, and at 1% prestrain is already matching the rate of change observed in NiTi after having entered the plastic region of its deformation curve. The ultimate value of the elastic modulus-temperature slope line in NiTiPdTa, -30 $MPaK^{-1}$, is significantly less than the most stable value observed in NiTi material.

Relative to NiTi, it appears the main cause for the significantly improved elastic modulus-temperature response is mainly because to the nature of the bonding experienced in the metal due to the high-strength PdTi bond. Considering that such low temperature effect on elastic modulus was achieved at only 6% prestrain, and before the onset of plastic slip, it leads to a logical question as to what performance may be possible should methods for achieving higher maximum strains in similar NiTiPd derivates, such as NiTiPdCu, be attempted. Alternatively, should a method for subjecting PdTi to significant deformation be determined, it may be informative to examine its own inherent thermal expansion and elastic modulus properties in this context.

5.5 Summary and Conclusions

In this chapter the effect of the substitutional Pd alloying on NiTi alloy was examined by repeating the key tests performed on NiTi alloy in Chapter IV. The following results were observed in this process:

1. Addition of sufficient Pd creates a phase shift, which caused a change of the primary axis of NTE to the orthonormal [010] direction of the orthogonal martensite. At the 25 at% addition, the net effect on the maximum operational temperature is +50 °C.
2. The net anisotropy in the NTE direction is significantly reduced relative to the monoclinic, equiatomic NiTi, with room-temperature NTE of -12.2 ppm.
3. $NiTiPd_{25}$ is limited by its low fracture strain (~6%) rather than its ability to reorient, and the thermal expansion had not plateaued at end of deformation.
4. $NiTiPd_{25}$ demonstrated significant reduction to -30 MPa/K of its elastic modulus change as a function of temperature, which was again limited by low fracture strain. Unlike in NiTi, the reductions are solely due to reorientation/detwinning effects within the strain range which was achievable.
5. Many of the changes in NiTiPd relative to NiTi appear to be caused by the introduction of the stronger PdTi pseudo-intermetallic. Use of other NiTiPdX alloys with higher deformation strain limits or PdTi alloy may prove fruitful towards both characterizing and maximizing the properties improved by the addition of Pd into the material.

CHAPTER VI

INVESTIGATION OF ANISOTROPIC CRYSTALLINE AND BULK NEGATIVE THERMAL EXPANSION IN BETA-TITANIUM ALLOYS

Tailoring thermal expansion in alloys in common engineering alloys has traditionally been difficult. Most alloy groups will possess a small range of positive coefficient of thermal expansion (CTE) for an allowable chemical range [1]. Workarounds exist in limited number of specific materials and structures which display negative CTE where the system will instead shrink when heated. However, until recently, most of these negative CTE materials have been non-metallic compounds or required creating compliant structures where negative CTE is created by differential bending of positive CTE structures [1, 51]. A new subclass of shape memory metal alloys exhibit crystallographic CTE anisotropy at the lattice level [15, 16, 39, 46, 52-54], and it has been demonstrated that this anisotropy can be exploited in polycrystals through crystallographic texturing upon deformation processing [15, 16]. This yields a tailorable bulk CTE with simultaneous positive and negative CTE directions allowing for observation of bulk CTE between -40 ppmK^{-1} and +50 ppmK^{-1} [15, 53] with typically two large magnitudes of CTE demonstrating opposite signs.

Common to all known instances of this behavior is possession of a thermoelastic martensitic transformation between a higher-symmetry austenitic and a lower-symmetry martensite - the phase that demonstrates an anisotropic CTE tensor. The most useful of these martensitic materials are shape memory alloys (SMAs) such as NiTi, NiTiPd, CoNiGa, NiMnGa, and TiNb [15, 54]. The anisotropy occurs in fully martensitic materials well below the temperatures where transformation would occur, which raises questions as to what exactly the underlying cause for this behavior is. Naturally, the physics of anisotropic CTE in martensitic materials is not fully understood; however, the comparison of the lattice parameter differences between phases can predict much of the anisotropy behavior. A thermal excitation mechanism similar to that of phenomenological models of Invar alloy [2, 4, 30] has been proposed to give a rough explanation of this behavior [15]. If the lattice spacing along a given vector in martensite is longer than an equivalent lattice parameter would be for the austenite at a given temperature, then martensite in these alloys is observed to contract during heating. Similarly, in the reverse case a shorter martensite than its equivalent austenite is also often seen showing a rapid expansion.

Use of thermomechanical processing in polycrystals allows for controlled changes in crystallographic texture and through this exploitation of the lattice CTE anisotropy in bulk samples. Martensite can easily be textured through variant reorientation/detwinning under low applied strain levels, often with little or no accompanying conventional plasticity [55-57]. In our first report on this phenomenon, tensile deformation of a polycrystalline NiTiPd SMA allowed sufficient reorientation for thermal expansion to change from + 14 ppm K^{-1} to – 3 ppm K^{-1} after only 5% tensile deformation was applied [15]. In disordered martensite such as those in binary TiNb SMAs [45, 58] simple deformation processing such as rolling or wire drawing can produce significant crystallographic texturing with accompanying large CTE anisotropy. TiNb alloys can easily be deformed at room temperature to tensile strains over 35% [53] or thickness reductions exceeding 90%, allowing deformation to be applied across a very broad range.

In our previous work (Chapter II) rolling of $Ti_{78}Nb_{22}$ resulted in bulk CTE ranges from -40 to +50 ppm K^{-1} [15, 53, 54] which should allow for the creation of very effective high-temperature anisotropically varying (anvar) alloys. However, both specific key information being missing and some problems with rolling was discovered in the process of this initial survey as well as a further investigation.

The information acquired in X-ray diffraction established the role of composition on CTE but required revisiting. Copper k-alpha x-rays were only capable of surface penetration of samples, meaning they were affected by oxidation of the titanium-based metal as it was heated to any significant temperature. While the high-temperature crystalline CTE information was useful, CTE applications exist both for high and low temperatures and further information regarding an apparent nonlinearity of the strain vs temperature below room temperature was considered desirable. Further investigation especially was desired as to whether there was a minimum temperature at which anisotropy stopped, which would indicate when the thermal barrier for excitation would become too large [15, 59].

Rolling is a powerful tool for applying large deformation amounts quickly but use of it systemically to characterize anvar alloy response is complicated by the aforementioned ease of detwinning reorientation. In our previous work it can be seen how rapidly the thermal expansion evolved when comparing 0 and 20% thickness reduction, which is in large part caused by the initial reorientation response in the first few percent of applied strain. Further investigation into low amounts of rolling showed large inconsistency in application due to this initial deformation sensitivity and made comparing different compositions and rolling techniques difficult, especially when targeting small changes in CTE from undeformed material. Resultantly, a more precise method that ideally would also allow for multiple deformation inputs on the same sample would prefer.

Similarly, while a strong inferred connection between bulk and crystalline CTE via texture was shown in the previous study by showing each of the three elements separately, no attempt to show a direct link between them was shown previously. In order to address these questions, TiNb was subjected to synchrotron measurements with liquid nitrogen access to better scrutinize its crystalline CTE, an in-situ tension deformation method was devised to allow for examination of stepwise deformation on the same sample with much finer deformation control, and measurement of texture in synchrotron would allow for comparison of crystalline CTE with texture to verify whether it would be able to predict macroscopic CTE behavior.

6.1 Crystalline Thermal Expansion: Effect of Deformation

Figure 6.1 demonstrates the two-theta plots as a function of temperature resulting from integration of the output for a $TiNb_{22}$ micro-tension dogleg which has been loaded to 4% prestrain before mounting in synchrotron. For this illustration, this shown through 7 of the points measured during cooling from the heating step. In Figure 6.1(a), the temperature range observed in this experiment demonstrates little to no apparent beta-phase present in the sample either from sample preparation or thermal transformation.

Generally, there is some increase in peak intensity as temperature increases up to about room temperature (likely due some frost formation), although it is only significant in a few cases such as (111) below room temperature.

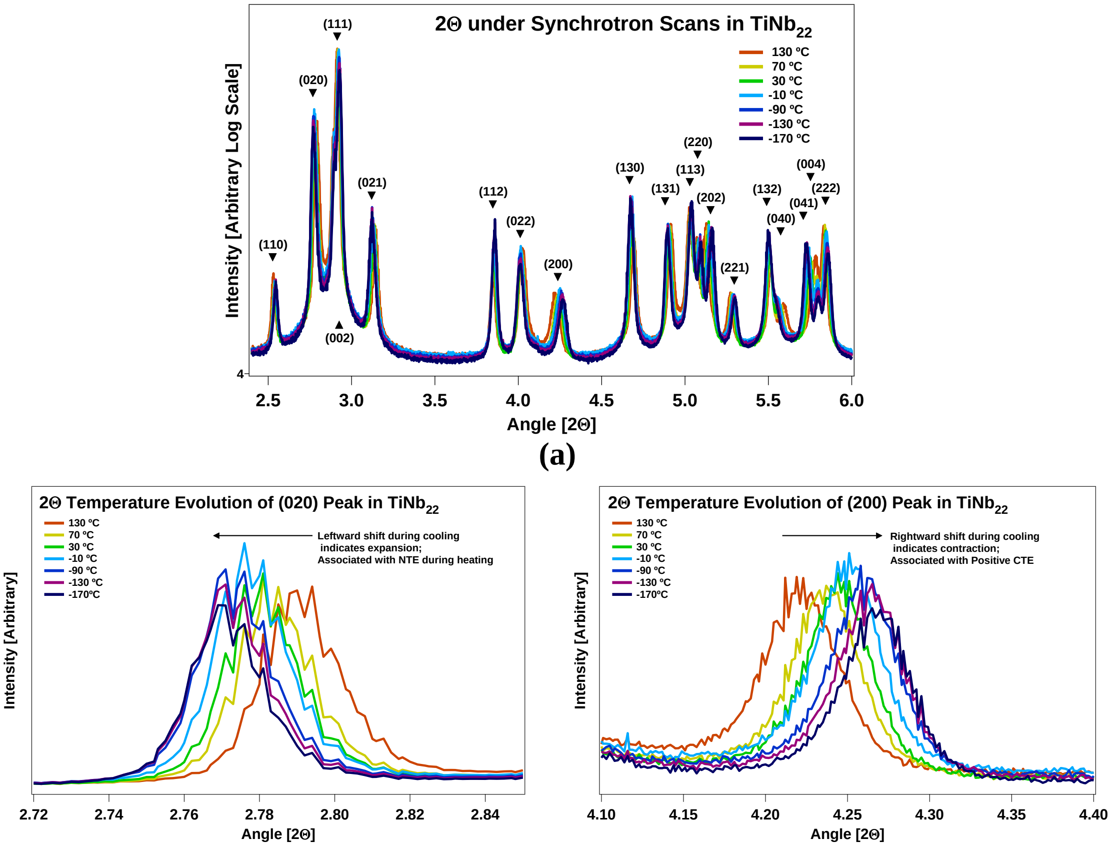

(a)

(b) **(c)**

Figure 6.1 Integrated synchrotron output of a $TiNb_{22}$ alloy. (a) typical two-theta of $TiNb_{22}$ alloy with integrated results of seven temperatures with even intervals. (b) Detail of the (020) HKL peak with the same temperature interval. (c) Detail of the (200) peak with the same temperature interval.

Two of the most interesting crystalline directions in the martensite are the ones associated with the (020) and (200) crystal peaks. The crystalline strain in the [010] direction is illustrated via the (020) peak in XRD in Figure 6.1(b). In both, the process of cooling from 130 °C to -170 °C is illustrated in seven steps. When examining the (020) peak shift, it can be observed that the center of the (020) peak is clearly moving left through the entire temperature range. This indicates an expansion of the lattice during cooling, which is a negative thermal expansion moment. This rate of contraction is significant at high temperatures, but it can be observed to be a smaller degree of shift as the temperature decreases. This same behavior can be seen in the (200) peak, but in this case the indicated behavior shown by the peak shift being towards the right during cooling is a large degree of contraction.

In addition to the (020) and (200) peaks, a summary of the strain change for the strongest peaks found in $TiNb_{22}$ can be found illustrated in Figure 6.2. Here four different prestrains can be compared to see how their anisotropy differs: undeformed, 4%, 7%, and 20% prestrain. Two major themes can be observed from this set of deformation levels: firstly, that the anisotropy appears to roughly have the same configuration and proportions and differs mainly in its overall magnitude (e.g., when the negative thermal expansion in the (020) is larger, generally so is the positive thermal expansion in the other orthonormal directions). A few rules consistently hold: the (200) expansion rate will always be larger in magnitude than the (020) contraction, and combined with the (002) peak’s expansion, this implies that a positive volume expansion is retained in martensite. The second significant characteristic is a temperature dependency regarding the magnitude of the thermal expansion in the crystal: at low temperatures, there is a small strain change per unit change in temperature, while at higher temperatures there is a significantly larger and accelerating rate of strain change.

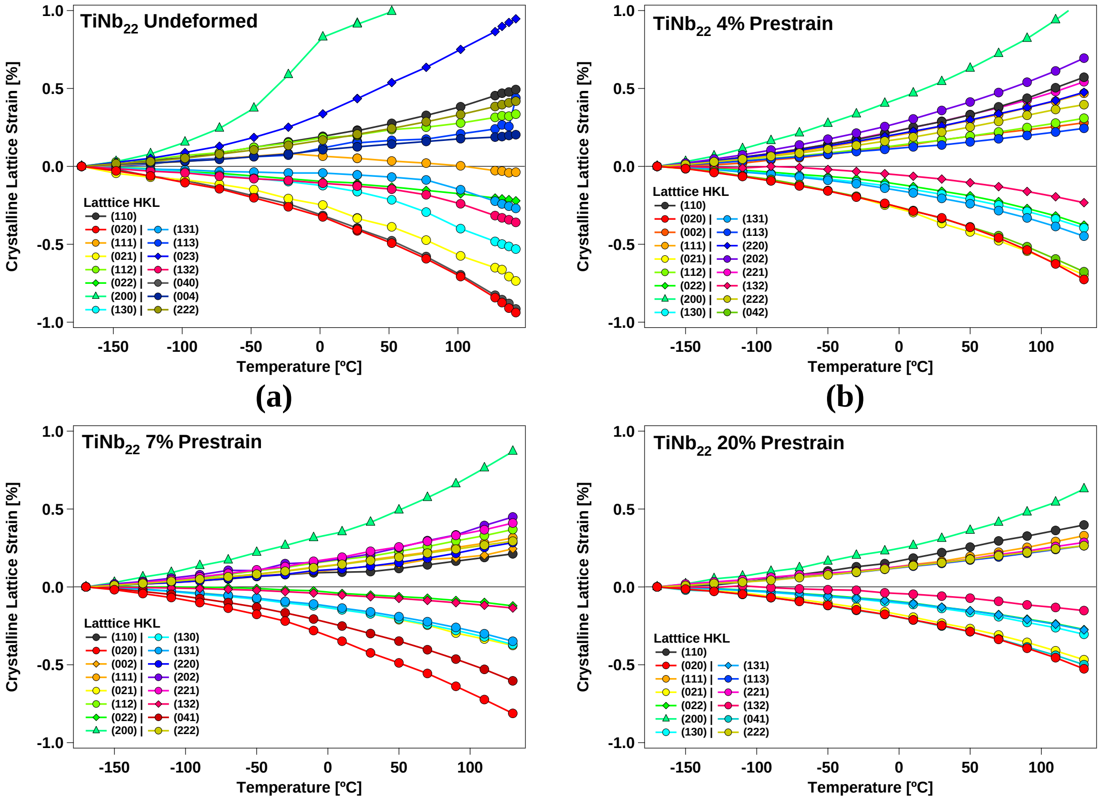

(a) (b)

(c) (d)

Figure 6.2 Crystalline strain vs temperature for 4 deformation prestrain levels of TiNb$_{22}$ alloy as determined by synchrotron measurements. (a) undeformed, (b) 4% Prestrain, (c) 7% Prestrain, (d) 20% Prestrain.

This temperature dependence is more completely explored via CTEAS [60] analysis of the 4% prestrain case in Figure 6.3. Here the effect of this temperature dependence becomes more starkly clear. In nearly all cases the c-axis [001] (z-axis) direction shows a small expansion near to 4 ppm K^{-1} which is nearly constant. In complete contrast is the a [100] and b [010] axes (x and y directions in the figures respectively), which start at minimum temperature with similar or even smaller magnitudes of strain change, but rapidly increase throughout the temperature range. This leads to a visible change in the shape of the anisotropy not obvious in the strain change graphs in Figure 6.2. While at higher temperatures there evolves a clear preponderance in ordering of the anisotropy such that angles near that of the a-axis consistently output large expansion and angles near that of the b-axis will display large contraction, at low temperatures the entire a-c plane shows a nearly homogenous expansion, and only a small contraction remains in a small region centered around the b-axis.

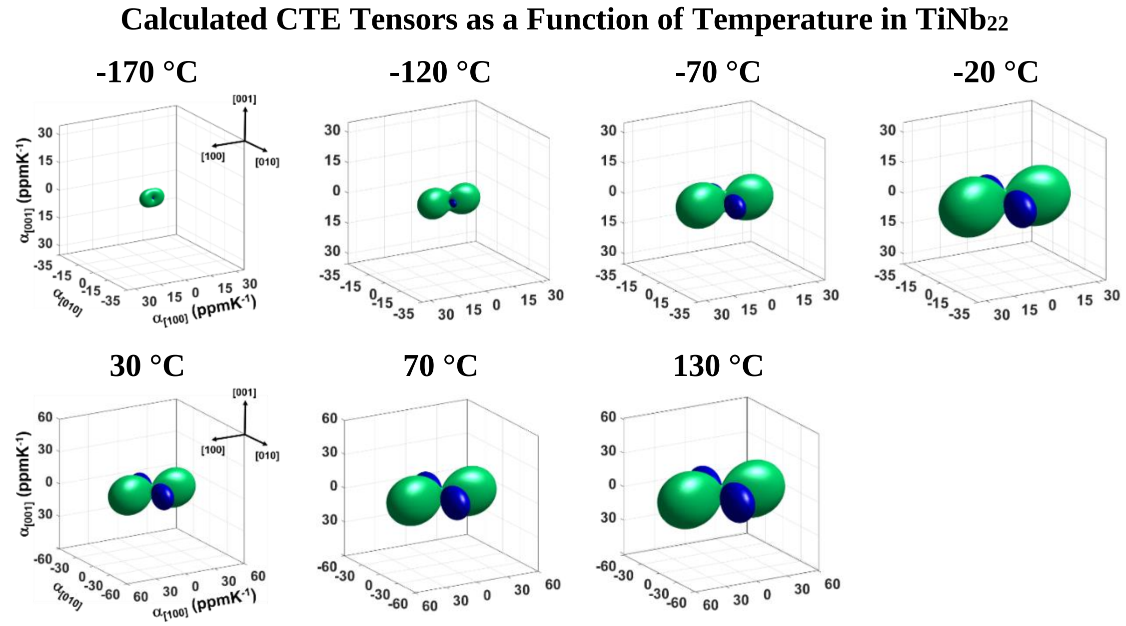

Figure 6.3 CTEAS Plotted Thermal Expansion Tensors for TiNb$_{22}$. 4% Prestrain at various temperatures, temperature spacing identical to Figure 6.1, beginning at top left (-170 °C), and progressing left-to-right to bottom right (130 °C).

This change from the near-homogeneity into the strong anisotropy occurs rapidly, as the a-axis grows from an effective CTE of 6 to 15 ppmK^{-1} over 50 degrees C, and then to 20 ppmK^{-1} after 50 more degrees have passed to -70 °C. By room temperature, this has increased to 40 ppmK^{-1} and eventually reaches 60 ppmK^{-1} at the final high temperature of 130 °C in this examination. This is mirrored in the b-axis, which likewise demonstrates the same increase in magnitude of contraction, starting at just -2 ppmK^{-1} before eventually growing to approach -50 ppmK^{-1} in the range examined here. In contrast to the apparent picture painted in Figure 6.2, there is significant changes occurring over the temperature range in this case.

6.2 Crystalline Thermal Expansion: Effect of Composition

Similar to the deformation case above, the composition of TiNb has a noticeable effect on the thermal expansion anisotropy seen in the alloy when examined at the crystalline level, as has been noted previously. To further examine this relationship, the lattice strain change as a function of temperature is examined in Figure 6.4 for the compositions of $TiNb_{15}$, $TiNb_{20}$, $TiNb_{22}$, and $TiNb_{24}$ when cooled to below -150 °C.

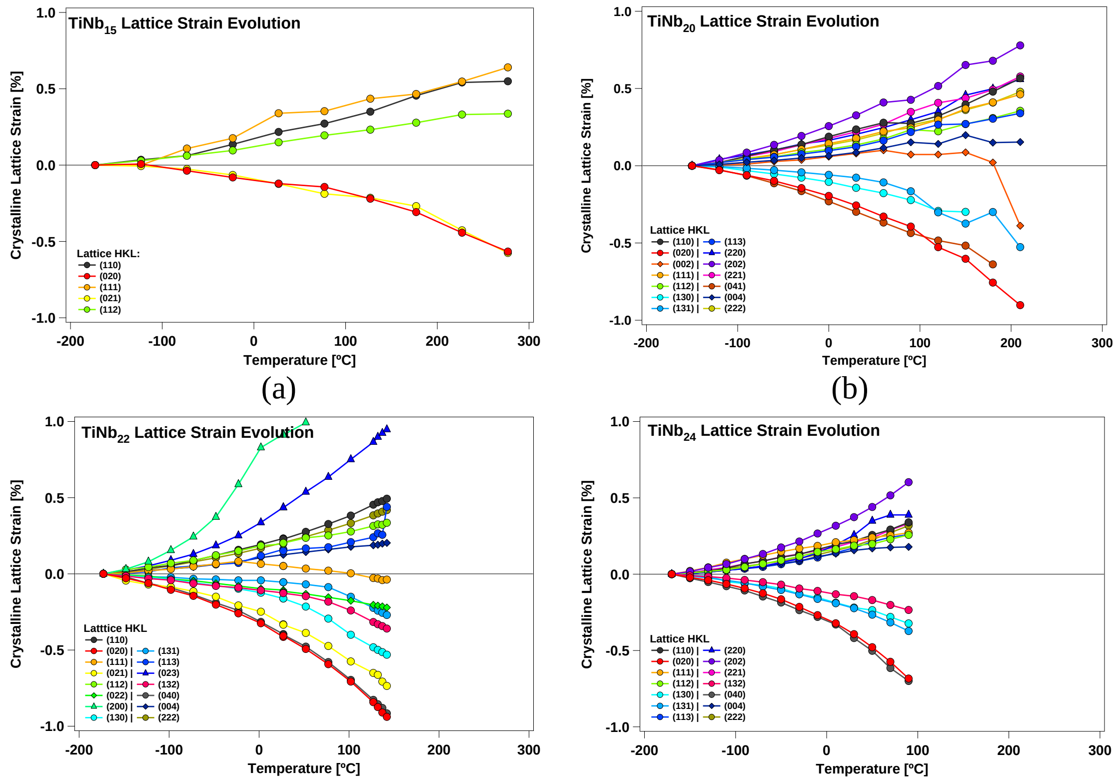

(a) (b)

(c) (d)

Figure 6.4 Strain vs temperature for four compositions of TiNb alloy. Clockwise from top left: (a) $TiNb_{15}$ (at%), (b) $TiNb_{20}$, (c) $TiNb_{22}$, (d) $TiNb_{24}$

Here a few key items may be noted. Firstly, as has been observed previously, all compositions examined demonstrate thermal expansion anisotropy throughout their entire temperature range. This statement is most significant for $TiNb_{15}$, which demonstrates particularly small strain change rates at low temperatures and has the slowest rate of growth as temperature increases. Despite these handicaps, it does demonstrate negative thermal expansion in the (020) peak even at minimum temperature, and can come to show rather significant CTE anisotropy magnitude as it comes to approach 300 °C.

Compared to $TiNb_{15}$, all of the other compositions which contain 20% or more niobium demonstrate significantly greater thermal expansion anisotropy. $TiNb_{22}$ does appear to have an obviously greater CTE magnitude relative to $TiNb_{20}$ (at expense of a lower maximum temperature), but $TiNb_{24}$'s significantly lessened maximum temperature makes its overall note thermal expansion magnitude harder to clearly identify as greater. However, it can be noted that the total amount of strain achieved in the (020) peak at a given temperature (e.g., 30 °C) is in fact highest for $TiNb_{24}$, followed by $TiNb_{22}$ and then $TiNb_{20}$. Since overall CTE anisotropy magnitude in other directions appears to be proportional to the CTE magnitude of any one direction, it follows that the CTE magnitude of anisotropy is highest for $TiNb_{24}$ in all directions.

6.3 Tension response of thermal expansion

A single cycle within the in-situ deformation process is illustrated more completely in Figure 6.5. Here, a separate tension sample separate from this study was deformed from 8% to 12% engineering strain in one step. To achieve this, the engineering force is increased until reaching the maximum deformation strain, whereupon it is unloaded in a linear fashion. For the remainder of the cycle (the temperature step), the force is held constant. Figure 6.5 shows the change in the sample centerline temperature rather than the grip temperatures through the cycle. While nominally isothermal during the deformation step, some variance in temperature can occur as the deformation occurs. This is followed by the temperature ramps. It can be noted that despite the nominal 120 and -20 °C upper and lower cycle limits, the centerline reaches only to 110 and -10 °C in the process. However, during the temperature ramps the change in centerline temperature is approximately linear and it is only during the initial changes in temperature and isothermal steps that the changes in centerline temperature are nonlinear.

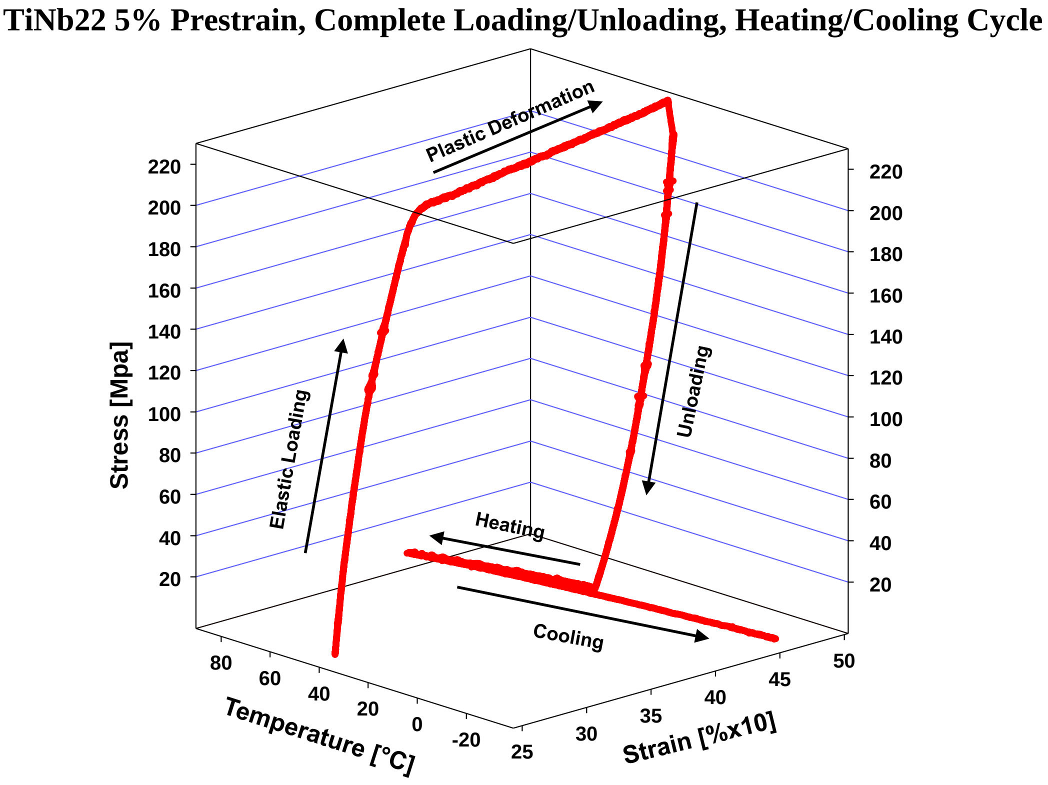

Figure 6.5 Illustration of the temperature-strain-stress relationship in a single iterated deformation step. 1) Load at constant displacement rate to target strain 2) unload at constant force rate to standby load 3) heat sample to cycle maximum temperature 4) cool sample to cycle minimum temperature. Not shown is 5) reheat sample to room temperature.

Figures 6.5 demonstrates the common cyclical output during the deformation and temperature steps. Figure 6.5 shows the stress-strain output of a single cycle, which predictably is dominated by the deformation step. Due to the isostress nature of the temperature step, the strain changes which result from the heating and cooling stage is expressed as the flat line centered around the end of the unloading point in the bottom right of the figure. In figure 6.5, the change in strain as a function of temperature is illustrated. Here again there is a large change in strain during the isothermal deformation step, but in this case the relative strain changes during the temperature stage are easily visible in contrast to this, with the change in strain per unit temperature (CTE) visible in this graph as the sample undergoes heating and cooling.

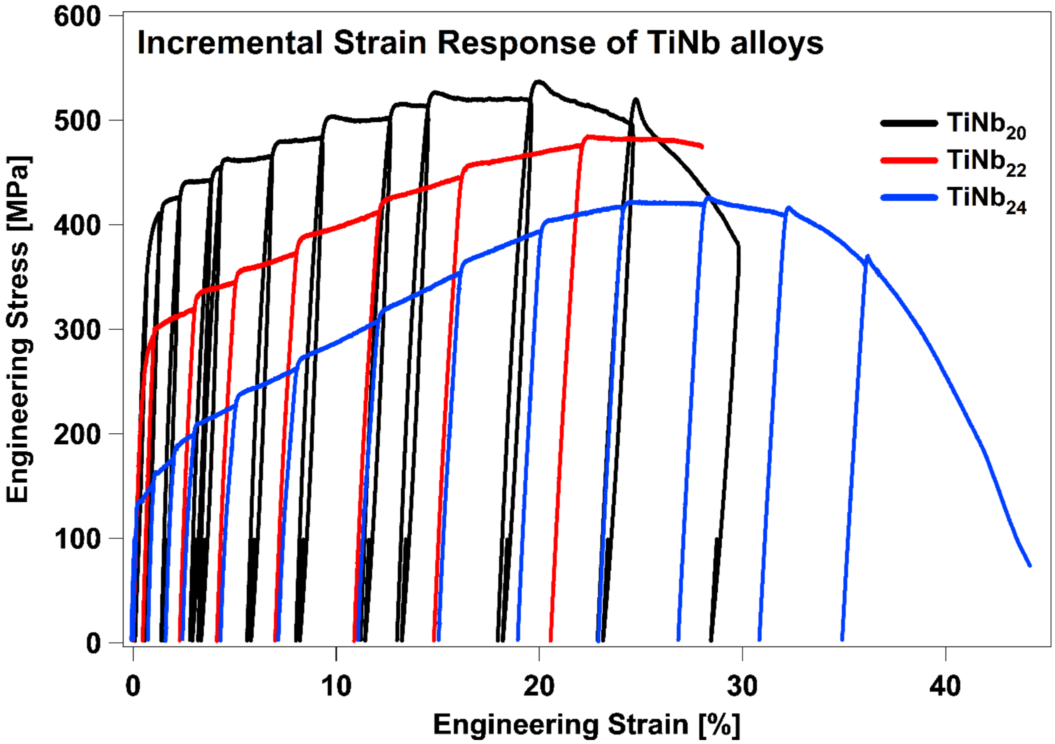

Figure 6.6: Illustrative stress-strain responses for the iterated tension deformation during the in-situ tension test process. $TiNb_{22}$ was terminated at onset of necking instead of being allowed to continue as in the other cases.

Figure 6.6 shows the deformation pathways (all of the deformation steps) superimposed upon each other, for $TiNb_{20}$, $TiNb_{22}$, and $TiNb_{24}$. Despite the segmented nature of the deformation and interposed heat/cool cycles and associated risk of omega-phase precipitate formation, the chained deformation steps generally conform to the shape of monotonically tested samples of this same material as previously reported for $TiNb_{22}$ and is also true of $TiNb_{24}$. However there is a distinct difference in behavior relative to the continuous deformation curves most visible in $TiNb_{20}$ where instead of a continuous smooth strain hardening curve the sample instead manifests a series of individual stress plateaus after some initial slightly higher yield stress to initiate deformation for that particular step. This is probably tied in some part to the small amounts of incremental deformation in each step, as it can be seen in some of the larger individual deformation steps that strain hardening once again can be seen towards the end of a given plateau. This is probably tied to a low overall amount of variant reorientation in this composition, paired with a smaller strain hardening coefficient, as reported in a prior examination on TiNb alloy.

The individual cooling steps for each deformation level of an *in-situ* test as a function of the *engineering strain* in each composition is shown in Figure 6.7. Only the first 2% of strain application is shown in $TiNb_{15}$ (Figure 6.7(a)) due to voids in the sample causing premature failure in subsequent cycles and owing to its visible lack of any deformation response leading to CTE change. The overall average strain before failure is generally low in addition as previously reported, leaving little room for any additional change in the behavior of the sample.

Cooling CTE Evolution after each Target Prestrain is Applied

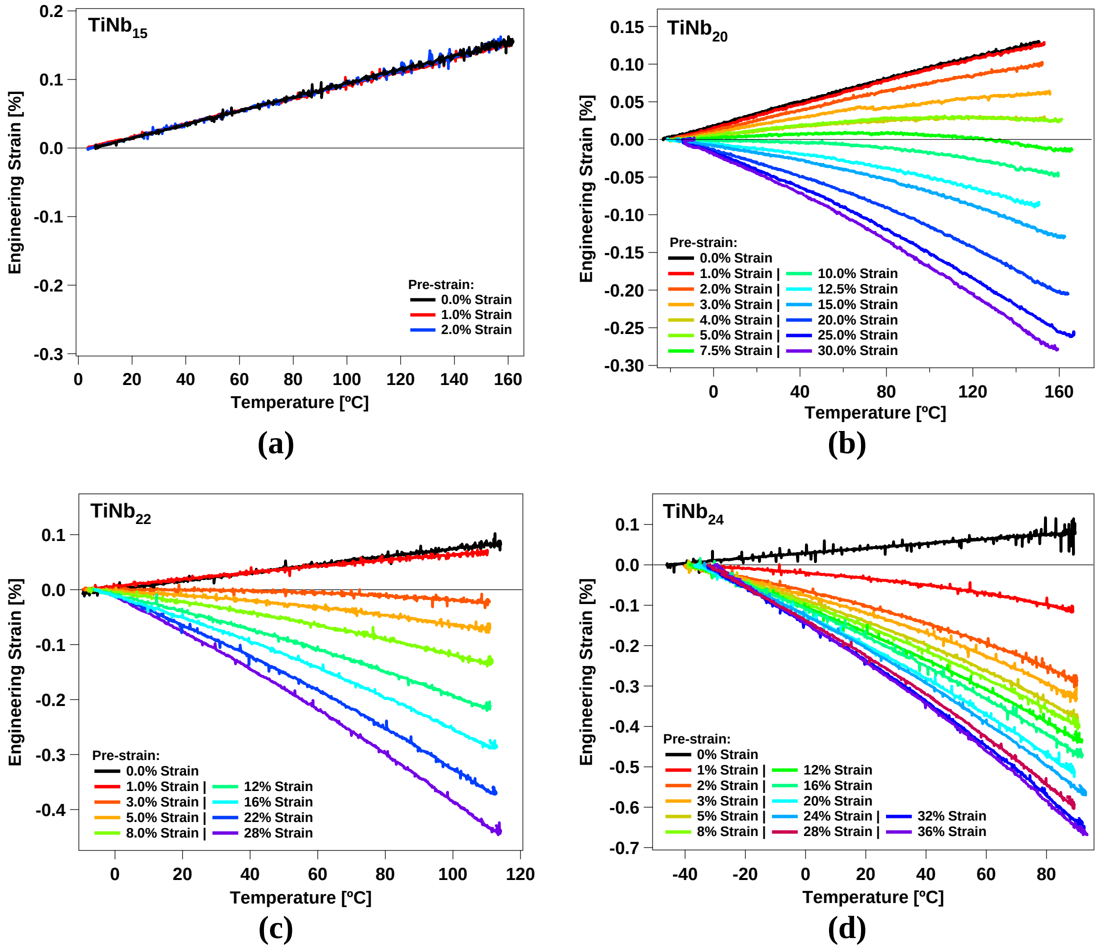

(a) (b) (c) (d)

Figure 6.7 Strain vs temperature of tension samples at various levels of deformation via prestrain. Clockwise from top left: (a) $TiNb_{15}$, (b) $TiNb_{20}$, (c) $TiNb_{22}$, and (d) $TiNb_{24}$.

Contrasting with $TiNb_{15}$, $TiNb_{20}$, $TiNb_{22}$, and $TiNb_{24}$ all show rapid evolution of the axial direction thermal expansion over the first few percent of deformation, with all demonstrating some degree of negative thermal expansion within the first 5% of prestrain and $TiNb_{24}$ demonstrating completely negative CTE seemingly immediately upon any plastic strain being input at all. $TiNb_{20}$ by contrast requires reaching 7.5% prestrain before demonstrating fully negative thermal expansion throughout the range, with a notable nonlinearity of slope that results in a sign change of the CTE during the temperature ramp in 4% up through 10% prestrain curves. This nonlinearity is most clearly retained in $TiNb_{20}$, which demonstrates it in nearly every strain level, but is not exclusive to this composition and appears in some middle-prestrain curves of $TiNb_{22}$ and early prestrain curves of $TiNb_{24}$.

When comparing the stress-strain curves in Figure 6.6 with the strain evolutions in Figure 6.7, there is a clear correlation between initial yield stress and ‘swiftness’ of CTE evolution. Note that in $TiNb_{24}$’s deformation curves in Figure 6.6, the yield stress is quite low and strain hardening occurs very rapidly, likely indicating a high ease of variant reorientation in the material. This contrasts strongly with the more than doubled yield stress of $TiNb_{20}$, which implies a higher threshold for initiation of variant reorientation. This trend extends beyond both to the yield stress of $TiNb_{15}$, which as reported in prior work is higher still, and appears to output no significant favorable variant reorientation at all.

Of some interest is the apparent contrast in line shape for the strain vs temperature curves of bulk tension samples against the crystalline strain shown in Figures 6.2 and 6.4. Compared to the crystalline strain, there is much less nonlinearity in the CTE response, even where that would be significant for the crystalline samples. While there is some, which increases as deformation does, it has a small overall effect in the temperature ranges studied in tension. This may be a result of tension generally being carried out in more linear regions of the strain response in crystals, or be indicative of polycrystalline phenomena (grain boundaries, dislocations, misorientations) which impart effects not reflected in the crystalline response.

6.4 Discussion

6.4.1 Lattice changes due to deformation

The calculated ‘a’ and ‘b’ lattice parameters for TiNb with different deformation levels is shown in Figure 6.8. Figures 6.8(a) and (b) show the lattice parameters for $TiNb_{22}$ and Figures 8c and d show the change for $TiNb_{24}$. It should be noted that previous literature has already established the shift in lattice parameters as a function of temperature – the ‘a’ axis grows rapidly while the ‘b’ axis shrinks as Nb content increases.

That this holds true can be examined best as a comparison beginning at 4% prestrain and then increasing the prestrain from this point, rather than from 0% prestrain. This appears to indicate some initial lack of effect resulting in larger changes in the 4% case.

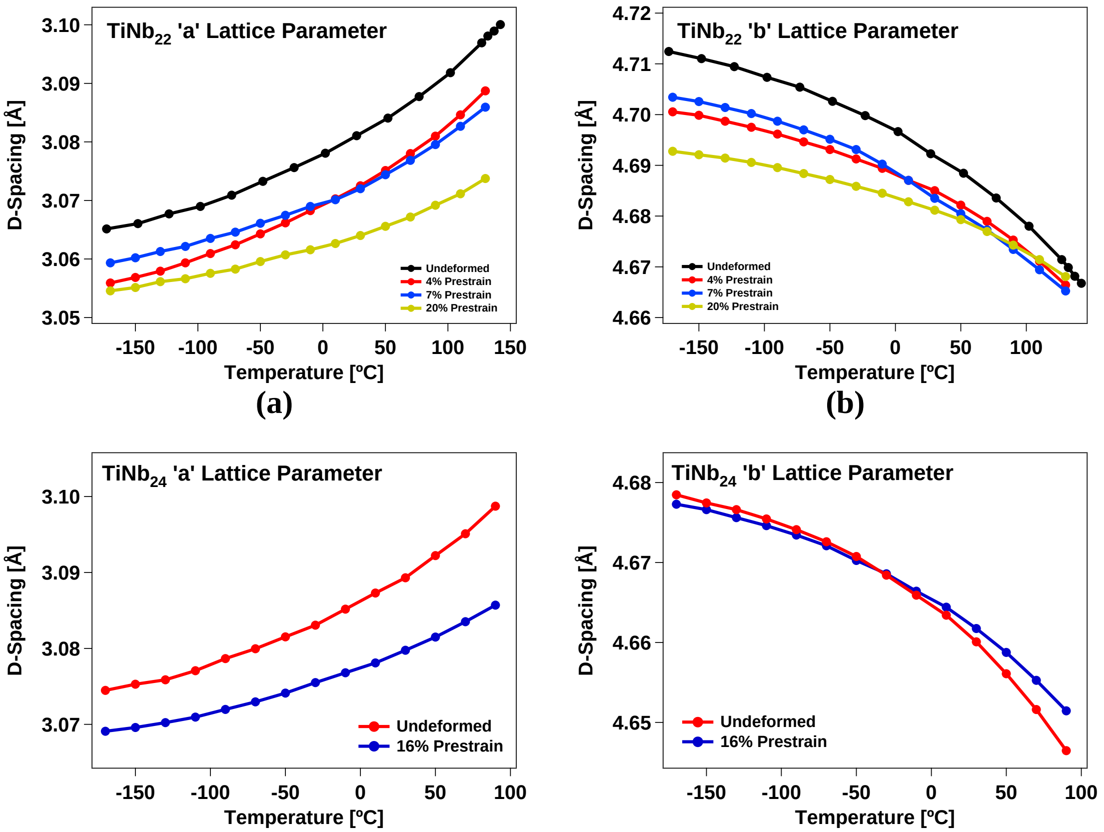

(a) (b) (c) (d)

Figure 6.8: Calculated lattice parameters for the a and b orthonormal axes. Clockwise from top left: (a), (b) TiNb$_{22}$ 'a' and 'b' lattice parameters for 0, 4, 7, and 20% applied prestrain; (c), (d) TiNb$_{24}$ 'a' and 'b' lattice parameters for 0 and 16% applied prestrain.

In both compositions it can be observed that the lattice parameters are being generally decreased as the deformation applied increases – this was also observed in the ‘c’ axis. This does not always hold true as Figure 8d with minimal shift in starting LP distance demonstrates, but the axis least likely to show such compression is the ‘b’ axis, which does make sense in the context of it being most aligned with the tensile force. In both the ‘a’ and ‘b’ axis the magnitude of the CTE can be observed as decreasing as the LP shift occurs during deformation.

Figures 6.8(a) and 6.8(c) show this trend in the ‘a’ axis, where in both $TiNb_{22}$ and $TiNb_{24}$ the lattice parameter is observed to decrease with deformation. In this same situation it becomes evident that the change in the LP as a function in temperature is also changing as a response to deformation, resulting in a net increase in the difference between LP as temperature increases when compared against undeformed material. Similar trends can be seen in 8b and 8d where the LP will decrease, only in the case of NTE often the reduction in CTE is expressed as a smaller difference between LP as temperature increases for different deformation conditions. This indicates that as deformation increases not only is the crystal becoming more compressed, but its overall CTE magnitude appears to be decreasing as well. The reduction however is to the overall magnitude of the anisotropy and does not appear to affect the overall volumetric rate of expansion in the crystal.

6.4.2 Temperature dependence of crystalline CTE

The apparent temperature dependence of thermal expansion anisotropy is quite interesting and deserves further regard both as a function of deformation and composition. Figure 6.9 shows the estimated CTE values for the orthonormal directions as a function of temperature as calculated in the CTEAS software by fitting the synchrotron data with a 2^{nd}-order polynomial function. Here the effect of composition is demonstrated by Figure 6.9(a), while the effect of deformation is illustrated for $TiNb_{22}$ in Figure 6.9(b) and $TiNb_{24}$ in Figure 6.9(c).

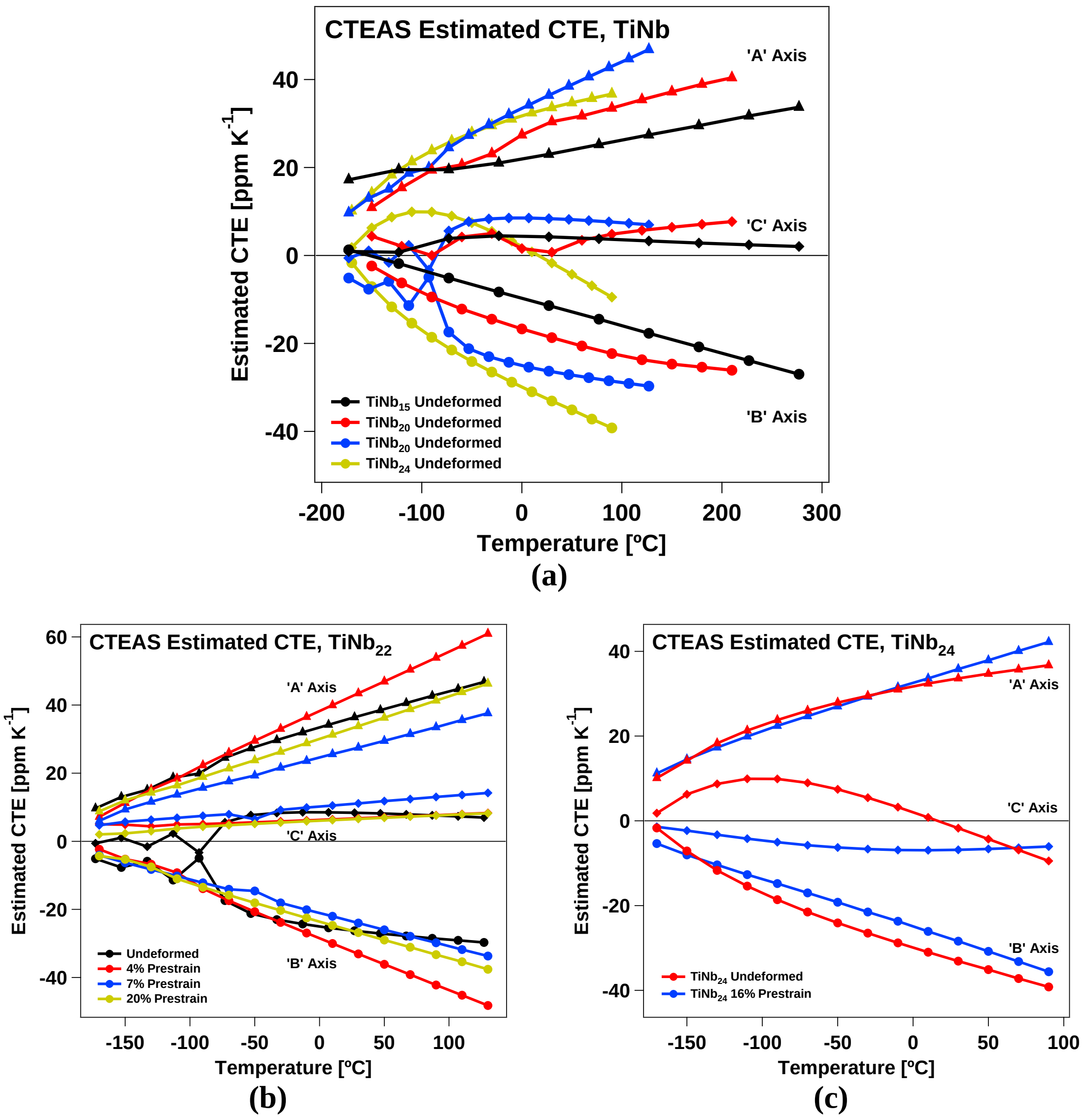

(a)

(b)

(c)

Figure 6.9 CTEAS estimated CTE values via 2nd-order polynomial fit. (a) All undeformed TiNb compositions studied in this work. (b) various deformation levels of $TiNb_{22}$. (c) the two deformation levels examined in $TiNb_{24}$.

When examining crystalline CTE as a function of composition as shown in Figure 6.9(a) clear trends emerge. The first is that at minimum temperature, all compositions appears to be trending towards some unity located, apparently, at a low positive CTE. The ‘a’ axis demonstrates large positive expansion as expected, but furthermore shows good symmetry with the ‘b’ axis if the assumption that unity lies at small positive CTE, with the same trend towards that same unity. In all compositions there is this same trend of approaching zero CTE for the ‘b’ axis as they approach minimum temperature, and of particular interest is the apparent switch in the ‘b’ axis of $TiNb_{15}$ where the fitting returns a positive value for the minimum temperature CTE. The ‘c’ axis shows little clear tendency towards a unity, rather more of a near-constant CTE when alloying for variance when fitted over the whole temperature range – given how close the ‘c’-axis CTE eigenvalue is when compared to the volumetric CTE, it may be the case that the ‘c’ axis simply already lies near unity. There is some contradiction here with previous experimental evidence that we are aware of, as prior examinations of anisotropic alloys (CoNiGa, NiTi) which approach 0 K indicate that the anisotropy does not change sign throughout the entire temperature range, which does not agree with the low-temperature trendlines estimated for the ‘b’ axis via CTEAS. This likely is indicative of fitting errors near the terminus of available data, and points to the value of truly low-temperature (to liquid helium temperatures, if possible) data in order to fully establish the nature and extent of anisotropy in any anisotropic alloy of interest.

Allowing for variance, there is a clear trend wherein the directional CTE in the ‘a’ or ‘b’ axis will possess higher magnitude as Nb content increases for a given temperature. The key difference as it appears to be is not the maximum achievable CTE for a given composition but rather the temperature at which a given CTE value would occur. The fit appears to indicate that essentially any of these alloys will demonstrate the full range of CTE experienced by any other composition. For example, $TiNb_{24}$ appears to always present the largest CTE magnitude at any given temperature before it reaches its transformation temperature, but $TiNb_{22}$ will reach those same magnitudes after heating of approximately 80 °C has occur. Focusing on the ‘b’ axis, $TiNb_{15}$ despite its minimal CTE value at room temperature can reach the same CTE value that $TiNb_{20}$ reached at 100 °C when heated to nearly 300 °C (whereas $TiNb_{24}$ shows such anisotropy at only -80 °C). Projecting forward, it seems that for these TiNb alloys in the ‘b’ axis, approximately the same maximum crystalline CTE is achieved prior to transformation occurring.

In Figure 6.9(b), the CTEAS estimated CTE values are presented as a function of deformation in $TiNb_{22}$. In general, it appears that the overall CTE magnitude decreases as a function of input prestrain. The biggest region of change according to these fits appears to occur between 4 and 7% prestrain, which in reviewing Figure 6 is consistent with the transition from variant-reorientation to plasticity as the dominant mechanism for further texture application. This likely indicates a large influence from dislocations as plasticity begins to significantly increase its density within the sample. This indicates a fundamental difference from the LP changes in Figure 6.8, where the differences between 4 and 7% prestrain are relatively modest in contrast. This likely points towards the change in LP having a more moderate effect when compared to the effects of dislocations when determining the size of impacts on CTE anisotropy.

Figure 6.9(c) shows the change in crystalline CTE as a function of temperature for $TiNb_{24}$ in undeformed and 16% prestrain condition. There appears to be little change between the two samples, but the undeformed sample still shows a degree of higher CTE similar to the response in $TiNb_{22}$. Notably the difference between the two is significantly less than the difference seen at similar prestrains in $TiNb_{22}$, which implies that the amount of effect from deformation is also-composition-dependent, likely again due to dislocations as the LP difference is small in $TiNb_{24}$ as a result of deformation, shown in Figure 6.8.

6.4.3 Effects of composition and deformation on the phenomenological switching model

There is clearly an effect on the CTE crystalline anisotropy magnitude that results from both composition selection and subsequent deformation to tailor the thermal expansion. Phenomenologically CTE is modeled as derived from random thermal fluctuations (“sampling”), similar to how liquids would also sample its crystalline forms through fluctuations before true crystallization will occur [61-63]. Because this creation and subsequent destruction is a rapid but not instantaneous process this implies the continued overall presence of some statistical population of sampled proto-beta phase for a given time interval. then it can be represented how such influences would affect this form of model. Here the phase being sampled is the higher temperature austenite within the low-temperature martensite, and the influence of the sampling upon the overall behavior of the material is tied to both the size of the statistical sampling population (the total amount of thermal fluctuations occurring per unit time) and the rate of change in the sampled population with temperature. This relationship can be understood as such: at a given temperature the alloy with a larger total sampling population will demonstrate the larger CTE anisotropy at a given temperature, and one with the larger change in the sampling rate will experience the larger change in CTE anisotropy per unit temperature.

On that basis [59], the mathematical function which is critical to describing this sampling process is the probability function for sampling austenite in martensite: $f^A = Be^{\frac{\Delta G^{M\to A}}{RT}}$ [29], which is a simple Arrhenius-type relationship that describes a random thermal fluctuation process. The primary variables are the proportionality constant B and the free energy of transformation from martensite to austenite, ΔG. Of the two factors in play, the one of interest in this discussion is that of the free energy difference, which can be further derived to account for its temperature-dependent nature as $\Delta G^{M\to A} = \Delta S^{M\to A} dT = \int_T^{T_0} \Delta S^{M\to A} dT = \Delta S^{M\to A}(T_0 - T)$ [29], which is dependent on the assumption that the entropy difference and enthalpy is relatively constant over a large temperature range.

Both factors in the free energy relationship can easily be connected to their likely roles in this phenomenological model of sampling. The entropy of transformation in the range studied is expected to have a small overall change as a disordered alloy, which means that the larger role of composition upon sampling is thus reflected in the change of the transformation temperature T_0. A higher-temperature composition would require larger effective energy input for a given amount of sampling and would also have a smaller change in free energy per unit temperature, which both act as barriers against sampling. As the transformation temperature increases, it raises the effective free energy difference for a given temperature value, which reduces the total amount of energy available for thermal fluctuations (as well as per unit fluctuation) and hence reduces both the overall sampling amount and rate. This likely also provides at least a partial explanation for the nonlinearity of strain vs temperature observed in the lower-temperature $TiNb_{20}$, $TiNb_{22}$, and $TiNb_{24}$ compositions when compared with $TiNb_{15}$, as in the range examined the ΔT can become very small as the samples approach their real transformation temperatures, while $TiNb_{15}$'s examined temperature range still retains a large effective ΔT even at 300 °C. Were $TiNb_{15}$ to be heated to over 400 °C, it is possible that it would also show a nonlinear increase in strain vs temperature with maximum CTE values approaching the higher-Nb compositions explored in this work.

In contrast to composition, deformation appears to work by directly affecting the entropy of transformation through increasing the overall entropy of transformation and is independent of temperature. While the overall ΔS contribution is likely to be quite small as it is in most SMAs [64-66], in TiNb alloys which already possess extremely low entropy differences ($-1.3\ \mathrm{J\ mol^{-1}\ K^{-1}}$ in $TiNb_{26}$) [67], even such small contributions will have noticeable effects on the CTE over such large temperature ranges. Deformation likely needs to be accommodated in the above equation through addition of an additional additive term to the overall ΔS equation to represent the temperature-independent dislocation hindering of sampling.

6.4.4 Deformation and Resultant CTE

Figure 6.7 demonstrates the change in *engineering strain* against temperature for the four compositions examined in this study. However, to compare the actual thermal expansions of the sample at these different deformation strains and hence resultant gauge lengths first requires that the engineering CTE values be subjected to a correction which can be expressed as $CTE_{Real} = CTE_{Engineering} * (1 - \varepsilon_{UL})$, where ε_{UL} represents the engineering strain of the sample in the cycle after it has been unloaded back to 10 Newtons force following deformation. This correction removes the systemic error that results from measuring the strain change vs temperature when the sample is increasing in length in discrete steps.

A summary of the resultant CTEs for the relevant three tailorable CTE alloys after correction is given in Figure 6.10. $TiNb_{15}$ did not need to be included in Figure 6.10 as the apparent CTE does not change as a result of correction as seen in Figure 6.7(a) – its thermal expansion simply remains identical to the undeformed sample expansion measured in the other TiNb samples. For the remaining three compositions however the effects of deformation upon the resultant tensile-direction CTE is made plain. There is a strong divide in the behavioral response between $TiNb_{20/22}$ and that of $TiNb_{24}$: for $TiNb_{20}$ and $TiNb_{22}$ there is a gradual decrease in CTE until necking occurs after the initial more rapid response, while for $TiNb_{24}$ this evolution is much more localized to the latter region. In all cases the final terminus for CTE increase is in fact the onset of necking as comparison with the stress-strain diagrams in Figure 6 shows that plasticity response still has an overall positive influence towards achieving the desired aligned texture.

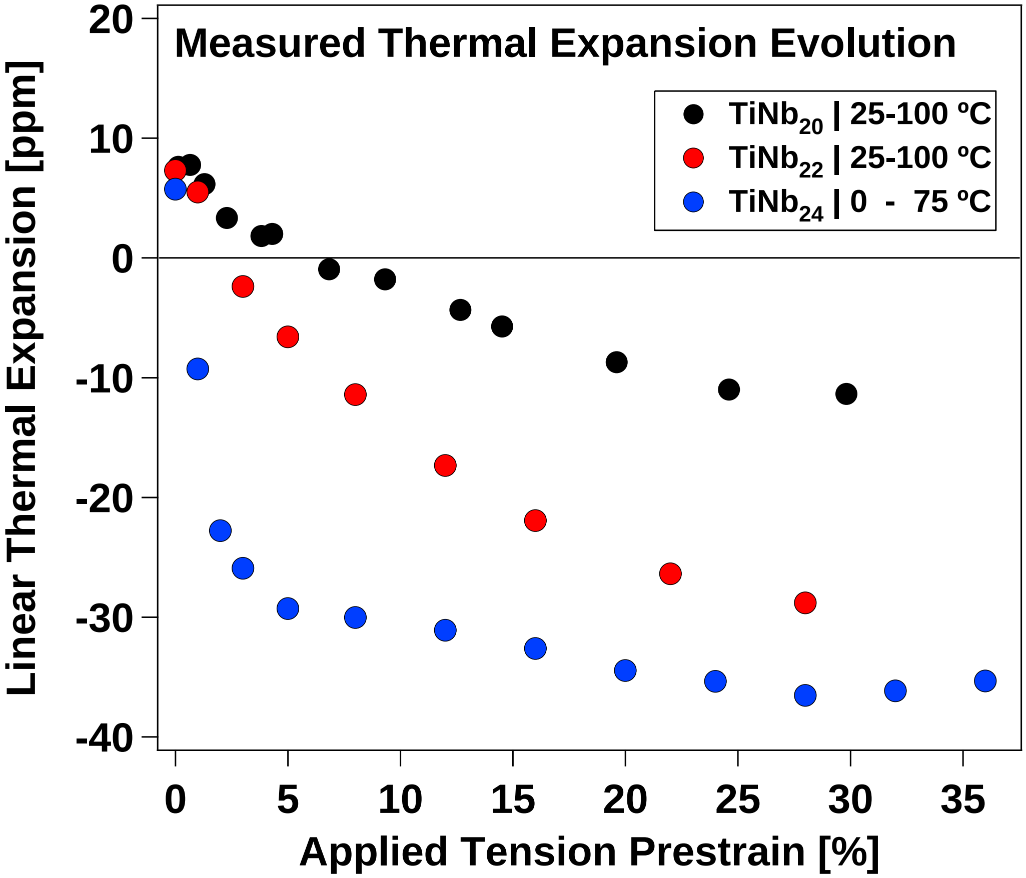

Figure 6.10: Average linear thermal expansion expressed by tension samples during cooling at target prestrain deformation levels during iterated test. A 75 °C temperature window is utilized for all cases.

The fast-onset of CTE in $TiNb_{24}$ is likely due to an ease of reorientation relative to the lower-Nb compositions indicated by its much lower yield stress. The lack of subsequent change in CTE (nonzero but much less than that of $TiNb_{20}$ and $TiNb_{22}$) would appear to indicate that the reorientation is sufficiently easy that the material is largely fully textured before significant slip may occur, leaving less remaining texture change to be elicited by future plastic deformation. This remains evident even in $TiNb_{20}$ and $TiNb_{22}$, where it can be observed that there are generally two slope regions of CTE during deformation. This first, more rapid evolution occurs in $TiNb_{20}$ until approximately 6% prestrain and near zero CTE, while in $TiNb_{22}$ this appears to occur instead at 8% prestrain near -15 $ppmK^{-1}$ CTE, although the evolution of $TiNb_{22}$ is sufficiently gradual as to be less stepwise in nature. This again indicates a less-complete retexturing during the initial variant reorientation and detwinning process followed by further retexturing during plasticity.

In all it can be observed that for the temperature range investigated the highest bulk polycrystalline CTE magnitude is observed in $TiNb_{24}$ just prior to the onset of necking (28% prestrain) with -36 $ppmK^{-1}$ linear average CTE over a 75 °C temperature range. Likewise, the maximum negative CTE for $TiNb_{22}$ at slightly higher temperatures is -27 $ppmK^{-1}$ at the same prestrain, and for $TiNb_{20}$ -10 $ppmK^{-1}$. The response to necking was stronger in $TiNb_{24}$ where some bounce back after the peak was observed, while for $TiNb_{20}$ the resultant CTE changed little after hitting its maximum. While there are differences in the crystalline CTE as determined in the prior section, the differences between bulk CTE in $TiNb_{20}$ and $TiNb_{22}$ are significantly larger than that of the crystalline CTE, indicating a loss of maximum favorable texturability in that alloy. This indicates that TiNb20 lies along a pathway of decreasing texturability as Nb content decreases in α’’ martensite, ultimately culminating in the near complete loss of texture response to plasticity observed in $TiNb_{15}$.

6.4.5 Texture after deformation and resultant CTE

As our explanation for the bulk tailored thermal expansion rests on the idea that the texture of the anisotropic polycrystals determines this resultant CTE it would therefore be informative to examine the evolution of the texture as it is deformed. In Figure 6.11, the inverse pole figures for various deformations and directions in the $TiNb_{22}$ alloy were plotted from MAUD texture data in MTEX.

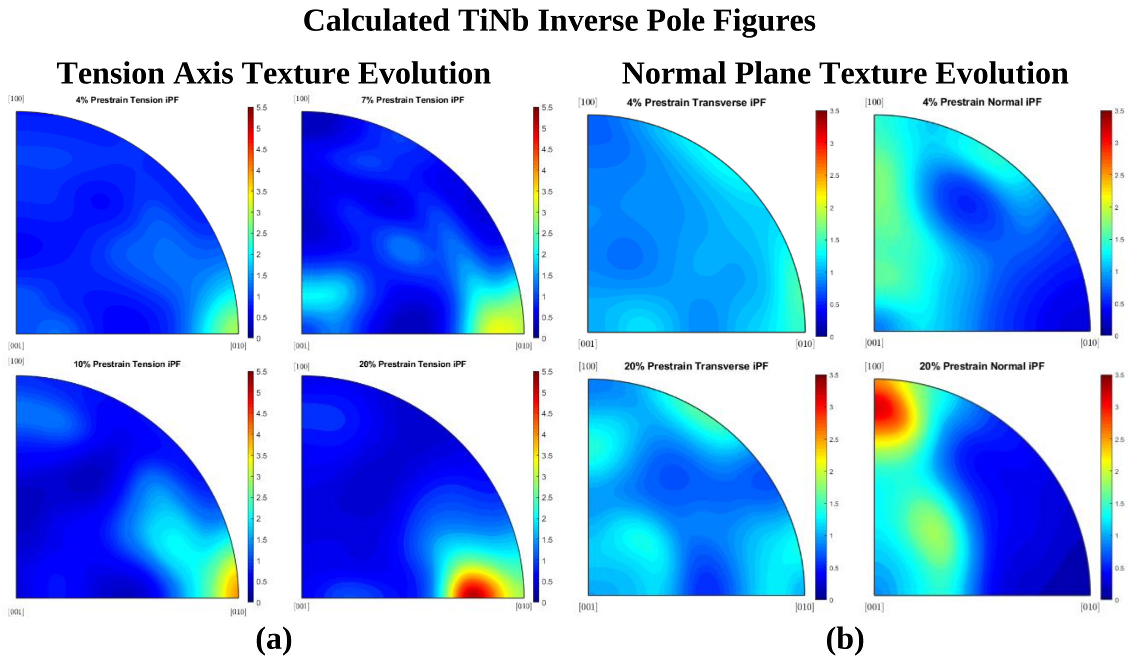

Figure 6.11: Calculated inverse pole figures of deformed $TiNb_{22}$ samples. (a) tension direction inverse pole figures. Clockwise from top left: 4, 7, 10, 20% prestrain. (b) transverse and normal direction inverse pole figures. Top: 4% prestrain. Bottom: 20% prestrain.

In the left half of Figure 6.11, we see the tension direction inverse pole figures for 4, 7, 10, and 20% prestrained $TiNb_{22}$ samples, all set to a range of 0 and 5.5 relative intensity. Compared to the semi-random texture caused by self-accommodation of martensite in an undeformed TiNb polycrystal there are significant changes as early as 4% prestrain which corresponds to the middle of the fast CTE change region. Already there is an evident strong (and nearly exclusive) association with the ‘b’ axis martensitic orientation demonstrated by the peak centered on the [010] corner. This relationship continues as prestrain increases, with peak intensities increasing from 3 to 3.3, 3.7, and finally 5.2 relative intensity at 20% prestrain. Despite the small shift away from the ideal [010] orientation in 20% prestrain possibly due to higher strain plasticity or deformation twinning effects, the overall increase in the texture strength is more likely compensating leading to the continued decrease in tension CTE seen in Figure 6.10. As it can also be seen in 7% prestrain, it is more likely caused by minor sample misorientation or sample-to-sample variance.

The apparent deformation pathway demonstrated by these inverse pole figures appears to be a swift primary onset of overall orientation (which is in line with how detwinning reorientation commonly manifests in SMA martensites) followed by a slow increase in the strength of that orientation as further stress encourages continued detwinning through less favorable variant orientations and eventual formation of plastic twins and dislocation slip planes. This evolution continues until the onset of necking when stress no longer allows for plastic deformation of the rest of the sample.

In the right portion of Figure 6.11 the texture evolution of the plane normal to the tension force is examined when normalized to between 0 and 3.5 relative intensity. For the purposes of identification, the normal is defined as the thin (1.5 mm) direction in the gauge cross-section while the transverse is defined as the thick (3 mm) direction. Here the 4 and 20% prestrain cases are shown to demonstrate the texture both after significant detwinning and then after significant plastic slip. Again, compared to the semirandom self-accommodated structure, there is already preferred orientation being demonstrated in both the transverse and normal orientations by 4% prestrain. In the transverse some [010] orientation remains at this stage, but two peaks near [110] and [051] are showing strong preference as well. In the normal direction there is a clear preference towards a [011] average orientation with virtually no remnant [010] orientation. This evolution is confirmed in the 20% prestrain case, where the normal now demonstrates an extremely strong orientation towards the [100] or ‘a’ axis orientation, indicating that it would be expected to show exceptionally large positive expansion. In contrast the transverse shows an amalgamation of 4 distinct texture orientation, including a small retained [010] orientation as well as [110], [130], and [661]. The transverse appears to be the catchall direction, where the strong orientation of the tensile and normal directions is forcing it simply to accommodate what is required to preserve variant symmetry.

6.4.6 Linking crystalline CTE and texture

Given the strong textures which evolve during deformation and the strongly anisotropic crystalline CTEs demonstrated in this work, then it should follow that the interaction between the two is what is responsible for the overall bulk CTE observed. To verify this for the $TiNb_{22}$ case, the thermal expansion tensor at room temperature calculated from CTEAS for a given condition was combined with the orientation density function of the texture using the CalcTensor [68] function in MTEX. The resultant predicted bulk material property tensors are plotted in Figure 6.12 with the same color scaling.

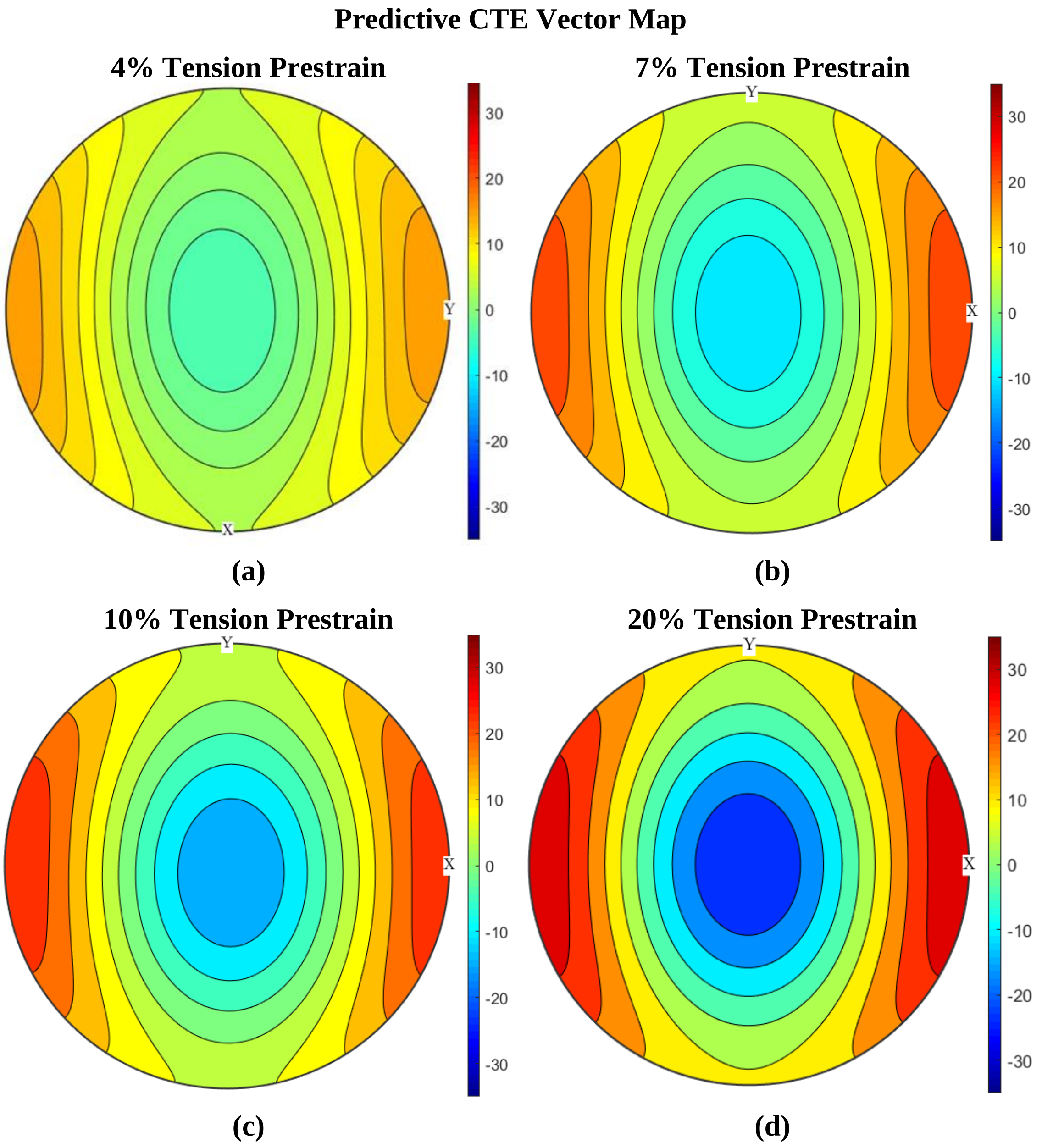

Figure 6.12: Calculated bulk CTE tensors from combining crystalline CTE tensor and texture via MTEX. Clockwise from top left: 4%, 7%, 10%, and 20% deformation prestrain.

Here the implications of the texture observed in the previous section when combined with the crystalline anisotropy are clear – as deformation level increases the magnitude of the tension and normal direction CTE increase. However the overall shape of the anisotropy which was already observed to be quite oriented in 4% prestrain changes very little between the prestrain levels, which matches the same small changes in orientation and favoring increasing texture strength which was demonstrated by the iPFs. This appears to show that there is a strong link between crystalline CTE, texture, and bulk polycrystalline thermal expansion.

6.5 Addendum – Elastic response evolution in TiNb

The evolution of the stiffness as a function of deformation and temperature was examined in a manner identical to that used in Chapters IV and V and is shown here in Figure 6.13.

It can be seen in Figure 6.13(a) that there is some effect on the single-temperature elastic modulus as deformation is applied through the initial reorientation region, with the stiffness decreasing in $TiNb_{20}$ and $TiNb_{22}$ by approximately 10 GPa. However, the initial effect in $TiNb_{24}$ can be observed as being more significant initially, followed by a reversion after large deformation to the same 10 GPa overall impact. It appears that alignment of the martensitic elastic anisotropy does have the expected effect of reducing the elastic modulus by incorporating a larger percentage of the softer long side of the orthorhombic crystal.

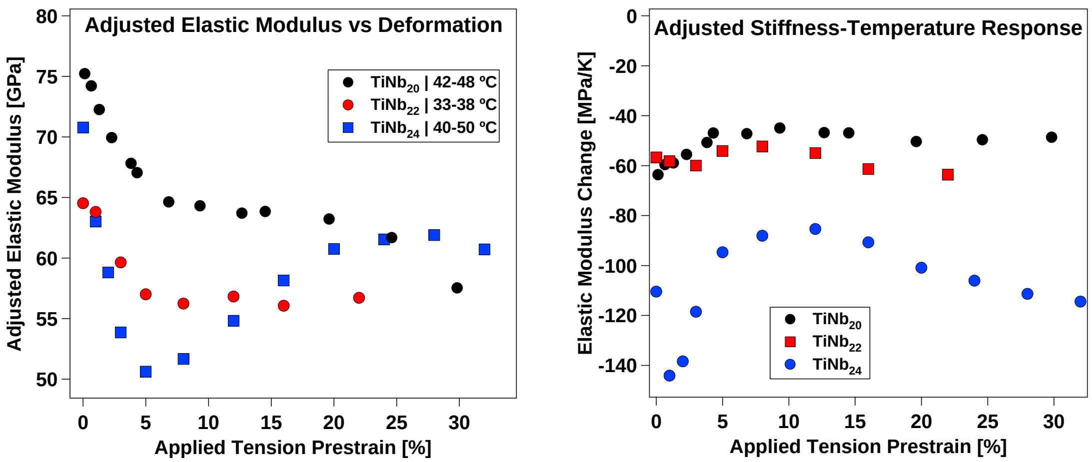

(a) **(b)**

Figure 6.13 Adjusted measured elastic modulus and stiffness-temperature for TiNb. (a) elastic modulus within a specific temperature range (indicated in the legend) for the three TiNb alloy compositions studied in this work plotted as a function of sample deformation. (b) Stiffness-temperature response over the full temperature range for a given TiNb alloy composition.

Figure 6.13(b) shows the evolution of the stiffness-temperature relationship as a function of deformation and composition. The effect can be best described as minimal in 20 and 22% Nb compositions with some initial deflections occurring during the bulk variant reorientation phase. This effect is more pronounced in $TiNb_{24}$ where the stiffness constant varies quite wildly in the first few percent of strain as alignment is imposed, although this is followed by a reversion towards the mean. The lack of response to deformation in regards to the stiffness-temperature constant is believed to be due to the disordered nature of the TiNb crystal as opposed to the ordered NiTi and NiTiPdTa, which does not create sufficiently cooperative bonding as to allow for the anticipated stiffness effects.

6.6 Conclusions

In this study various compositions and tensile deformed samples of the TiNb binary alloy system which had been quenched into α’’ martensite were examined by synchrotron and *in-situ* tension to evaluate the crystalline CTE, polycrystalline texture, and bulk tension property evolution. Evaluation of the crystalline strain response as a function of temperature it was observed that the lattice strain change with temperature for TiNb was largest when Nb content was also highest, with the largest effective CTE being found in $TiNb_{24}$ (at%) alloys, which also possesses the smallest maximum temperature before initiating transformation. Reduction in Nb increased the potential maximum working temperature, at the expense of overall CTE anisotropy magnitude. In a similar fashion, examination of bulk tension samples showed a similar behavior, where lower-temperature, higher-Nb compositions resulted in higher measured CTE in the tensile direction at lower deformation prestrain levels. The apparent level of response to deformation showed a clear dependence on composition, with $TiNb_{24}$ alloys demonstrating high ease of total texturability, while $TiNb_{15}$ demonstrated no apparent texturability despite retaining the crystalline anisotropy. Deformation was also observed to influence the crystalline CTE, where it led to a decrease in CTE anisotropy magnitude as the applied deformation increased. Examination of the texture at various deformation levels showed a desirable texture evolution for maximizing the CTE anisotropy via crystalline CTE. When combining crystalline CTE tensors with the measured texture the predicted CTE showed good agreement with experimental results, demonstrating the likely causation for bulk CTE anisotropy in TiNb alloys.

CHAPTER VII

EVOLUTION OF ANISOTROPIC AND NEGATIVE THERMAL EXPANSION IN ROLLED EQUIATOMIC NICKEL-TITANIUM MARTENSITE*

NiTi demonstrates crystalline CTE ranges between -25 and +35 ppmK^{-1} [15, 16, 39]. Anisotropic CTE at macroscale in polycrystalline samples has been shown by Ahadi *et al.* [16], where nickel-rich NiTi was demonstrated to exhibit up to -10 ppmK^{-1} negative CTE in the rolling direction at thickness reductions between 40 and 60%. However as shown in [15], much of the desired texture evolution is due to martensite reorientation at low strains, thus it is possible that the highest anisotropic CTE may occur at much lower rolling reductions. This would simplify processing as high deformation levels in NiTi is difficult to achieve due to its somewhat brittle intermetallic nature. Larger rolling reductions may also be detrimental for achieving large CTE magnitudes since dislocation slip can cause undesired changes in texture and work against texture evolution from martensite reorientation at lower strain levels.

---

*Reprinted with permission from “Evolution of anisotropic and negative thermal expansion in rolled equiatomic nickel-titanium martensite” by Gehring, D, and Karaman, I, 2020. Scripta Materialia 186, pp. 142-146, Copyright 2020 by Acta Materialia Inc. published by Elsevier Ltd. DOI: 10.1016/j.scriptamat.2020.03.058

Moreover, because of the complicated nature of plastic deformation in martensite [69-71], it is not well-known how crystallographic texture evolves at high strain levels, and what effect deformation-induced martensite stabilization may have on the potential operating temperature range for CTE anisotropy.

7.1 Calorimetry

The DSC results for all samples are shown in Figure 7.1.

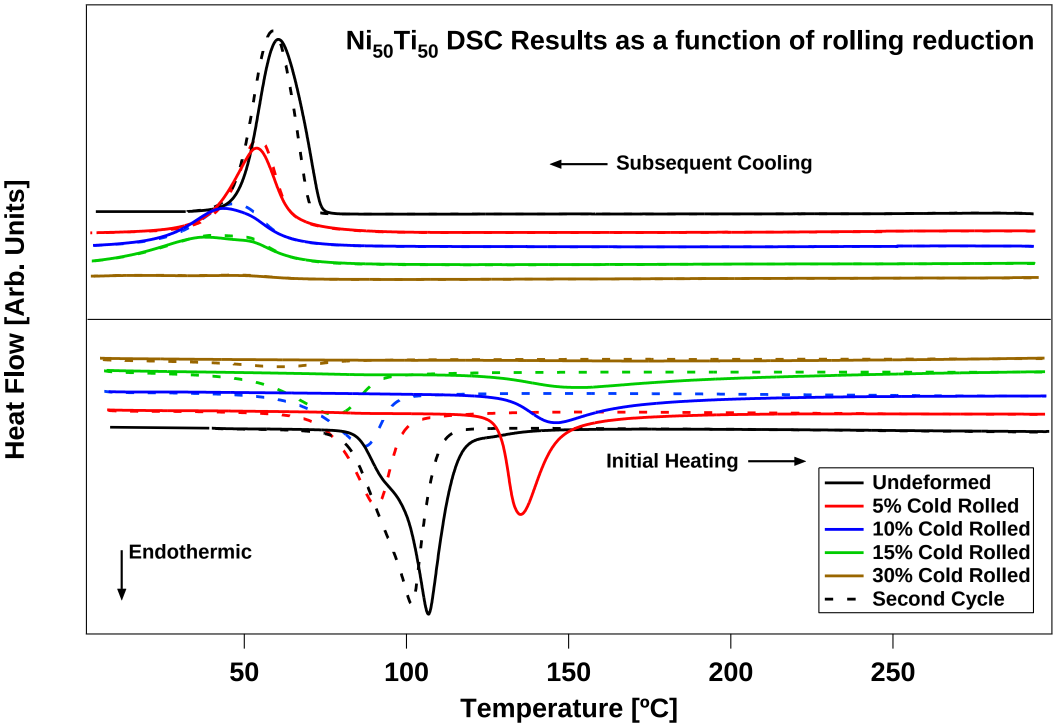

Figure 7.1 Differential Scanning Calorimetry (DSC) results for both the undeformed (as-quenched) and cold-rolled equiatomic NiTi shape memory alloy. Seen as a function of the rolling reduction, displaying how the rolling reduction affects the transformation characteristics during heating in the first cycle and subsequent cooling with comparative responses for the second cycle.

For the as-received condition, the martensite start (M_s) temperature was 70°C and austenite finish (A_f) temperature was 115°C, determined in the second DSC cycle. In the 5% rolled sample, A_f increased to 160°C during the first heating cycle due to the well-known "first heating effect" [72], before reverting to an M_s slightly below the M_s of the undeformed, as-quenched material. Subsequent rolling reductions further increased the first heating A_f temperatures reaching to 190°C at 15% rolling reduction due to the martensite stabilization. It was not possible to determine the first heating A_f temperature of the 30% rolled sample with the current upper cycle temperature of 300°C. Similarly, A_s increased from 75°C in the undeformed sample to 120°C in the 5% rolled sample. Subsequent rolling appears to have diminishing effect on the increase in A_S, as it gradually increases to 130°C by 15%, and 135°C at 30% rolling reduction. The first heating A_S temperatures are critically important in the context of tailorable CTE, as rolling increases the A_S temperature and thus, possibly extends the working temperature range relative to undeformed samples.

7.2 Thermal Expansion

The measured thermal expansion values for the rolled NiTi samples are presented in Figure 7.2. Two trends manifest through the rolling reduction space. First, the normal direction displays the highest positive CTE (up to 28 ppmK^{-1} at 5% rolling, and never below 20 ppmK^{-1}), while the CTE along the transverse direction slowly increases in positive direction as the rolling percentage increases. Simultaneously, the rolling direction shows negative CTE at all rolling reductions examined. Here the highest negative CTE occurs twice, at 5% (-10 ppmK^{-1}) and 30% (-12 ppmK^{-1}) rolling reductions, with negative CTE magnitude on a gradual parabolic curve in between these endpoints, appearing to minimize near 17.5% reduction with CTE of approximately -5 ppmK^{-1}. Clearly, the evolution of CTE with rolling reduction is not simply monotonic and presents a somewhat complicated behavior.

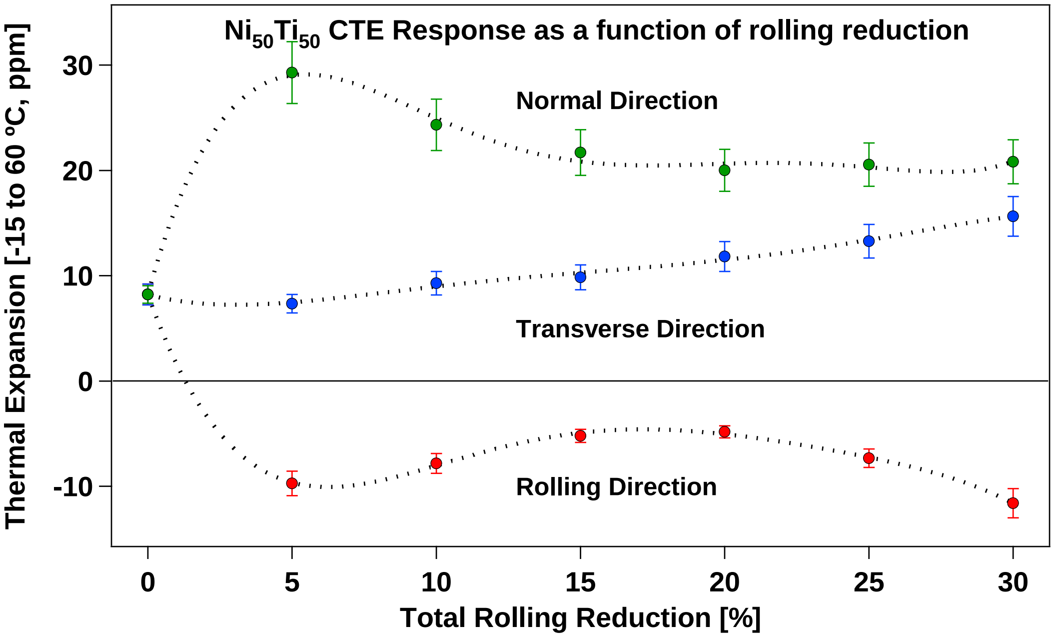

Figure 7.2 Average linear coefficient of thermal expansion (CTE) of as-quenched and cold rolled equiatomic NiTi shape memory alloy. Given as a function of the rolling reduction along three orthogonal directions of the rolled samples. Error bars represent the standard error for TMA measurements according to ASTM E831-14.

7.3 Discussion of Thermal Expansion Evolution

The reason for the unexpected change in CTE along the rolling direction with increasing reduction can be better understood by examining operational deformation modes during monotonic tensile deformation of NiTi [18, 73-79] (Figure 7.3(a)). To compare the deformation in tension vs. during rolling, the equivalent plastic strain (EPS) for rolling can be calculated as $\varepsilon_{EPS} = \frac{2}{\sqrt{3}} \left| -\ln \left(\frac{h_0}{h_1}\right) \right|$ where h_0 and h_1 are the thicknesses before and after rolling [80, 81]. 5% rolling reduction (5.92% EPS) correlates with the end of the stress plateau in the monotonic tensile response (Figure 7.3(a)), which occurs near 6% strain. This indicates that the 'Stage II' reorientation & detwinning processes [74-77] has been mostly consumed after 5% rolling. The 10% and 15% rolling reduction steps convert to 12.17% and 18.77% EPS, which correspond to Stage III deformation, governed by elastic deformation of reoriented martensite, $(20\bar{1})$ and (100) deformation twinning, and increasing levels of dislocation plasticity [74, 76, 77, 79]. Detwinning can still take place but its contribution is likely minimal. After 15% rolling reduction (18.77% EPS), the material ultimately transitions into Stage IV deformation where strain hardening rate drops off as plasticity effects become dominant while further (100), $(20\bar{1})$, and (113)/(114) deformation twins nucleate and grow [74, 76, 77]. This extends to 20% rolling reduction (25.77% EPS), which contains only Stage IV deformation. It appears that Stage II reorientation/detwinning process is the most favorable for anisotropy, and Stage III causes the start of unfavorable texturing such that the previously favorably oriented rolling and normal directions now orient unfavorably or revert to more random texturing from 5% to 20% reduction.

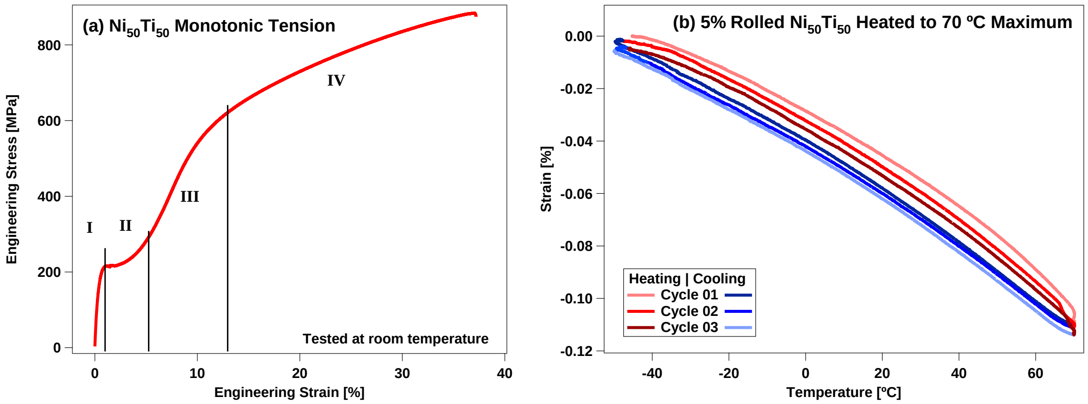

Figure 7.3 Monotonic tension test of equiatomic NiTi and TMA examination below the DSC measured A_S temperature. (a) Monotonic tension test result. (b) first 3 TMA cycles for a 5% cold rolled NiTi sample limited in heating to below the A_S observed in undeformed material (70 °C).

In contrast to the lower reduction rolled samples discussed above, 25 and 30% rolled samples experience high levels of EPS (33.22% and 41.19%, respectively) which exceed the common fracture strain of NiTi in tension [73, 74]. Therefore, the deformation modes are not quite clear. At high EPS levels, the negative CTE magnitudes and the overall anisotropy in the polycrystalline rolled samples again increase. The -12 ppmK^{-1} CTE measured at 30% rolling reduction here is somewhat higher than the -10 ppmK^{-1} observed between 40 and 60% reduction in Ni-rich NiTi [16], which points towards limited further increase in CTE. Clearly, there are two areas of interest regarding CTE evolution during rolling of NiTi, that being the low deformation region and the severely plastic deformation region, and there appears to be two separate mechanisms which enhance the CTE anisotropy in the polycrystalline samples and merit further investigation. It is clear though that there is no need to attain high rolling reductions or severe plastic deformation levels to accomplish negative CTE values or high CTE anisotropy in NiTi martensite, and it appears that extremely low reduction (<2.5%) should result in zero CTE (Invar).

7.4 Examination of strain-temperature response below and above DSC heating limits

Figure 7.3(b) illustrates the strain evolution after 5% rolling as the furnace is heated to 70°C, below the A_S of undeformed NiTi. While there are some progressive strain peculiarities during the first and last 10°C of each heating ramp caused mainly by the disconnect between the measured furnace temperature and the actual sample temperature, the linear ramps for all three cycles appear to match, especially when comparing the cooling responses. This consistency in repeated heating-cooling responses is retained for all rolling reductions under this heating condition, providing validity to the observed CTEs in Figure 7.2.

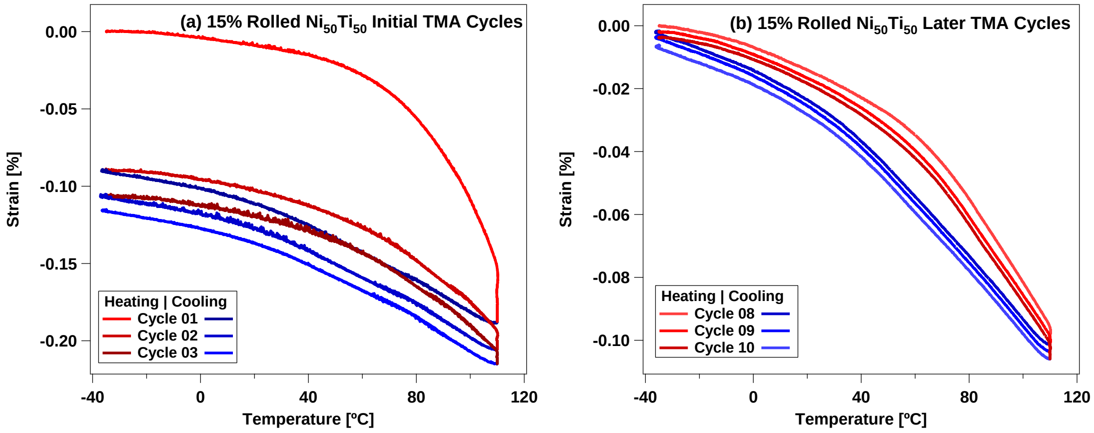

Figure 7.4 Strain vs. temperature response of the 15% cold-rolled NiTi. Heated to temperatures approaching the A_s temperature measured in the first heating cycle in DSC (Fig.1) but above the A_s temperature of the initial as-quenched material. (a) First three heating-cooling cycles. (b) Final three heating-cooling cycles (cycles 8th through 10th).

Four of the rolling reduction cases (5, 10, 15, and 30%) had additional samples each heated to a furnace temperature within 10°C of the first heating A_S measured in DSC for that specific rolling amount. As an example, TMA thermal cycling response of the 15% rolling case at two different times is illustrated in Figure 7.4 with a furnace maximum temperature of 110°C. As can be seen in Figure 7.4(a), above 70°C there is a significant contraction which occurs during the first heating cycle. Subsequent ramps become more consistent, with the first cycle cooling response matching the subsequent second and third cooling ramps, and the second and third cycle heating ramps being similar, although adjustments still occur during the isothermal hold after each heating. The 8th through 10th thermal cycles are shown in Fig.4b. In contrast to the initial cycles in Fig.4a, here the strain-temperature response during the three cycles is consistent. Two inflection points are apparent, which appear at 52°C in heating and 35°C in cooling. Examining the 15% case in DSC (Figure 7.1), these points appear to correlate with the second-cycle heating and cooling peaks, which both occur at slightly reduced temperatures, indicating that reverse transformation is likely responsible for much of this strain rate change after the first heating (cycle 1 in Figure 7.4(a)).

As illustrated in Figure 7.4, the apparent thermal contraction upon heating accelerates at temperatures above 60 to 70°C (near As temperature of undeformed material) in all rolled cases. This strain change is however not large enough for true bulk transformation. Instead thermally unstable dislocations migrate and eventually annihilate, allowing for limited relaxation of stress fields in the material and small migration of the twin boundaries with temperature, resulting in limited reverse transformation where local strain fields are favorable [82, 83]. Even with this mechanism taking place, the dislocation density near phase interfaces remains sufficiently high to block bulk military transformation [83]. This enforces retention of overall texture in the material and leads to the amplification of negative CTE values with a small two-way shape memory effect. This allows for the repeatability of the CTE response when heated and for the CTE to persist in stabilized martensite up to 125°C in 30% rolled material. Due to the higher contraction rates as a consequence of the combination of lattice level negative CTE and the two-way shape memory effect, second-cycle cooling from 100 to 25 °C (a 75°C measurement range transposed relative to Figure 2) showed apparent linear CTE rates of -16.0, -14.6, -8.9, and -17.4 ppmK^{-1} for 5, 10, 15, and 30% rolling reductions respectively, which represent a nearly 50% increase in measured CTE when compared to the 70°C maximum temperature case. As this appears to be repeatable, it may illustrate how to maximize both the potential CTE magnitude *and* temperature range in tailorable CTE NiTi.

7.5 Summary and conclusions

In this study equiatomic nickel-titanium SMA was subjected to rolling in martensitic state to 0, 5, 10, 15, 20, 25, and 30% total thickness reductions and both transformation temperatures and orthonormal CTEs were measured. As a result of martensite stabilization, the observed A_S of the rolled NiTi increased from 75 °C to between 120 and 130°C for materials rolled to 5% or greater thickness reduction. The orthonormal CTE measurements demonstrated peak negative CTE values along the rolling direction at 5% and 30% reductions, indicating the operation of two distinct mechanisms. The first is driven mainly by martensite variant reorientation, while the second is attributed to severe plastic deformation and activation of different deformation modes such as deformation twinning and slip, similar to what is observed in tensile deformation stages. Significant evolution of CTE occurred simultaneously along the transverse and normal directions, with peak positive CTE of 27 ppmK^{-1} in the normal direction occurring at 5% rolling reduction. Measuring the CTE along the rolling direction to temperatures indicated by first-heating DSC results demonstrated a significant increase in the apparent negative CTE values, illustrating how CTE anisotropy and operational temperature range can be enhanced. These increased negative CTE values are the manifestation of the lattice level CTE anisotropy as a consequence of texturing via martensite reorientation and the result of a narrow hysteresis two-way shape memory effect appearing due to the migration of dislocations and the twin boundaries.

CHAPTER VIII

THERMAL EXPANSION CHARACTERISTICS OF ROLLED MARTENSITIC TINB ALLOYS*

In Chapter VI, it was observed that the TiNb binary system could yield high maximum NTE in the tension direction with good flexibility. However, it is also true that the deformation process in tension is generally difficult to scale, and proper long-term implementation of TiNb alloy should be predicated on investigation and propagation of other more effective modes for scaling the applied deformation. In this chapter, the overall effects of rolling deformation will be evaluated for the case of TiNb alloys, with special attention paid to the following aspects:

1. Do the crystalline properties of the TiNb alloys used for rolling correspond well with the material used in tension? Unlike in NiTi, the rolling material and tension material generally originate from separate preparation batches.
2. Do the evolutions of CTE as a result of rolling correspond well to tension responses, and the postulated effects of composition on the deformation response laid out in the prior chapter?

---

*Portions of this chapter are reprinted with permission from “Effects of Composition on the Mechanical Properties and Negative Thermal Expansion in Martensitic TiNb Alloys” by Gehring, D, Monroe, J.A. and Karaman, I, 2019. Scripta Materialia 178, pp. 351-355, Copyright 2019 by Acta Materialia Inc. published by Elsevier Ltd. DOI: 10.1016/ j.scriptamat.2019.11.052

3. How does the CTE and texture evolve in three dimensions, rather than one, as a result of the rolling deformation?
4. Can variation in rolling temperature affect thermomechanical processing results and how?

8.1 Examination of the fundamental properties in undeformed TiNb intended for rolling deformation

8.1.1 Crystalline properties

XRD scans at different temperatures can be seen in Figure 8.1.

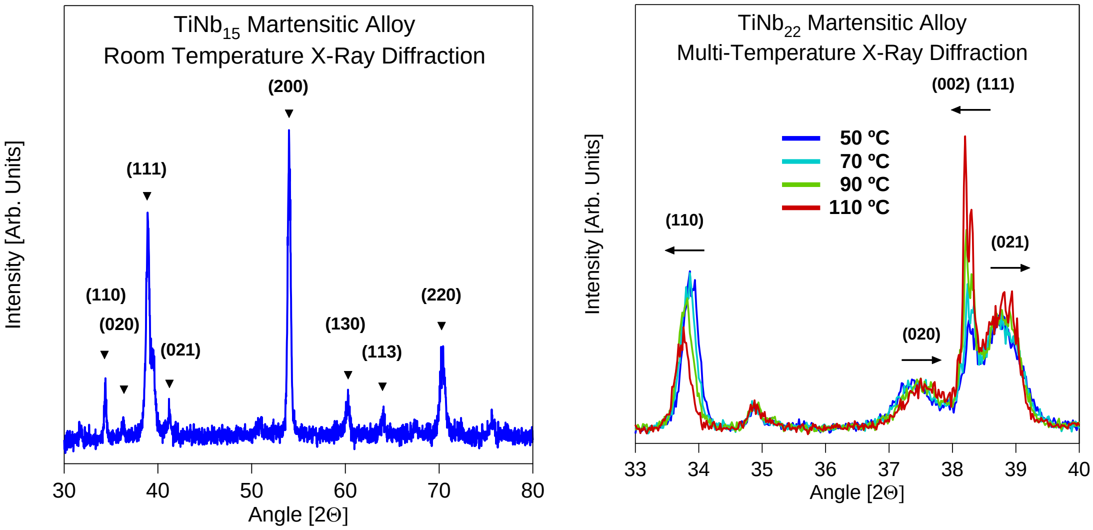

(a) (b)

Figure 8.1 Room temperature X-Ray Diffraction scan examples for TiNb alloys. (a) the $TiNb_{15}$ martensitic alloy (b) Details of the scans of the $TiNb_{22}$ alloy illustrating the evolution of the peak positions with temperature. Leftward shift of the peaks points out conventional thermal expansion with heating, and rightward shift means thermal contraction upon heating. Arrows on top of each peak demonstrates the direction of the shift with the temperature.

Figure 8.1(a) displays the intensity of the peaks as a function of 2θ for $TiNb_{15}$. The peaks are typical for orthorhombic α”-martensite. Only a small number of peaks provided high peak-to-background ratios, and thus, the (200), (113), (130), (022), and (020) peaks were selected for further examination. Figure 8.1(b) shows XRD scans at various temperatures in martensite for $TiNb_{22}$. Here, it can be seen how the peaks shift with temperature. The (110), (002), and (111) peaks move to the left as temperature increases. When converted to d-spacings, these leftward movements indicate expansions in the lattice upon heating. By contrast, the (020) and (021) peaks move rightward, indicating a lattice contraction in the direction of these planes upon heating (a negative CTE).

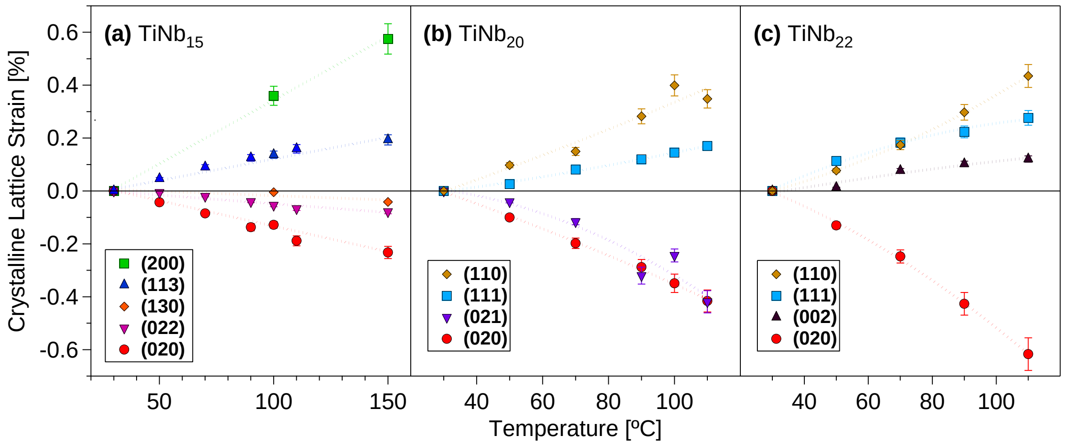

Figure 8.2 Calculated lattice strain change for TiNb alloys. (a) $TiNb_{15}$, (b) $TiNb_{20}$, (c) $TiNb_{22}$ martensitic alloys, based on the changes in the d-spacings as a function of temperature, measured using XRD (Fig. 2).

In Figure 8.2, the crystalline lattice strains as a function of temperature are displayed for the three compositions. The (020), (021), and (130) planes show contraction upon heating in all compositions. The CTE along the [020] direction ranges from approximately -30$ppmK^{-1}$ in $TiNb_{15}$ to -70$ppmK^{-1}$ in $TiNb_{22}$ between room temperature and 110°C. For the (110) plane, the net change in the d-spacing with temperature is significantly positive; this suggests that the rate of expansion along [100] is greater than the rate of contraction along [010]. As the (110) expansion rate is the difference between the (200) and (020) plane expansion rates, the (200) expansion can be estimated to exceed 100 $ppmK^{-1}$ in $TiNb_{22}$ in order to achieve a positive thermal expansion in the (110) planes. The (002) plane shows small expansion upon heating. By multiplying the orthonormal expansion rates by their associated lattice parameter, the volumetric expansion can be calculated as approximately 10 $ppmK^{-1}$ in the same temperature range.

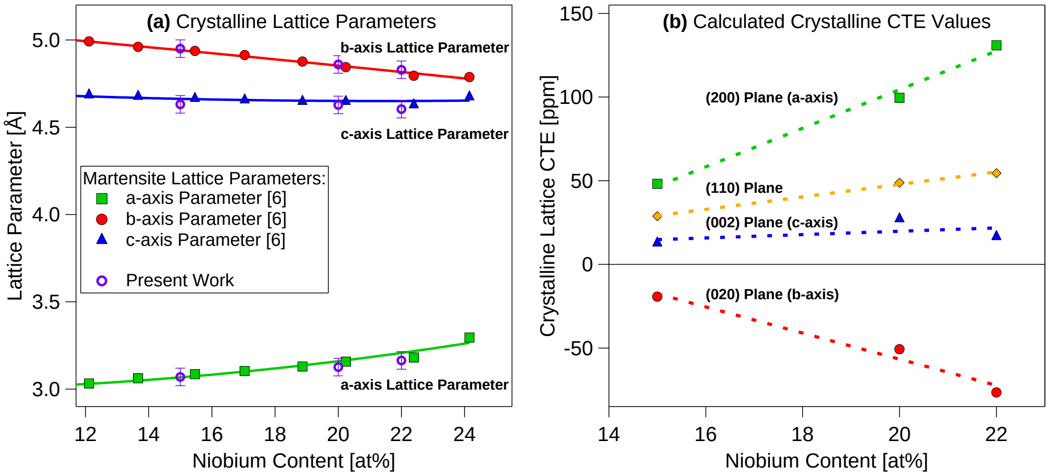

Figure 8.3 Lattice parameter and CTE anisotropy evolution in TiNb alloys. **(**a) The lattice parameters of the martensitic (orthorhombic) α'' and austenitic (cubic) β phases as a function of the Nb content in TiNb martensitic alloys, as determined by Boenisch *et al* [58] and measured in the present work. (b) Summary of the crystalline level lattice CTE as a function of the Nb content along the orthonormal martensitic crystal directions.

The overall magnitudes of the lattice strain slopes in Figure 8.2 (i.e. lattice CTEs) is explored further in Figure 8.3. Figure 8.3(a) displays the lattice parameters of orthorhombic martensite as a function of Nb content [58]. Figure 8.3(b) presents the martensitic CTEs along the low index directions, calculated using the change in the d-spacings with temperature in Figure 8.2. Comparing Figures 8.3(a) and (b), it appears that martensitic CTE magnitude and anisotropy increase as the distortion between martensite and austenite phases represented by the martensitic c/a ratio decrease. This result is consistent with that of previous work [15] in which high CTE was observed in materials where good compatibility between the two phases was evident.

In addition to the observed relationship between the martensite c/a ratio and lattice CTE anisotropy, another correlation exists between the anisotropic martensite lattice CTE and martensitic transformation temperatures in TiNb alloys. The lattice CTE anisotropy increases as the transformation temperatures decrease with increase in Nb content. The existence of this correlation can be rationalized using an atomistic mechanism based on statistical thermodynamics, that we have hypothesized here to explain the anisotropic lattice CTE in martensitic alloys, as summarized below.

We propose that while in martensite phase, austenite phase is constantly sampled by random thermal fluctuations. This is similar to how a liquid phase sample its crystalline form due to random thermal fluctuations, but this is quickly destroyed by subsequent thermal fluctuations [61-63]. The sampling rate is dependent upon the free energy difference (ΔG) between the two phases at the temperature where this sampling occurs.

The free energy difference can be thought as the activation energy for sampling while ambient heat determines the thermal energy available for sampling. As a more relevant example to the proposed mechanism, sampling between different lattice configurations of ferromagnetic and antiferromagnetic phases with small ΔG was proposed as a well-accepted reason for the conventional Invar effect in Fe-Ni alloys [2, 4]. Similar to the present martensitic alloys, statistical sampling of the antiferromagnetic phase in the ferromagnetic phase due to random thermal fluctuations leads to zero CTE as a result of the large volume change between these magnetic orders (the volume change compensates conventional thermal expansion). More importantly, this mechanism occurs at temperatures below the Curie temperature in a temperature range more than 200ºC [4]. Similarly, if the configurational sampling really occurs between martensite and austenite in martensitic alloys as proposed, then along any given martensite lattice vector, if the interatomic distance along this lattice vector is greater than the interatomic distance along the same vector in statistically sampled austenite, the martensite lattice along this particular vector should contract when heated. In other words, the specific martensitic lattice direction should exhibit negative CTE. Similarly, when the interatomic distance along a given direction in martensite is shorter than that along the equivalent austenite direction, then the particular martensite direction should display positive (normal) thermal expansion during heating.

This is indeed what is observed in TiNb and many other martensitic alloys [15, 27, 54, 84-88], even when the sample is apparently fully martensitic and CTE is measured at temperatures well below A_s temperature. The free energy difference between austenite and martensite in many thermoelastic systems is quite low [64-67, 88] and for TiNb and NiTi can be comparable to the difference described in Fe-Ni Invar alloy [2, 4]. The energy barrier for thermal fluctuations derived is a product of the transformation entropy and the difference between the test temperature and the transformation temperature. For $TiNb_{26}$ this entropy difference has been estimated as -1.348e-5 eV/atom-K [67], which is the only empirical measurement in the TiNb system we have found. Assuming this to be indicative of the entropy in the alloys studied here, then the energy barrier is estimated to be approximately 10-20% the total thermal energy in the system, 25.7 meV, at room temperature. The increase in the transformation temperature with decreasing niobium content results in a higher energy barrier at a given temperature, which implies a decrease in the total fluctuations occurring. This will resolve into a lower rate of change in thermal fluctuations with temperature and reduced effect on CTE anisotropy despite the larger lattice mismatch in low Nb alloys, which reflects the behaviors observed in $TiNb_{15}$, $TiNb_{20}$, and $TiNb_{22}$. It is clear that this extremely low energy barrier is key to the thermal expansion anisotropy and enables the wide temperature range of this behavior. Further investigation of where this energy barrier becomes prohibitive will be required to better characterize why this occurs.

8.1.2 Mechanical Properties

The lattice level CTE anisotropy and negative CTE values in TiNb martensites clearly are composition dependent. The natural question then is how the lattice level negative CTE can be practically exploited in macroscopic, polycrystalline bulk samples and which composition would be more likely to demonstrate negative CTE in polycrystals. This would occur if martensite variants can be easily textured, along the crystallographic directions that exhibit negative CTE, via martensite reorientation/detwinning without significant interference from plastic deformation. In order to evaluate the ease of crystallographic texturing as a function of composition in the present TiNb alloys, the simplest method is to determine their mechanical response, in particular the shape of the stress-strain response, in martensite, and compare the stress levels for detwinning and plastic deformation.

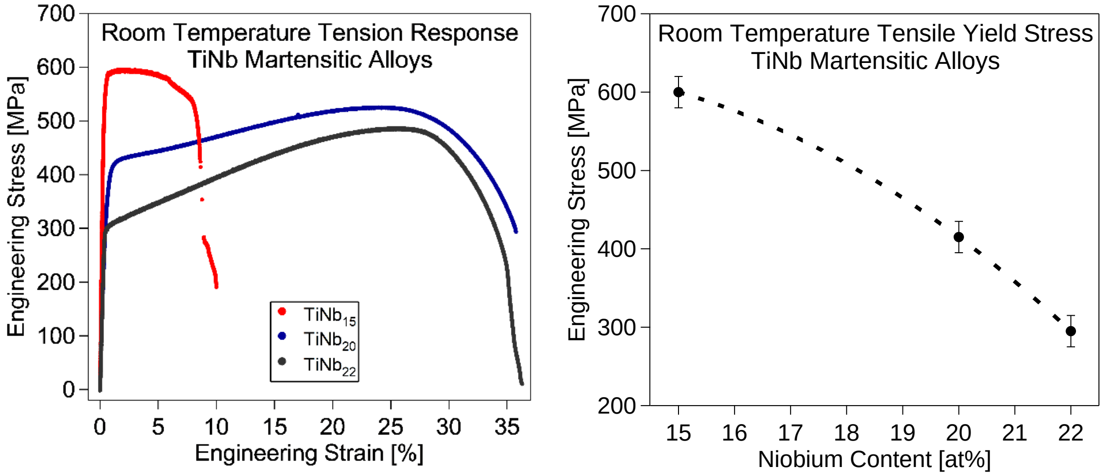

(a) **(b)**

Figure 8.4 Room temperature monotonic tension properties of TiNb alloys. (a) Room temperature tensile response of the TiNb martensitic alloy compositions studied, and (b) observed yield strengths of these alloys as a function of composition.

With this goal in mind, Figure 8.4(a) demonstrates the tensile mechanical responses of the present TiNb alloys. The shape of the stress-strain response for $TiNb_{15}$

obviously different than the other compositions and $TiNb_{15}$ exhibits the lowest tensile ductility, which may constitute an issue against achieving proper texturing for bringing out negative CTE in polycrystalline samples. Figure 8.4(b) displays that the stress for the onset of inelastic deformation at room temperature is notably higher for $TiNb_{15}$, and with increasing Nb, this stress level drops. Radically different tensile responses are indicative of the availability of martensite reorientation/detwinning pathways in $TiNb_{20}$ and $TiNb_{22}$ alloys, as opposed to $TiNb_{15}$, that should allow easy crystallographic texturing. In both $TiNb_{20}$ and $TiNb_{22}$, the lower yield stress, small stress plateau (especially in $TiNb_{20}$), and eventual strain hardening appear indicative of martensite variant reorientation/detwinning. The majority of variant reorientation, similar to other SMAs, likely occurs near yield stress in the first few percent of deformation, and especially in the small stress plateau after the yielding [89-93]. The relatively large difference between the yield and ultimate tensile stresses in $TiNb_{22}$ can be considered as the indication of the large stress difference between the onset of martensite reorientation/detwinning and conventional global plasticity. Therefore, one can argue that $TiNb_{22}$ alloy would be the easiest and $TiNb_{15}$ would be the hardest to texture via martensite reorientation at room temperature. Combined with the notable differences in the crystal level CTE anisotropy and negative CTE values between $TiNb_{22}$ and $TiNb_{15}$ alloys, $TiNb_{22}$ would clearly be the easiest alloy to accomplish negative and/or zero CTE values in polycrystalline bulk samples.

8.2 Orthonormal Thermal Expansion of Cold-Rolled TiNb

In Figure 8.5, the orthonormal linear bulk CTE and texture evolution is given as a function of composition and rolling reduction. Figure 8.5 shows that expansion along the rolling direction becomes significantly negative in $TiNb_{22}$ and $TiNb_{20}$ and slightly positive in $TiNb_{15}$ as deformation increases. The thermal expansion of the normal direction appears to increase in proportion to the maximum negative CTE observed in the crystalline structure. In transverse directions there appears to be a smaller positive response to deformation which does not necessarily correlate with the evolution of the other orthogonal responses.

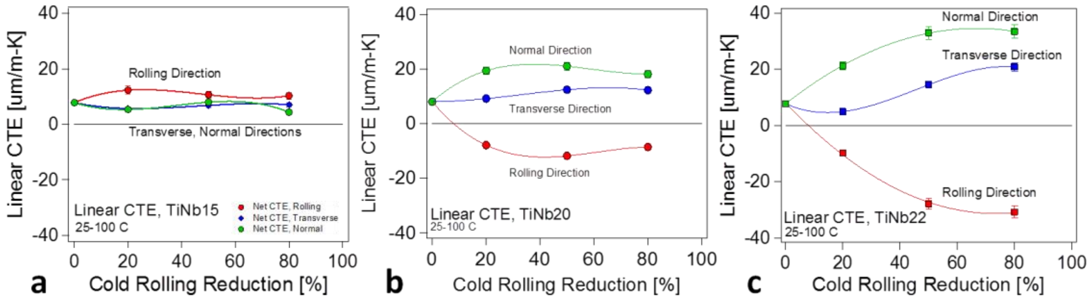

Figure 8.5 Bulk linear thermal expansion of TiNb. (a) TiNb15, (b) TiNb20, and (c) TiNb22 material in three directions relative to the applied rolling.

Interpretation of Figure 8.6 illustrates what appears to be a correlation between the evolution of alignment in the contracting b-axis observed in Figure 1 and the negative thermal expansion seen in Figure 8.5 in $TiNb_{22}$.

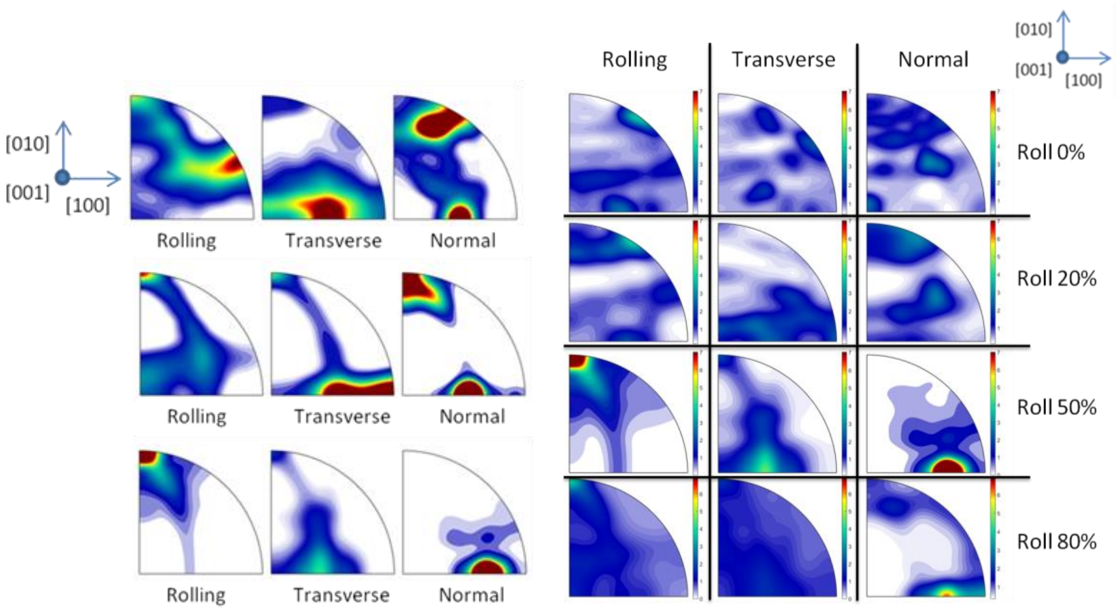

(a) **(b)**

Figure 8.6 Inverse pole figures representing the evolution of texture in TiNb. (a) Inverse pole figures for 50% reduction of (top to bottom) $TiNb_{15}$ normalized to 2.25 intensity, $TiNb_{20}$ normalized to 4 intensity, $TiNb_{22}$ normalized to 7 intensity. (b) Evolution of the texture in rolled $TiNb_{22}$ alloy.

At up to 50% reduction there is increasing orientation of the b-axis towards the rolling direction, followed by apparent stabilization of the overall texture and reduced change in bulk CTE. The higher-expansion a-axis appears to align more towards the normal orthogonal axis with increasing deformation with a lesser bias towards the transverse. Examination of the evolution of texture in one composition in Figure E-6b further reinforces these observations by demonstrating how the crystalline a- and b-axis alignment strengthens towards its preferred orientations up through 50% reduction, followed by the relative stagnation to 80%. These evolutions fit well with the observed changes in CTE in Figure 2. Generally, $TiNb_{20}$ showed similar if less strong texture to that of $TiNb_{22}$; $TiNb_{15}$ showed little texturing and was closer to random orientation than either $TiNb_{20}$ or $TiNb_{22}$ at a given rolling percentage. This suggests that $TiNb_{15}$ showing little if any CTE evolution is caused by insufficient texturing induced by deformation to significantly affect the bulk CTE. It appears that the overall texturability of the TiNb system is proportional to the niobium content as previously speculated.

The cause of the difference in texture in the three compositions likely is due mainly to the ease of martensitic reorientation and detwinning in each case. Determining the exact nature of martensite reorientation is something of an unusual topic, as the bulk of effort in SMAs has focused primarily on reorientation of variants during transformation [55, 56]. TiNb appears to lack comprehensive information such as the full list of slip and twinning systems and their activation temperatures across composition. A similar structure in single-composition α-Uranium martensite [94-97] has had some degree of attention given to these questions. Uranium underscores the difficulty in divining the deformation in these orthorhombic martensites; in that system there are 4 main slip systems and 3 twinning modes which define the deformation. There is little reason to think there are significantly less for TiNb.

In α-uranium there is a temperature effect on slip system activation. At various temperatures different slip systems and twinning modes are active, causing uranium to show radically changed deformation texture. Here the change is composition, causing a marked change in the transformation temperature. The temperature of slip activation quite possibly changes in proportion to the transformation temperature as it does in other martensitic alloys [45, 57]. Thus $TiNb_{15}$'s elevated transformation temperature implies some slip systems will not be utilized at room temperature. These are likely active in the lower temperature $TiNb_{20}$ and $TiNb_{22}$. A limitation upon available slip systems combined with a shift in the c/a ratio due to lattice parameter evolution with composition would together restrict the ability to reorient, explaining the change in texture evolution between compositions. The mobility of twin boundaries will also be determined by the temperature and the composition's energetic requirements for motion [92, 93] and will most likely be the main barrier to limit maximum variant reorientation. These considerations indicate that an intermediate composition between 15 and 20 at% Nb contains the 'critical temperature' where room-temperature cold rolling will cease texturing TiNb with sufficient effect to create the anisotropic bulk response.

8.3 Temperature effect on thermomechanical processing response

A typical TMA response to the first heating and cooling cycle when material is examined in the rolling direction is indicated in Figure 8.7(a). The normal areas of key consideration during heating are an initial linear response region, followed by an onset of a nonlinear accelerating increase in the rate of strain with temperature. This nonlinearity is not unique to the rolled TiNb; indeed, it has been observed in the tension-deformed NiTi and TiNb, as well as rolled NiTi. The main contrast in rolled TiNb relative to the others is twofold: the strain change during the initial heating is generally much larger than observed elsewhere, and the change in behavior during the cooling and subsequent cycles is more pronounced. In the TiNb rolled samples, the initial heating deflection is followed by a notably flatter curve during the cooling phase. Most importantly, the ultimate behavior of all subsequent heating and cooling behaviors (unless the maximum temperature were to be increased) becomes nearly identical to this first cycle cooling response. This does contrast with NiTi which demonstrated large strain hysteresis after rolling.

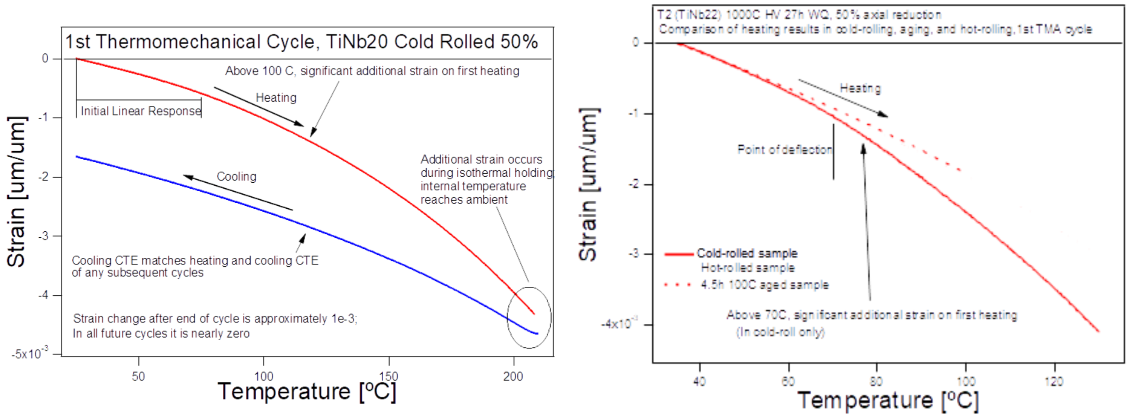

(a) **(b)**

Figure 8.7 Illustrations of the typical TMA response in the rolling direction. (a) Classic response: 50% cold rolled $TiNb_{20}$ illustrates the normal 1st cycle heating and cooling response, with notes included. (b) Comparison of the response in the first heating for cold-rolled compared with alternative higher-temperature approaches.

Considering that this first heating occurs in a thermally reactive material the ultimate cause of this strain change is likely a combination of several factors. The primary input is likely caused by thermal annealing of dislocations as the temperature increases, which is accompanied by texture reversion and transformation at the small scale in the material. One side effect of severe plastic deformation is to input dislocations to a density significantly higher than normal in the material, resulting in significant strain fields. Logically, this would result in some dislocations which are easily excited into rearranging themselves with only a small total increase in their thermal energy. As these dislocations are annealed, the local strain fields can relax slightly. This enables the most unstable martensite variants to restore themselves to a lower energy configuration relative to the local strain conditions, which may be accomplished either by transformation to austenite/omega phase or a partial shift into a differently aligned variant to relieve local stresses. While small, it is possible that this irreversible strain change can be problematic should the first heating occur at an inopportune time, such as after installation of a part prepared from this material. It can also be observed that the low-temperature NTE magnitude has also decreased slightly as a result of this first heating, which may lead to invalid design assumptions should the material be specified using its preheating linear CTE. As such, use of heating methods which reduce or eliminate the causes of this initial relaxation should be investigated.

Two methods were investigated to evaluate their ability to restrict the thermal nonlinearity, with typical results illustrated in Figure 8.7(b). The first was to preheat the material after cold rolling before measurement, typically to a temperature slightly below the maximum operating temperature used for the composition in question. In this example, the aging was carried out on a $TiNb_{22}$ sample at 100 °C for 4.5 hours. It should be noted that subsequent investigations have indicated that the time of preheating is not as important as ensuring that the sample equilibrates at the intended temperature – this aligns well with the TMA information, where the nonlinear strain occurred at a relatively high rate of temperature change rather than during long isothermal holds. The strain discontinuity illustrated in 8.7(a) is due to the sample equilibrating to the furnace temperature rather than the sample being at the target temperature. It can be observed that after such preheating in $TiNb_{22}$ the heating response is indeed approximately linear in comparison to the cold-rolled sample, with a small dip in the linear CTE similar to that seen in the cooling portion of the TMA first cycle of cold-rolled material.

An alternative method studied to the above preheating method was to instead roll the material at an elevated temperature rather than at room temperature. In this case, this would mean the material would have been preheated in the act of rolling, and therefore would not require a separate preheating step. In the TiNb22 case the rolling was performed with the sample heated to 100 °C. Illustrated in Figure 8.7(b), it can be again seen that the overall effect is to flatten the strain response to temperature, however in this case the effective linear CTE is not the same as it was in the other cases at lower temperature. Instead, the linear NTE is of a greater magnitude. This was significant and therefore investigated further.

In both $TiNb_{20}$ and $_{22}$, hot rolling was conducted at a temperature 50 °C below the mechanical A_S temperature (180 and 100 °C respectively). The was selected to give a healthy margin of safety regarding preventing accidental transformation to austenite. The results of such rolling are shown in figure 8.8 for the $TiNb_{20}$ case.

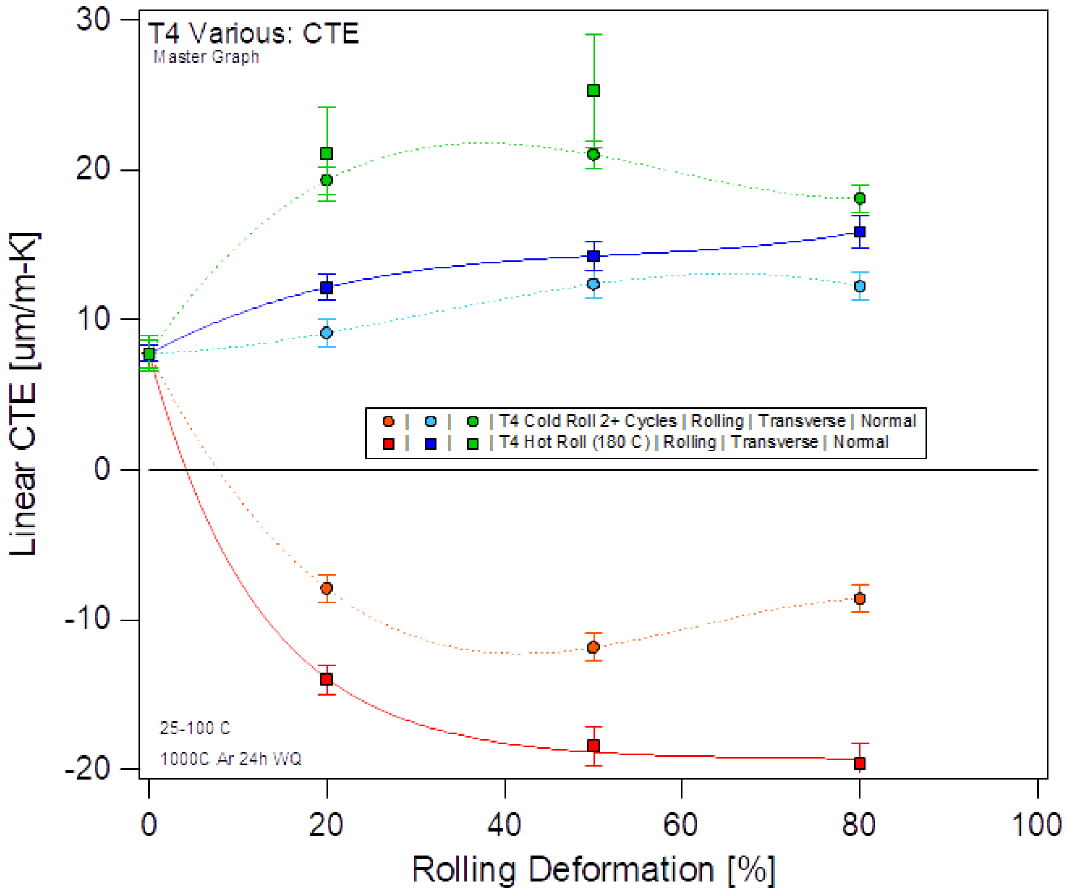

Figure 8.8 Comparison between the orthonormal CTE responses for cold rolled and warm rolled $TiNb_{22}$ alloy.

When comparing the linear average thermal expansion for the cold and hot-rolled cases, the overall thermal expansion anisotropy is highly enhanced by the hot rolling. This is especially visible for the rolling direction, where the overall maximum NTE increases from -10 to -20 in the same composition. This continues to the transverse and normal directions, where in both cases the CTE also increases somewhat compared to the cold-rolling case. Compared to the $TiNb_{20}$ case, the effect of the hot-rolling process is significantly less pronounced in $TiNb_{22}$, with there only being a small change in the CTE overall.

The most probable cause for this significant thermal response to higher-temperature deformation is due to the increased ease of variant reorientation and slip at elevated temperatures. This allows for a higher amount of orientation for a given deformation input due to the decreased resistance. The reduced benefit in $TiNb_{22}$ is due to the higher base reorientation response at room temperature, giving a smaller marginal improvement due to raising the rolling temperature. It is likely that such trends would continue for lower Nb content but raising the temperature of $TiNb_{15}$ material to 400 °C still failed to result in significant anisotropy. This illustrates that there are still limits to the effectiveness of this method. However, if hot rolling is available, it is clear that it offers an enhanced response by increasing the potential CTE anisotropy and removing the influence of the first-heating nonlinearity.

8.4 Inaccuracies of data estimation for rolling

Throughout this chapter, the estimation of the evolution in CTE over the course of deformation has been carried out using only four data points for each orthonormal direction – 0, 20, 50, and 80% rolling reduction. While the possibility exists that this density of data points is sufficient to accurately model the CTE change, the normal response to tension prestrain would indicate that this is unlikely to be the case. In the previous chapters the CTE changed rapidly in a small strain range which corresponded to the region of martensite variant reorientation being the primary deformation mode. To examine this potential error, additional rolling was performed in the TiNb20 material by rolling 4 additional samples to 2, 3, 5, and 10% total reductions. The rolling plane CTEs were measured via TMA and plotted against the previously gathered 20, 50, and 80% rolling reductions in Figure 8.9.

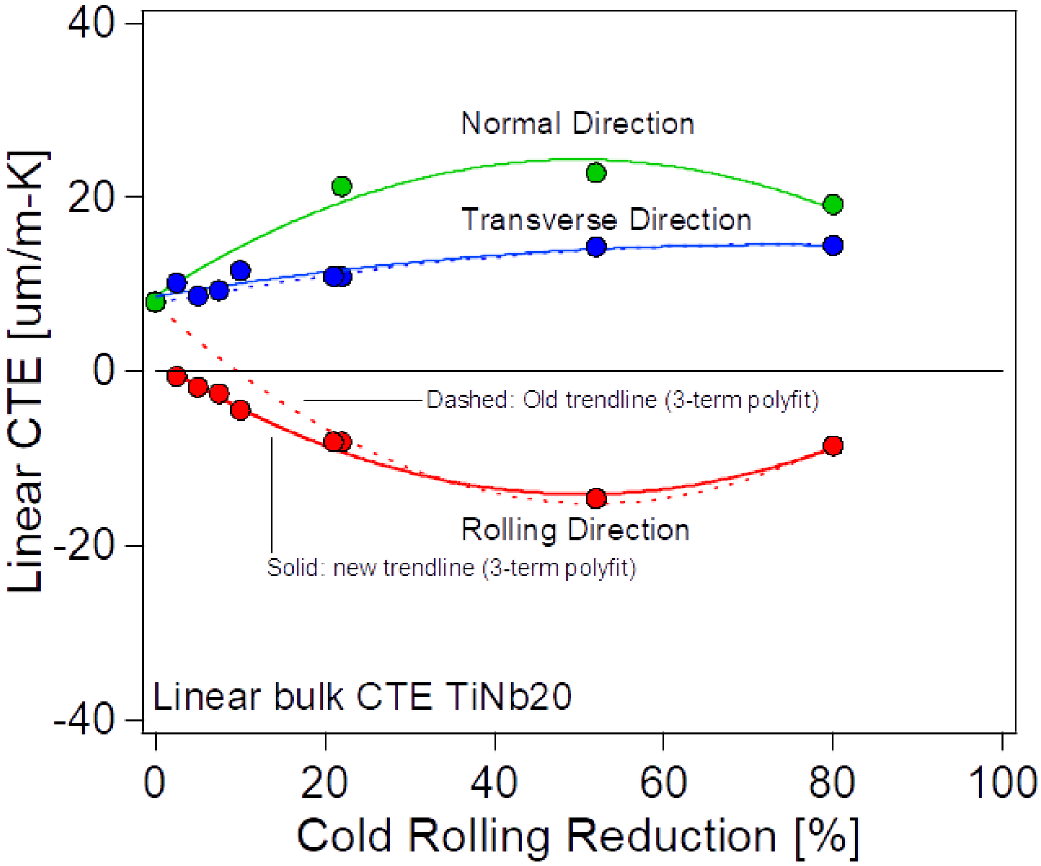

Figure 8.9 Illustration of the rolling direction mismatch based on inclusion of low-rolling deformation data in $TiNb_{20}$.

In this figure, the original 4-data point trendlines, estimated via a third-order (parabolic) polynomial fit are given as dashed lines for the rolling and transverse case, and solid for the normal direction (as this was not evaluated for these low-rolled samples). This is not the same trendline fit that was used in the orthonormal CTE demonstrated in 8.5(b) as this group of data was gathered in a separate batch of samples. Examined without the context of the less-rolled samples, it is clear why the logical conclusion would be that the CTE would change gradually before reaching the measured value at 20% reduction. However, addition of the new information clearly shows that for the rolling case this is not a valid conclusion. Indeed, the material instead evolves in a manner extremely like that of rolled NiTi, where much of the initial change in CTE for the rolling direction occurs over the very first few percent of rolling deformation. Interestingly, such a change is not present in the transverse case, where the additional data has a small effect on the overall estimation. This faster evolution likely extends to the normal direction, which often changes at a rate proportional to the rolling direction CTE. Overall, this indicates that the more rapid evolution in CTE outlined by both the tension and NiTi rolling data persists into the TiNb case, and that to fully model the change in CTE accurately for TiNb should require significantly more data below 20% rolling reduction than is seen in this study.

8.5 Temperature cycling effects on CTE response

Two phenomena in TiNb raise the question of long-term viability. Since TiNb is relatively inert and not subject to common corrosion, this question mainly is concerned with how affected by thermal cycling the CTE anisotropy will be. The first is the first-cycle strain change, which indicates a sensitivity to temperature in the material despite its isolation to the first application of heat. The second is TiNb's nature of being primary composed of a metastable phase in the conditions studied here. As such the possibility of decomposition to either the ω-phase or austenite may exist. Given that the ability for transformation can be induced by a number of aging factors, including thermal annealing of dislocations, spontaneous aging, excessive thermal energy, or gradual movement of interfaces due to fluctuations in the local strain fields, establishing whether there is any obvious susceptibility to thermal cycling is essential.

To that end, a preliminary study using methodology iii from Chapter III was applied to 50% rolled samples of both $TiNb_{20}$ and $TiNb_{22}$ alloys. For the 20% Nb alloy, the samples were subjected to heating of 150 °C for up to 1000 heat/cool cycles in total, while the 22% alloy was raised to only 100 °C in light of its reduced A_S temperature. Measurements of the CTE along various directions were made in TMA at specific intervals, namely after the first, 50th, 100th, 500th, and 1000th cycle of heating. The subsequent results of this work are summarized in Figure 8.10.

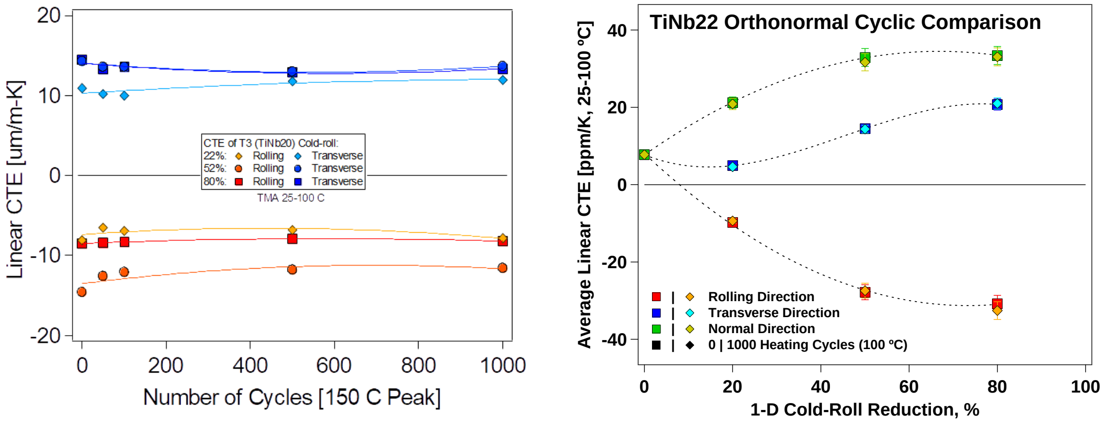

(a) **(b)**

Figure 8.10 (a) Illustration of cyclic testing response at various cold rolling amounts in $TiNb_{20}$ alloy. Illustrated are the rolling and transverse direction CTE for the 1st cycle as well as after the50th, 100th, 500th and 1000th heating cycles. (b) Examination of the 1st and 1000th cycle response in the orthonormal directions for $TiNb_{22}$ alloy.

In 8.10(a), the planar CTEs for $TiNb_{20}$ alloy rolled to 20, 50, and 80% rolling reduction are shown. While as usual the different CTEs for the different levels of deformation are visible, this is not the main concern here. When examining the change in linear average CTE over the course of cycling, it can be seen that on average there is a small (~2-3 ppm/K) change in the CTE over the first 50 cycles, followed by relative stability in the period following this. This holds true for all the rolling and transverse direction curves shown here. It appears to indicate that while a small adjustment will occur over the first few cycles, the material ultimately will settle rather than experience fatigue and revert to a more isotropic state within the first 1000 cycles.

This holding steady is further demonstrated for the TiNb22 alloy in Figure 8.10(b), where the average CTE for the first and 1000th cycle is compared in all the orthonormal directions. It can quickly be observed that in all cases, the deviation from the originally measured CTE is somewhat less than the experimental margin of error. This, when combined with the previous results in Figure 8.10(a), point towards a potential conclusion that overall, there is no transformation fatigue effect in rolled TiNb heated to below the observed A_S temperature. While this may have seemed tautological given that temperatures exceeding the transformation thresholds for TiNb were not reached in this study, the result was no self-evident due to the factors discussed above. It can be noted that in $TiNb_{20}$ there appears to be a larger displacement during the first 50 cycles before stabilization is achieved relative to $TiNb_{22}$. This is likely caused by the higher operating temperature which it was subjected to, which allowed for annealing of higher temperature dislocations which required more time to reach their tentative equilibrium.

8.6 Summary and Conclusions

In this chapter, TiNb binary alloy of compositions 15, 20, and 22 at% Nb were subjected to a rolling deformation treatment and the resulting CTE responses were examined to evaluate several criteria. The following was determined:

1. The martensitic CTE behaviors are in line with those observed in Chapter VI.
2. There exist multiple indicators which predict the loss of texturability as Nb content decreases, including yield stress, strain hardening, and lattice parameter mismatch.

3. The overall CTE anisotropy due to rolling is very large, allowing for creation of materials which have CTEs ranging from an isotropic 8 ppm/K to an anisotropic -30 to +30 ppm/K minimum in $TiNb_{22}$ along specific directions with application of 50% or more rolling reduction. This anisotropy does not persist through the entire range examined, with 15% Nb showing no significant bulk change in CTE.
4. Examination of the texture evolution shows that the CTE anisotropy is in good agreement with the orientation of the a- and b-axis for the crystalline martensite overall. The changes in texture with composition also agree with the indicators for reduced texturability observed previously.
5. Use of preheating or higher temperature rolling processes allows for the elimination of a distinct first-heating strain effect observed in rolled TiNb alloys, with a resulting loss of strain hysteresis due to the initial heating of the sample. In addition, rolling martensite at elevated temperatures is able to enhance the overall texturability of the TiNb material, enabling larger total CTE anisotropy at a more rapid evolution pace. This effect diminishes with increased Nb content.
6. Proper characterization of the incremental changes in CTE anisotropy with rolling reduction will require a more thorough approach below 20% rolling, as the evolution of the CTE is more rapid than was anticipated to be covered by the original 20, 50, and 80% rolling reduction references.
7. Examination of the overall CTE response to thermal cycling indicates that while the material remains below the transformation temperature threshold it can be remarkably stable.

CHAPTER IX

THERMAL EXPANSION ANISOTROPY AND OBSERVED ELINVAR EFFECT UNDER HIGH ROLLING CONDITIONS IN NICKEL-RICH NITI SHAPE MEMORY ALLOY

While examination up until this point has been exclusively focused on the characterization of alloys which demonstrate themselves to be wholly or nearly-wholly martensitic after thermomechanical heat treatment, it should be noted that martensite has been known to exist outside of the bulk military transformation in shape memory alloys. Although it remains a subject of debate as to what exactly the conditions are within the following metals, it has been postulated that in NiTi strain glasses [26, 28] and β-Ti GUM [27] metals there exists a 'frustrated' transformation in which extremely fine particles of martensite are located within the overall parent phase of austenite.

While this does in point of fact mean that the vast majority of the material is not martensitic, strain glasses and GUM metals show a number of similar properties that are not commonly known to occur within the confines of shape-memory alloys which are fully austenitic [26-28]. Most notably (and importantly) for this work, the martensitic particles interact with the surrounding matrix along their phase boundaries, leading to several temperature-dependent properties unique to this group of materials. Functionally, this 'frustration' of the transformation is analogous to an extreme form of martensitic stabilization, in which the conditions required for the formation and growth of the nanoparticles are persistent over an incredibly wide range of temperature, and equally small amounts of particle nucleation and growth/shrinkage are happening over the course of that same range.

In GUM metals, examination of rolled specimens where strain-glass like behaviors existed indicated that thermal expansion anisotropy could be achieved in this material as well. It is of high importance to this work that the proposed explanation as to why this may be occurring for the GUM metal is as being caused by the alignment of the martensite nanoparticles within the matrix as a response to the rolling deformation. If correct, this would indicate that the alignment of the martensite would have the same influence as switching, where the sign and magnitude of the lattice mismatch between the martensite and austenite would indicate the form of anisotropy created by the thermal excitations. Here, these thermal excitations most likely take the form of the growth and shrinkage of extant nanoparticles within the matrix, combined with the nucleation and destruction of new nanoparticles from the same matrix. This is due to the high concentration of dislocations and persistent strain fields present within the material, which both acts to prevent military transformation, as well as preserving a strain field favorable to oriented nucleation and/or growth in the sample as thermal conditions become more amenable to such. With such highly oriented material, the full difference in directional properties due to these lattice differences will occur at the phase boundaries as growth and shrinkage occur, potentially allowing for large strain and bond strength changes.

Compared to the TiNb binary material examined in the previous chapters, the typical compositions seen for many GUM metals are not significantly more alloyed, lending additional viability to the possibility of this postulated presence of martensite in these less-favorable conditions. As such, a logical extension to the examination of binary NiTi alloy would be to shift to a composition with transformation temperatures slightly below room temperature, thus allowing for the formation of a fully austenitic material that could easily accommodate higher levels of deformation than would be normally achieved via the cold-rolling of equiatomic martensite. By rolling to sufficiently high levels of deformation, it would therefore be possible to generate a sufficiently high dislocation density to achieve large local stress fields favorable to the formation of small, localized, and highly oriented martensitic cores which would then slowly shrink as temperature increased, allowing for the generation of matrix anisotropy in both thermal expansion and elastic properties as a result of the additional phase fraction and cohesion of austenite. Preparation of such material, with high rolling deformation amounts of 30, 40, and 52% rolling reduction was achieved, and these samples were tested via tension to verify whether this potential could be satisfied.

9.1 Observed crystal structure and calorimetry of nickel-rich NiTi

X-ray diffraction via Cu k-α radiation of the nickel-rich NiTi material at room temperature is shown in Figure 9.1. As-quenched, it can be observed that the two-theta curve is relatively disordered, with one main peak at approximately 42 degrees two-theta that is relatively broad, and a series of small broad peaks that are not only correct for pure BCC phase austenite. While it is possible that the source of these non-BCC peaks is noise, it may also indicate some small presence of martensite or the r-phase within the austenite matrix due to local conditions. Regardless, the as-quenched matrix is clearly not fully martensitic and appears to be relatively disordered in its overall configuration.

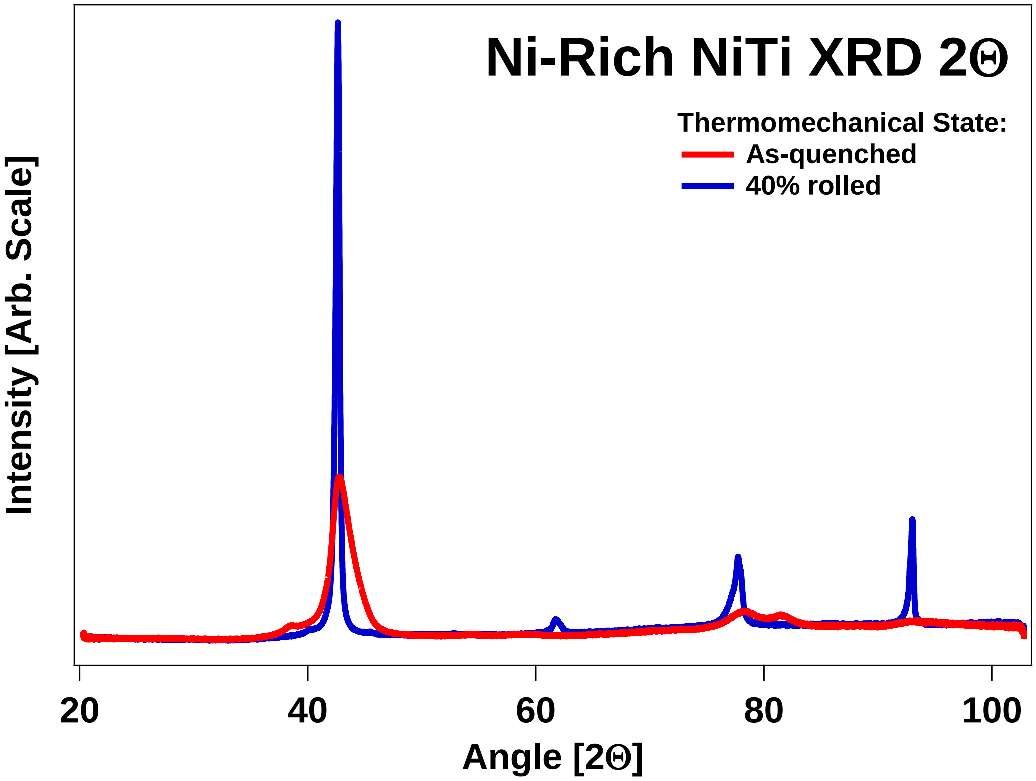

Figure 9.1 X-ray diffraction 2Θ results for various post-thermomechanical states of Ni-rich NiTi, including as-quenched and after 40% rolling.

This situation does not persist after rolling, here illustrated with the two-theta curve for the 40% rolled material which is here designated as being representative for the whole set of rolled material. In this situation, the BCC pattern expected for austenite can be clearly distinguished and there are no additional peaks which would be associated with other phases visible. In addition to this, the peak broadening has been significantly reduced, resulting in what appears to be a very strongly austenitic material with good ordering between the constituent grains. Such strongly austenitic results argue towards the correct conditions for potential strain glass behavior, and against the possibility that the primary result of rolling in these conditions was instead formation of the amorphous phase within the nickel-rich NiTi.

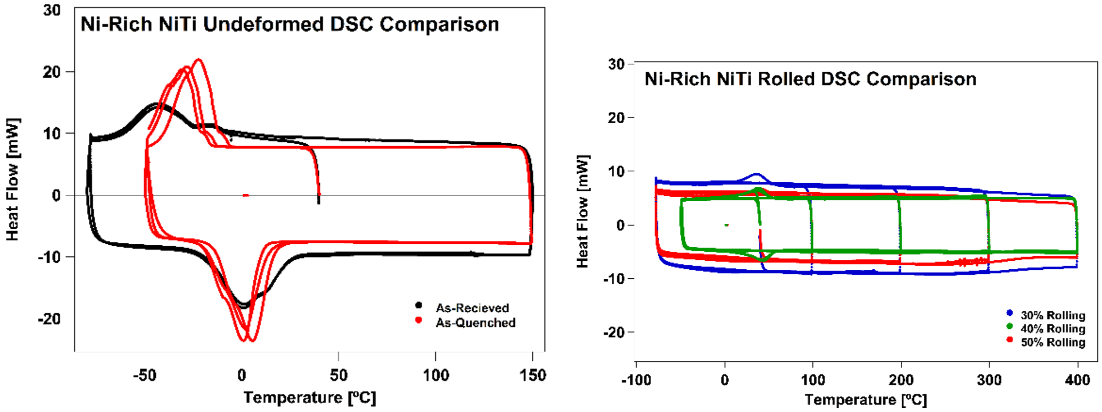

(a) **(b)**

Figure 9.2 DSC Examination of the Ni-rich NiTi. (a) Comparison of as-received and as-quenched undeformed material. (b) Comparison of the various 30, 40, and 52% rolling treatments after being applied to as-quenched material.

The underlying thermal transformation properties of this material are further examined in Figure 9.2, which demonstrates the DSC curves for the nickel-rich NiTi under different thermomechanical conditions. In 9.2(a), the as-received material demonstrates the following: A_S of -20 °C, A_F 40 °C, primary M_S of -10 °C, and primary M_F of -55 °C. The as-received material also possesses a secondary cooling peak at elevated temperatures relative to the primary, which may speak to some inhomogeneity due to manufacturing or previous processing. This contrasts with the calorimetry results observed within the as-quenched material used in this study, where the A_S is roughly the same but a smaller hysteresis region lowers the A_F to 30 °C with higher heat flow peak intensity during the transformation, while the M_S and M_F are shifted to -10 and -40 °C respectively with the same intensity increase. There is a small drop in the observed M_S, M_F, and A_F values after the first cycle, likely associated with the first heating effect documented earlier in NiTi. The effect of homogenization appears to have resulted in imposing a greater degree of uniformity regarding both the transformation and the reverse transformation. Relative to the equiatomic NiTi however, even this more ordered transformation results in heat flow peak values approximately half that seen in that previous case, possibly indicating a lower overall phase fraction transforms, or that it requires overcoming smaller energetic barriers.

The heat flow verses temperature for the rolled specimens is illustrated in Figure 9.2(b). Here it is plain that there is little, if any, obvious evidence of martensitic transformation. While there are peaks in 30 and 40% rolling, they are of extremely small magnitude, and in the 30% case only appear after the first cycle, likely indicating some degree of reverse transformation where thermal annealing of dislocations has permitted it. The gradual reduction and then disappearance of this peak as rolling amount increases indicates that the dislocation density increases to such a point that such annealing has a reduced effect in the region studied with higher rolling amounts. Considering the overall shape of the heat flow curves (quite bumpy and not flat as in a normal SMA DSC curve) and the relative strengths and locations of the peaks (all centered at approximately 50 °C), it appears that this material does not undergo bulk martensitic transformation.

However, it does appear to have some low-grade change in the material over the examined temperature range.

The information seen in Figures 9.1 and 9.2 are consistent with the behaviors observed in other strain glasses in literature. As a result, it seems reasonable to tentatively label the 30, 40, and 52% rolled $Ni_{50.3}Ti_{49.7}$ (at%) material as also being a strain glass.

9.2 Thermal expansion behaviors of rolled Ni-rich NiTi

The heating/cooling responses of previously unheated Ni-rich NiTi samples measured along the rolling direction in tension are shown in Figure 9.3(a). The first unusual behavioral quirk which can be noted in this dataset is the first-heating behavior. While it appears prototypical of the normal enhanced-strain response to heating, the magnitudes of the permanent strain change are opposed to the normal pattern seen in fully martensitic rolled metal – that is to say, rather than the largest permanent strain change being associated with the largest rolling amount as it is normally, instead the smallest strain change is attached to the largest rolling reduction of 52%. However, beyond this difference the rolling strain verses temperature curves appear remarkably like TMA and tension results for samples demonstrating NTE in martensitic alloys.

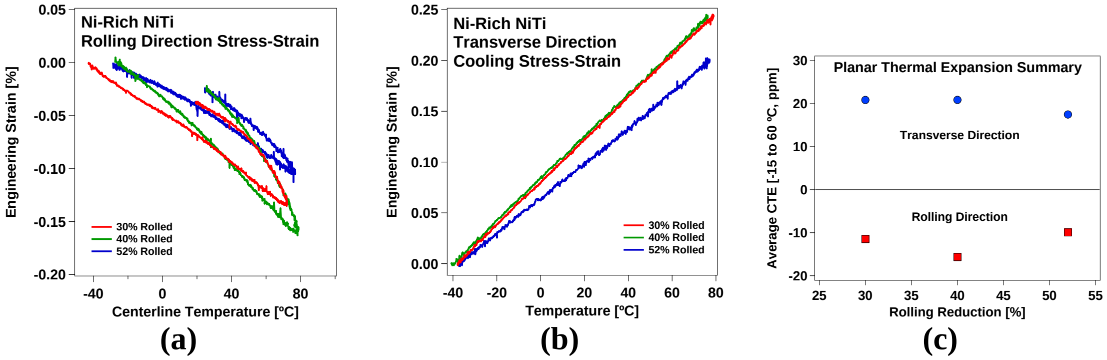

Figure 9.3 Thermal expansion anisotropy of Ni-rich NiTi. (a) Rolling direction strain plotted against temperature. (b) The same for Transverse orienatation. (c) Resultant CTE plotted against rolling reduction amount.

In cooling, it can be seen that the overall thermal expansion shows signs classic to the martensitic NTE. Very similarly to equiatomic NiTi, there is some nonlinearity above the 'M_F' temperature seen in both the as-quenched main peak and the smaller peaks in the rolled samples. Here, this increase appears very slight in comparison to the overall magnitude of the linear CTE and in contrast to equiatomic, with its existence most visible in the 52% rolling case. The 30% rolled sample has some significant nonlinearity not above the M_F temperature but rather below, possibly due to a lack of stabilization from dislocation density or experimental error. It can be observed that as a result of this, the highest overall NTE is seen in the 40% rolled case, and close examination of the higher-temperature portion of the cooling curve from 80 to 35 °C further implies that the 30% case does demonstrate somewhat less NTE than the 40% case were the nonlinear dip from 35 to -20 °C to be ignored.

In Figure 9.3(b), the transverse direction strain vs temperature results may be observed. Here, the 30% and 40% rolling amounts result in nearly identical overall CTE with particularly good linearity throughout the testing range, with a notable reduction in the overall CTE magnitude with the 52% rolling deformation. A summary of the linear average CTE measured from 60 to -15 °C is given in Figure 9.3(c). Here it should again be noted that the significant nonlinearity has some effect on the average CTE value for the 30% rolled case, and based on the visible strain verses temperature outside of the nonlinearity, it can be postulated that the NTE magnitude is slightly greater, although again still less than the 40% case. What is possibly of greater interest is that the NTE observed in all three cases is larger than the NTE seen in all conditions of NiTi save for the maximum NTE seen at the end of the variant reorientation stage of deformation, with the highest value (-16 ppmK^{-1}) being among the highest NTE seen in any NiTi-based material as a result of deformation tested in this work. Similarly, the transverse CTE measured in all three rolling conditions is notably higher than the CTE which had been measured in martensitic samples, indicating a higher overall anisotropy being achieved by this thermomechanical approach relative to the purely martensitic material in response to deformation. While it is irresponsible to assign trendlines to so few overall data points, it appears that this anisotropy peaks at the 40% rolling amount, with both lesser and greater amounts of rolling demonstrating either slightly reduced NTE in the rolling direction, or less overall CTE in both directions. This appears to indicate that there is a critical point for the beneficial effects of deformation upon this material system.

9.3 Elastic response to temperature in Ni-rich NiTi

9.3.1 Response under a limited temperature ceiling

When subjected to an even-interval elastic modulus test (of one cycle only) similar to the method used for NiTi using a similar temperature ceiling, the resulting stress-strain curves for the second elastic pulls at each temperature step are illustrated in Figure 9.4. In 9.4(a), it can be seen that when stressed to nearly 500 MPa, the 40% rolled material when examined in the rolling direction demonstrates a significant ‘straightening’ effect as the temperature increases. This has the effective result of raising the observed elastic modulus for the material in this direction as the temperature increases relative to the cooler temperature elastic curves. This same effect is also observable for the transverse case in Figure 9.4(b), although here the inversion of the sign for thermal expansion results in the curves for each temperature step appearing in the opposite order. Indeed, the effect is so strong in the rolling case that the apparent elastic hysteresis decreases as the temperature increases rather than grows larger as expected.

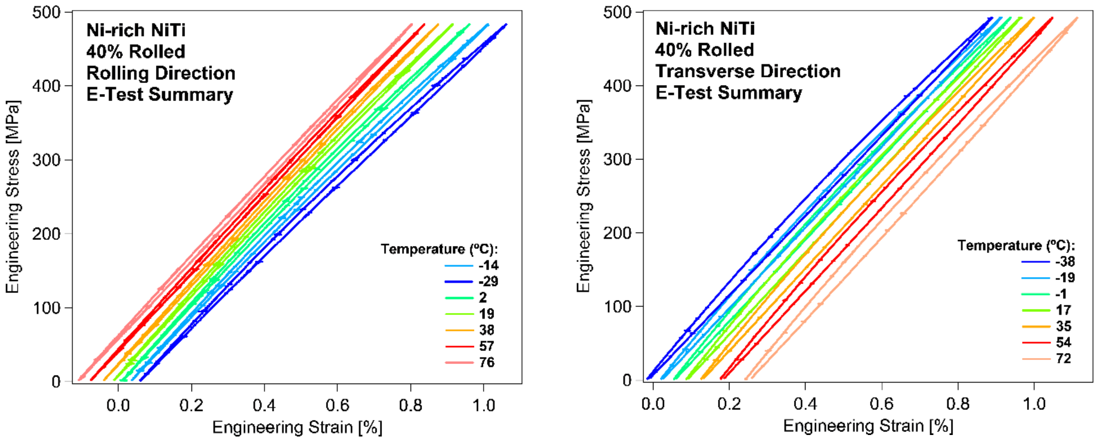

(a) (b)

Figure 9.4 Illustration of the thermal elastic cycle response in $Ni_{50.3}Ti$ after 40% rolling deformation.

The effect is more pronounced when viewed at higher stress limits, which was made possible here due to the large pre-straining applied to the samples via rolling relative to the undeformed NiTi which would not have elastic strength over 500 MPa until well into Region III deformation. For the purposes of evaluation however the 100 MPa upper bound used in NiTi is retained to allow for direct comparison of the two sample sets – in this lowered stress region, the straightening effect can be expected to be less pronounced, based upon visual examination of the lower-stress portion of the stress-strain curves in Figure 9.4.

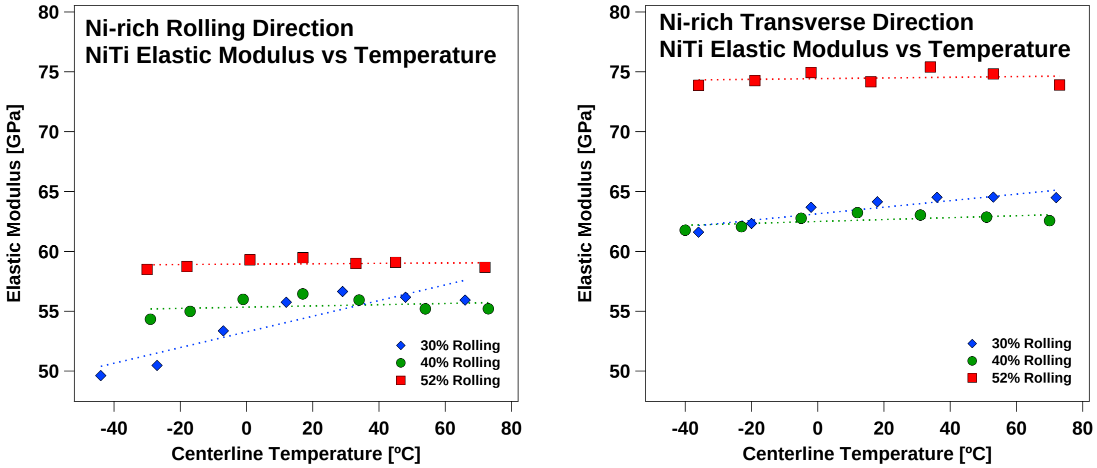

(a) (b)

Figure 9.5 Examination of NiTiPdTa elastic response to temperature. Engineering elastic modulus measured as an average of the loading and unloading steps in the cycles illustrated in Figure 9.4 compared as a function of temperature, deformation, and orientation.

In Figure 9.5, the results of the elastic pull to 100 MPa as a function of temperature are summarized for all rolling amounts. In the examination of the rolling direction shown in 9.5(a), the overall average elastic modulus increases with higher deformation amounts. It can be observed that as a function of temperature, the individual elastic moduli for a specific rolling treatment do not decrease as would be expected in a normal material. Instead, they appear to be nearly constant for 40 and 52% rolling, representing a potential Elinvar effect. In 30% rolling the elastic modulus values indeed do not simply hold constant but are rather increasing at quite a rapid rate, allowing for the elastic modulus to increase approximately 5 GPa in the range between -40 and 40 °C. This effect is not restricted to the rolling direction either, as Figure 9.5(b) shows. In the transverse direction the average elastic modulus again increases with rolling amount, with an apparent Elinvar effect seen in 40 and 52% rolling. In 30% the increase is notably less pronounced, as the elastic modulus only grows by approximately 2.5 GPa in the same temperature range.

When examining the response of elastic modulus to temperature in Ni-rich NiTi under heavy rolling reduction, there are significant new behaviors up to 80 °C. These are most likely caused by the shrinkage of martensite particles with increasing temperature as the effective reduction in the bond length with corresponding spring constant increase likely occurs at a rate proportional to the loss of stiffness in the surrounding austenite matrix. The induced orientation of the martensite particles is most likely the reason why this anisotropy can be observed in bulk material. In this temperature range, the lower dislocation density of 30% rolled material allows for a higher rate of interfacial change, which would enable a higher stiffening rate resulting from thermal excitations than the corresponding stiffness loss. However, to clarify whether this is likely to be an accurate explanation should require further examination at higher temperature to show whether any true transformation or other change in behavior may occur.

9.3.2 Determination of higher temperature targets and demonstration of response

To better understand the behaviors of the rolled Ni-rich NiTi material, it was first necessary to determine how the material behaved when subjected to temperatures well above the observed DSC transformation temperatures. The range up to 400 °C showed no other significant heat flow points in Figure 9.2(b), indicating no significant transformation localization. To verify this, one sample of 40% rolled material was placed into the tension machine and progressively heated in intervals to 400 °C as measured by the sample thermocouple. During this process, the heating would be interrupted at specific intervals to allow for elastic pulls after equilibration at those temperatures, as illustrated in Figure 9.6.

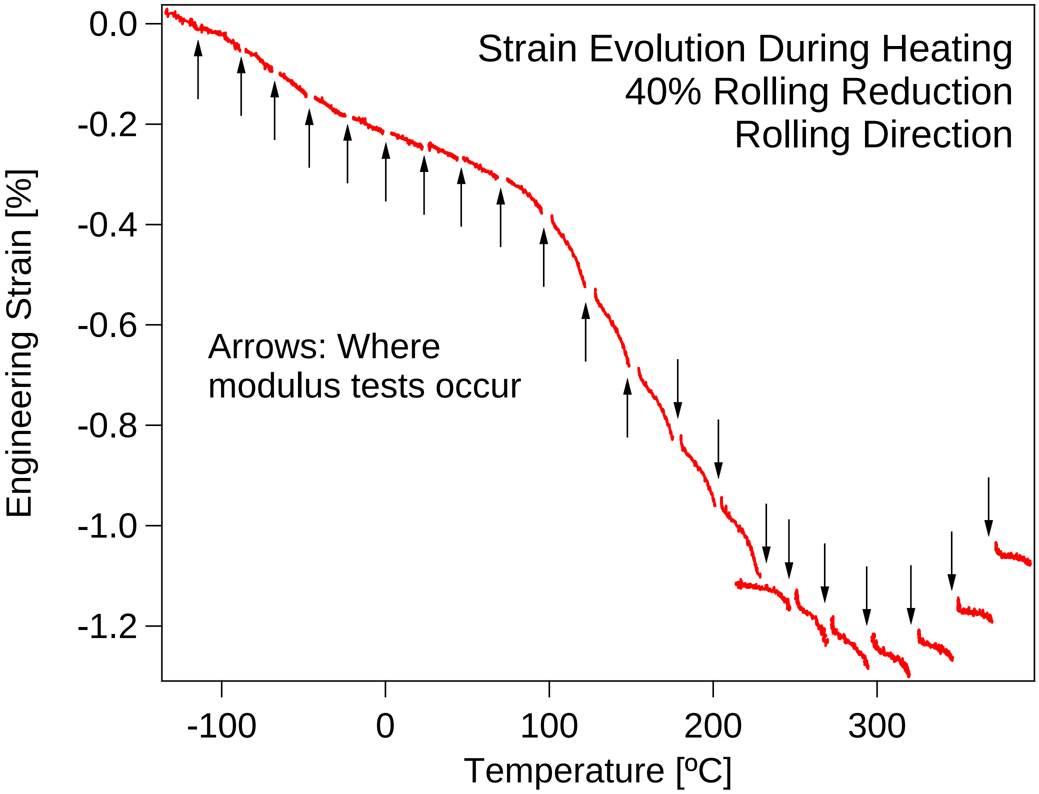

Figure 9.6 Engineering strain as a function of temperature for nickel-rich NiTi. 40% rolling reduction mounted in the rolling orientation during the course of its above-90 °C heating test. Large gaps between curves caused by additional thermomechanical response during the elastic loading after each heating step.

These pauses for testing also account for the breaks between data, and in some cases (above 230 °C) caused significant strain shift during the elastic preparatory pull due to what is probably a relaxation response within the sample at elevated temperature. When examining the sample strain against the heating temperature, there appears to be a region of constant behavior up to approximately 100 °C which corresponds with the region examined previously. This is followed by an unexpected significant negative strain resembling a traditional shape-memory strain response to bulk transformation, with a percent strain change (~0.9%) appropriate for a SMA with large hysteresis. Beyond 300 °C the strain response to heating has leveled out, and the strain change largely occurs instead due to elastic relaxation between heating intervals.

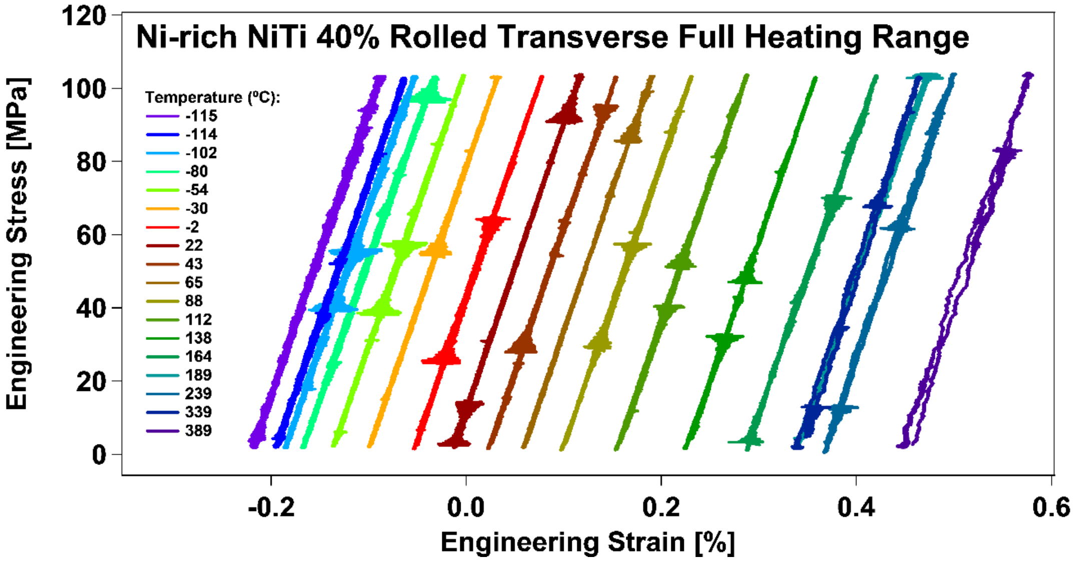

Figure 9.7 Stress-strain results for each temperature point in the full-range heating test of Ni-rich NiTi.

Based on 9.6 there appears to be some form of transformation-like behavior within the material. The overall curve most strongly reflects the strain curve seen in the rolling direction of rolled TiNb or NiTi when heated through its entire transformation process, consisting of the near-linear NTE followed by significant large negative strain change over a large temperature window. An explanation for this is not immediately clear due to the lack of significant amounts of the martensite phase. It is possible that thermal annealing of dislocations is allowing for significant strain change, but this most likely should be accompanied by some form of phase shift to reach such magnitude. Considering the high threshold of detection for subphases via Cu k-α XRD (~5% phase volume fraction), the possibility exists that the characterization of this alloy's constituent nanostructure is incomplete.

The arrows in Figure 9.6 illustrate all the temperature points during the one-way heating pathway where elastic modulus pulls occurred in this and similar tests. One of these is illustrated for the transverse direction of 40% rolled material in Figure 9.7. In this, the consistency of the elastic behavior can be seen. The slope of the stress-strain can be observed to have shifted slightly over the course of heating from -115 to 389 °C, with the apparent stiffness of the latter case being somewhat higher. Until crossing beyond 230 °C, the individual loading and unloading curves are in good agreement with little if any observable elastic hysteresis. Beyond this temperature this is reduced somewhat as the high-temperature relaxation results in the small separation between the two curves. It is of interest that this process occurs only at the conclusion of the large strain deflection observed in Figure 9.6, and likely points to some interrelation between them. Nonetheless, it is clear that over a 500 °C there is a small change in the overall elastic behavior of the sample as it is being heated.

9.3.3 Overall stiffness-temperature response and high-temperature Elinvar effect in $Ni_{50.3}Ti$

The measured elastic moduli as a function of temperature when subjected to the 400 °C maximum are given in Figure 9.8(a) for material in the rolling direction, and in Figure 9.8(b) for the transverse.

In the rolling direction there is a real Elinvar effect between -100 and 100 °C in 52% rolled material. 30 and 40% rolled material also show either average net zero change over a specific temperature range or an overall increase in stiffness in this same range. For all three rolling treatments, a rapid increase in the stiffness began after exceeding 100 °C in the sample continuing until the sample reached 350 °C. The peak stiffness in 40% and 52% rolled material at that high temperature corresponds strongly with the approximate range of stiffness typical for the austenite phase in NiTi. The overall stiffness behavior appears to correspond strongly with a two-mechanism model, where a process similar to switching dominates at lower temperatures before giving way to a transformation mechanism which takes place until the material is fully austenitic.

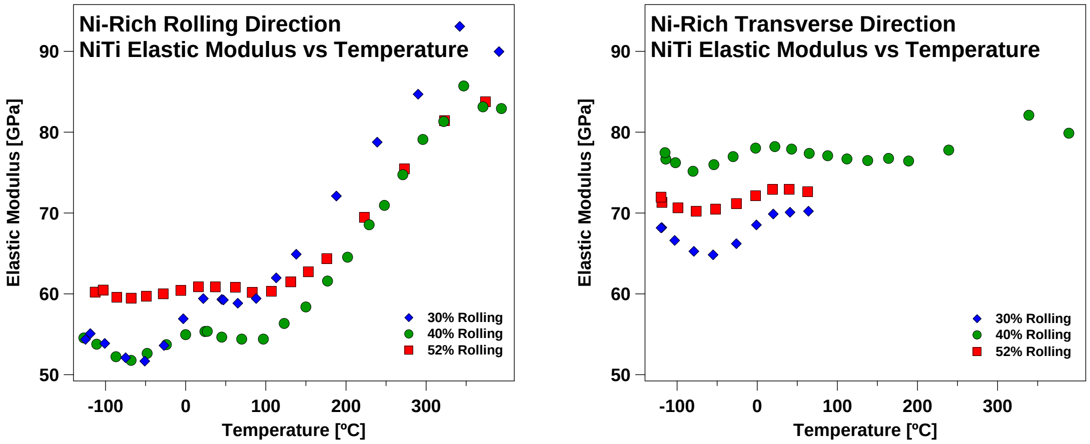

(a) **(b)**

Figure 9.8 Elastic modulus for nickel-rich NiTi as a function of temperature, deformation level, and orientation for continuously increasing heating. (a) all three rolling reductions and both orientations considered (b) 40% rolling reduction alone.

The two-mode mechanism supported by the rolling-direction data is however contradicted by the transverse direction summary. Here average elastic modulus for all rolling amounts is already significantly greater than it was in the rolling direction, which is to be expected given the reduced lattice mismatch between the PTE orientations and the BCC matrix. However, of greater interest is the apparent lack of any transformation mechanism onset until approaching the same 300-350 °C temperature that represents the end of the transformation phase in the rolling direction. The net effect of this is the persistence of the room-temperature level elastic modulus up to a significantly higher temperature, with the 40% rolled material demonstrating an apparent net Elinvar effect in the entire temperature range from -100 to 250 °C.

Why this disparity may exist between the two directions is unknown, but it clearly points to a strong disparity in directional response to temperature within the same material. Certainly, further investigation would be required to determine and isolate all the factors behind this difference in behavior. Regardless of the unknowns in the underlying mechanic however, the existence of an observed Elinvar effect up to 250 °C is extremely significant, as it exceeds the previously known highest temperature of an Elinvar alloy by almost 125 °C. Between this and the significant CTE anisotropy extant in this rolled material, this highlights a truly powerful alternative approach to the fully martensitic alloys studied in the prior chapters.

9.4 Summary and Conclusions

In this chapter a nickel-rich $Ni_{50.3}Ti$ (at%) alloy was studied to determine whether manipulation of a less-martensitic material via dislocations and boundary interactions may provide an alternative methodology with desirable properties. After examination via XRD, DSC, and tension testing, the following conclusions were reached:

1. Rolling deformation of a non-martensitic material is still capable of producing significant CTE anisotropy, with the 40% rolled case for this material exceeding the thermal expansion achieved by rolled equiatomic NiTi while presenting significantly higher transverse CTE.
2. The rolling deformation, based on the XRD and DSC information gathered, demonstrates characteristics most strongly associated with strain glass alloys. This is contradicted by its strain responses at higher temperatures, where significant strain change occurs without a corresponding heat flow peak. This

may point to a higher percentage of stress-induced martensite than assumed which played a role at sufficiently high temperature, or additional mechanism currently unknown.

3. In addition to the significant CTE anisotropy, rolled Ni-rich NiTi also demonstrates net elastically invariant behavior as temperature increases. The transverse case in 40% rolled material retained its Elinvar characteristic to 250 °C, which is significantly higher than other known Elinvar alloys.
4. Further examination and characterization is required to gain a full understanding of the potential demonstrated in this study.

CHAPTER X

SUMMARY, MAIN CONCLUSIONS, AND FUTURE DIRECTIONS

Various aspects of the thermal anisotropy in the NiTi, NiTiPd, and TiNb alloy systems were investigated. Over the course of this study the crystalline thermal expansion anisotropy, bulk thermal expansion, and bulk stiffness responses were examined for various thermomechanical approaches to determine whether the multiple scales of anisotropy were intrinsically linked via their deformation texture.

Examination of the equiatomic NiTi martensite revealed a large thermal expansion anisotropy in the B19’ monoclinic crystal that resulted in a large positive thermal expansion along the [010] crystalline direction, with a nearly equal negative thermal expansion moment that lay along an axis determined by the interactions of the beta angle with the a- and c-axis thermal expansions. Study of the deformation effect upon NiTi showed that for the crystalline lattice expansion the overall effect was minimal until after passing out of the region of detwinning and variant reorientation response to deformation into slip plasticity, upon which there would be a notable decrease in crystalline thermal expansion anisotropy. Bulk thermal expansion measurements along the tension direction indicated that the CTE evolved in a similar manner where it would decrease rapidly throughout the reorientation phase to a minimum average linear CTE of -18 ppm K^{-1} over a 75 °C temperature window. Passing beyond the area of variant reorientation would result in a gradual reduction in maximum NTE magnitude until fracture. These results conformed well with the observed texture evolution. Examination of the elastic modulus response to deformation along the tension axis further revealed that orientation texture showed a small effect on the room-temperature stiffness, but the slope of the stiffness-temperature response to deformation decreased radically as reorientation texture was applied. This was followed by a continued monotonic decrease in the stiffness change as a result of temperature, indicating that additional effects further change the stiffness-temperature relationship in texture NiTi during plastic slip.

Measurement of a $NiTi_{49.5}Pd_{25}Ta_{0.5}$ alloy showed that the alloying content increase led to a shift into the B19 orthorhombic martensite phase, with an accompanying shift towards an orthonormal crystalline CTE response with the b-axis representing the axis of NTE, the a-axis the orientation of large PTE, and the c-axis possessing a small PTE magnitude. Despite this, the overall crystalline thermal expansion anisotropy remained similar to NiTi. Examination of the resulting tension CTE showed a slow linear decrease in CTE under reaching a maximum NTE of -5 ppm K^{-1} before fracture. The limitation of CTE is caused by the low accommodation of slip in the NiTiPd system as the sample would fracture upon reaching the limit of detwinning stress in this material. Examination of elastic properties in the material showed a significant rapid decrease in the stiffness-temperature relationship due to martensite orientation, with stiffness at 5% prestrain softening only -30 MPa/K. This high level of thermal stability in the sample is attributed to the extremely strong and symmetric PdTi bond stabilizing the material.

Measurement of crystalline lattice expansion in TiNb demonstrated a small effect on the crystalline thermal expansion anisotropy as the total deformation increased. In addition, TiNb demonstrated a significant temperature effect on the CTE where the slope of the (020) NTE and (200) PTE were continuously changing as the temperature increased/decreased, likely due to the ease of sampling and this sampling rate being changed by the availability of excess thermal energy as temperature increased. Comparison of composition showed an inverse CTE anisotropy/maximum working temperature relationship, where higher expected A_S temperatures likewise were in alloys that demonstrated smaller overall CTE anisotropy rates, although the overall strain change generated over a temperature range from -170 °C to the maximum working temperature was more similar. Examination of the CTE resulting from tension deformation resulted in a compositionally-dependent rate of CTE evolution, where the high-temperature $TiNb_{15}$ (at%) showed no change in bulk CTE while the maximum NTE increased significantly as Nb content in the alloy increased. The rate of change of the CTE as a function of deformation also evolved radically, with $TiNb_{20}$ alloy showing an initial decrease followed by a small gradual change and more constant rate of CTE change in $TiNb_{22}$. This contrasted with $TiNb_{24}$ alloy which demonstrated extremely swift reorientation of the material in the first 5% of plastic strain followed by relatively little change during subsequent deformation. Examination of texture showed good correlation between crystalline alignment and bulk CTE, with texture orientation proving capable of predicting CTE magnitude and direction of bulk TiNb samples.

Examination of the orthonormal CTE in NiTi as a response to rolling deformation revealed that the CTE evolves radically along the rolling and normal directions with magnitudes of each peaking at approximately 5% rolling reduction. Conversion to effective tension strain values illustrates good agreement between the tension-axis NTE evolution and the rolling CTE change along the rolling axis. Severe plastic strain in the NiTi showed unexpected increases in the CTE after the gradual reduction in CTE anisotropy which indicates additional effects may be coming into play in the SPS region. Heating samples to the stabilized martensite temperatures revealed in DSC showed that some reversible martensitic transformation occurs in these samples during thermal cycling, with the effect of enhancing the net CTE.

Application of rolling to TiNb alloy showed that the orthonormal CTE evolves to become extremely anisotropic for compositions $TiNb_{20}$ and $TiNb_{22}$, with no net CTE change occurring in $TiNb_{15}$. This occurs despite the retention of CTE anisotropy in the crystalline $TiNb_{15}$ and points towards limitations in the reorientation capabilities of the different compositions being of tantamount importance in determining the achievable CTE anisotropy. The availability of detwinning pathways in TiNb is determined by composition and temperature considerations, the latter of which is made clear when comparing low-temperature and high-temperature resultant rolling CTE in $TiNb_{20}$ alloy. The application of higher temperature appears to be most significant on compositions where the reorientation is partly reduced rather than prevented entirely at room temperature. Preliminary examination of thermal cycling responses indicate that the

TiNb alloy is not significantly prone to thermal expansion fatigue when heated below the A_S temperature.

Examination of nickel-rich $Ni_{50.3}Ti$ alloy showed what appeared to be a strain glass material which became more strongly austenitic with application of rolling deformation. Examination of these deformed samples demonstrated large planar CTE anisotropy, with NTE on par with the maximum NTE observed in equiatomic NiTi alloys. Elastic modulus measurements revealed both a significant directional modulus discrepancy and a tendency to increase the stiffness as temperature increased, with net elinvar behaviors reported for rolling reductions between 30 and 52%. This elinvar behavior would be very robust, persisting until 100 °C generally and up to 300 °C in the 40% rolled transverse directional example. The directional nature of the anisotropy for both properties indicates that the orientation of the martensitic nanoparticles has a significant overall influence on the behavior of strain glass and may point towards a more unified model for strain glass mechanics.

10.1 Future Work and Directions Overview

The results discussed in the previous chapters leave a number of clear routes for additional study. While the general linear deformation response of the TiNb, NiTi, and NiTiPdTa material in regard to CTE and stiffness is well established in this work, three routes of further experimental investigation have been identified:

1. Examination of the viability for using directional cutting at a given deformation amount instead of deformation amount in a direction as a controlling variable.

2. Using temperature as a parameter for further tuning the CTE or elastic stiffness response in a material, taking advantage of the large transformation hysteresis provided by large deformations.
3. The possibility of generating an approximately uniform 2-dimensional (planar) thermal expansion, as well as other two-dimensional CTE configurations.

The first two areas of interest are tied to the design of alloys by way of optimization in highly deformed material. In each of these areas some preliminary work has been completed, offering a window as to what may be possible and providing some guidance as to further investigation in order to glean a systemic understanding tied to each objective. The results of these preliminary studies, as well as thoughts as to how to approach each problem, are given below.

10.2 Directional cutting of highly rolled SMA

One behavior clearly established throughout this work is that under large deformation, the material will evolve to show a large peak CTE in the transverse orientation, and a large NTE oriented with the rolling direction. As this anisotropy results from the texture of the sample, examination of the textures has indicated that both orientations are, on average, the peak values that are seen in the sample. Accordingly, it can be expected that if the rolling plane (containing the rolling and transverse axes oriented at 90° relative to each other) were to be examined at angles other than the principle axes, then values of CTE between the two peaks should be measured. This has already been shown for highly rolled NiTi by Ahadi *et al*. [16], where the CTE between the rolling and transverse orientation evolved in a pseudo-linear fashion, where the thermal expansion was approximately zero between 35 and 45 degrees orientation relative to the rolling direction.

There are several reasons to prefer cutting at an orientation in a pre-deformed sample rather than tailor the deformation to achieve the intended CTE as explored in this work. One is that many of the likely desirable CTE values in the rolling direction, such as invar and other small positive and negative CTE values, all tend to occur in a narrow range of deformation in both NiTi and TiNb, making it very sensitive to the precise amount of deformation applied to the sample. Additionally, there exists the possibility for a non-insignificant amount of variance to occur in separate parts because of the pseudo-randomness of the self-accommodated martensite generated during the quench. Especially when the target deformation may only be 1 or 2% in total, such influence on the ease or lack thereof in variant reorientation may have a significant effect on the exact CTE which results. Much higher deformation values to well beyond the region where the majority of variant reorientation occurs would result in higher consistency, as many of these causes for variance would have been fully worked out. As was seen in previous chapters, rolling to much higher reductions will also allow for the possibility of leveraging martensite stabilization and allow for higher operating temperatures. Taking these factors into account, using cutting orientation instead of deformation amount is the better option. When the higher ease of use (due to always having the same thermomechanical preparation route) is taken into consideration, this is most likely the optimal pathway by which to introduce this technology into industrial usage.

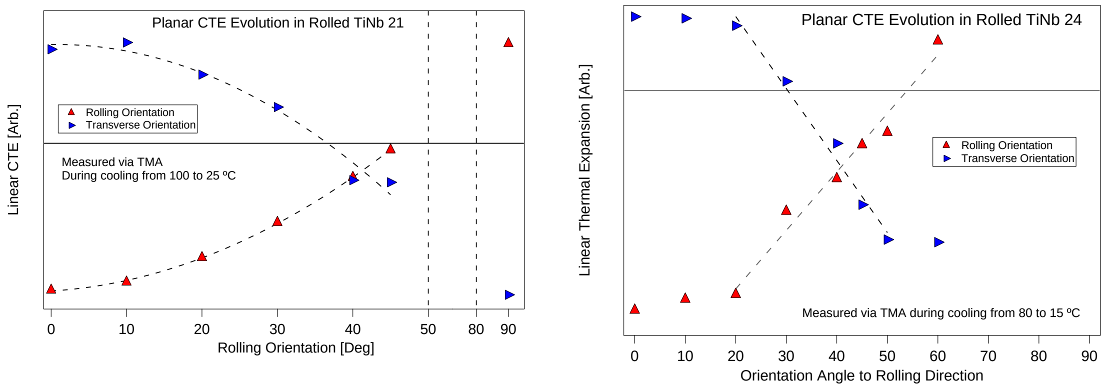

(a) **(b)**

Figure 10.1 Preliminary examinations of CTE-orientation relationship for highly rolled TiNb. (a)TiNb$_{21}$ (b)TiNb$_{24}$

While the planar response in NiTi had been previously established, whether this same sort of linear decline also occurred in TiNb was not known and so I undertook a small proof of concept study. Figure 11.1 shows the results of this preliminary work where TMA samples were cut from 50% cold rolled strips of TiNb$_{21}$ and TiNb$_{24}$ alloys at 10° orientation steps, and the resulting CTE in these directions was measured. Because of a lack of immediate need this study was abandoned with only about half the total orientations measured, which is the cause for the missing data between 50° and 90°. What is here is still believed valid as many of the remaining results were expected to be mirrors of the already gathered data, similar to the 90° orientation in TiNb$_{21}$ compared to the 0° orientation. Ultimately figures G-1a and G-1b both indicate an increase in CTE from the minimum found in the rolling direction until reaching its maximum in the transverse, although the modes of this change are not identical. In 21% Nb alloy, the mode of the change is a gradual pseudo-sinusoidal curve where the change in CTE appears to begin almost immediately after moving out of the exact rolling orientation. This contrasts with the 24% Nb alloy where the change in CTE is a delayed linear curve which begins after the CTE was relatively plateaued within an approximately 40° cone centered at the principle axes. This points to a distinct contrast caused by the texturability in the two metals – the TiNb24 as previously seen is easily capable of being worked to high texture in short amounts of deformation, resulting in a broader distribution of this orientation over time.

This points to the main area where further work would need to be concentrated: in examining enough compositions and samples to determine the general shape of the resulting CTE as a function of orientation, and how the different levels of texturability compare in terms of their orientation effects. Further examination, and ultimately industrial calibration should this method be exported, could easily be accomplished by examination of the surface via digital image correlation (DIC) as the samples are thermally cycled. This will allow for quickly capturing the change in strain with temperature in all directions of the sample with good accuracy, although some work would need to be done to verify how accurate surface measurements such as DIC are when compared to bulk measurements like TMA.

Ultimately, use of orientation to tailor the CTE is an exciting method, and much promise can be seen in pursuing further examination of this topic.

10.3 Over-temperature of the material to tailor expansion and stiffness response

One effect of large deformations in SMA is to make the transformation temperature range extremely large, even if it does not result in raising the A_S temperature via martensite stabilization. The direct effect when martensite is deformed is a significant increase in the A_F temperature, making it so that the transformation can occur over a large temperature range. It is possible to manipulate this large temperature range because of the athermal nature of martensitic transformations. If it can be assumed that the deformation result in nearly identical transformation responses, which is likely nearly true when highly deformed, then it is possible to consistently transform a specific fraction of the material permanently by heating to a specific temperature. The advantage of doing so lies in the large anisotropy of the material – many common applications will not require NTE magnitudes as high as was observed in, for example, 50% cold rolled TiNb22. As a result, by raising the temperature of the material above its AS temperature and reducing the volume fraction of the martensite, the amount of material available for switching is reduced and thus the overall NTE magnitude can be lowered, potentially to the exact value desired with sufficient understanding. The additional benefit of this method for tailoring the CTE is once again due to the athermal nature of the transformation: after having increased the part’s exposed temperature, it can now in theory be worked up to this temperature without any further change in its CTE, raising its maximum operational temperature. This offers yet another powerful way to both tailor and further optimize the CTE behavior of SMA materials.

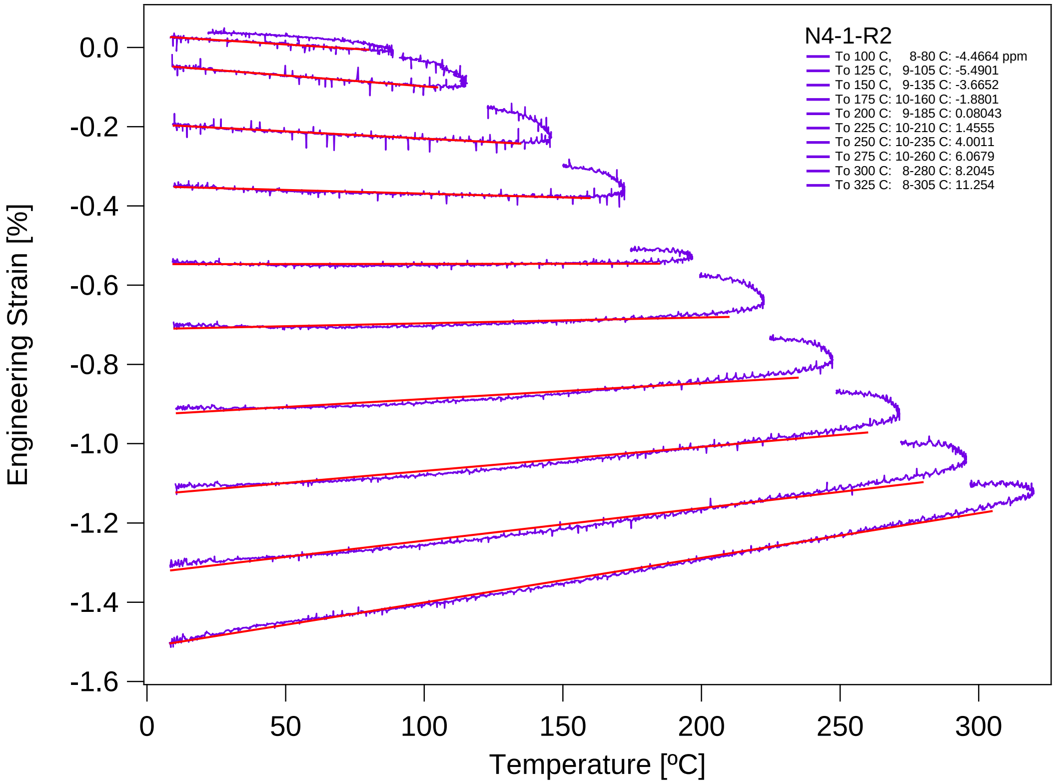

Figure 10.2 Stepwise heating effects on expansion properties illustrated via nickel-rich NiTi rolling 52% in the rolling orientation. Strain response for heating and subsequent cooling of the sample to new maximum temperature limits.

To examine the viability of this concept, two preliminary studies were carried out in 52% rolled $Ni_{50.3}Ti$ and in 50% rolled $TiNb_{21}$ alloy. Figure 11.2 illustrates the strain verses temperature for the stepwise heating pathway and cooling curves as the sample was heated from 100 °C maximum achieved (sample) temperature to 325°C maximum achieved temperature. The overall strain change over the course of the stepwise heating resembles the strain change seen in the heating of Ni-rich alloy in the previous chapters and appears to proceed in a linear fashion through much of the temperature range. Of great interest is the cooling curves, which by comparison with the overlaid linear fit curves can be easily seen to be largely linear in their strain change. The CTE values of these cooling curves averaged over their entire length is given in 11.3(a). The apparent effect as the temperature is increased and (in this ‘strain glass’ case) dislocations are annealed is to create a linear reduction of the NTE until it crosses to PTE, culminating in a PTE value at maximum temperature similar to the volumetric expansion of the material when undeformed. Of particular note is the 200 °C heating case, which gives an exactly invar slope for CTE and continues to do so up to 200 °C – 75 °C higher than Invar alloy and significantly higher than the highest temperature in rolled NiTi.

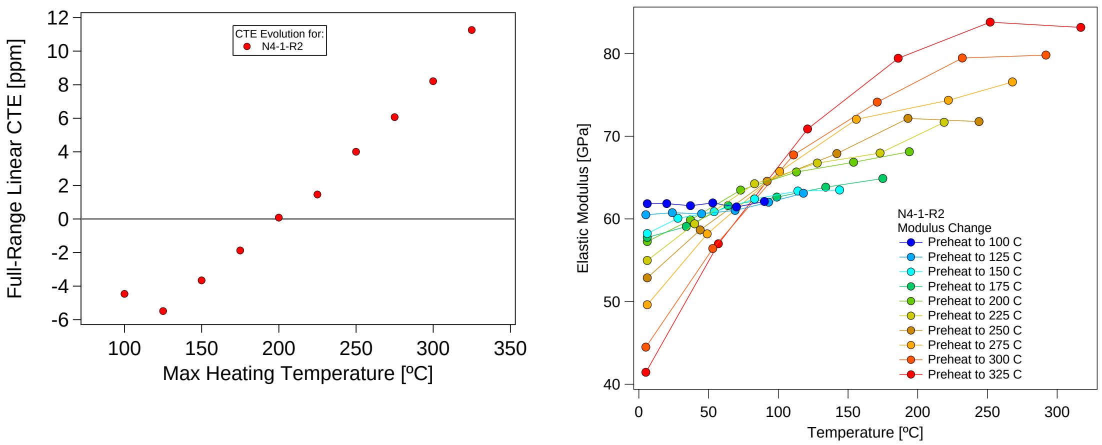

(a) **(b)**

Figure 10.3 Stepwise heating effects on various properties illustrated via nickel-rich NiTi rolling 52% in the rolling orientation. (a) Linear CTE resulting from 0 °C to the maximum heating temperature for each target heating level. (c) Stepwise elastic modulus measured during the return heating after cooling to the previous temperature maximum.

In this same test the stiffness of the sample was measured as it was reheated to its previous maximum heating temperature in the same manner as has been done in previous chapters. The results are given in Figure 11.3(b) and show that the stiffness as a function of temperature evolves radically as the temperature limits are raised. When heated to 100 °C maximum the Elinvar behavior previously reported once again is seen, but as the temperature limit is raised, the slope of the stiffness change in the material becomes progressively more positive. This culminates at the 325 maximum heating temperature case, where the elastic modulus ranges from 41 GPa at 0°C to 85 GPa at 275 °C, for an average stiffness change of +160 MPa/K. This once again is likely due to the thermal annealing. As more dislocations are destroyed, a larger percentage of the material can transform to martensite as the temperature is decreased, and vice versa. This results in a large percentage of highly oriented martensite at low temperatures in the most heated cases with a correspondingly low elastic modulus, and a more complete conversion to austenite at high temperatures with the correspondingly high modulus. This author is not knowledgeable of any other material which demonstrates a doubling in stiffness as it is heated over nearly 300 degrees, nor of any immediate applicational use. However, it is exciting in its uniqueness.

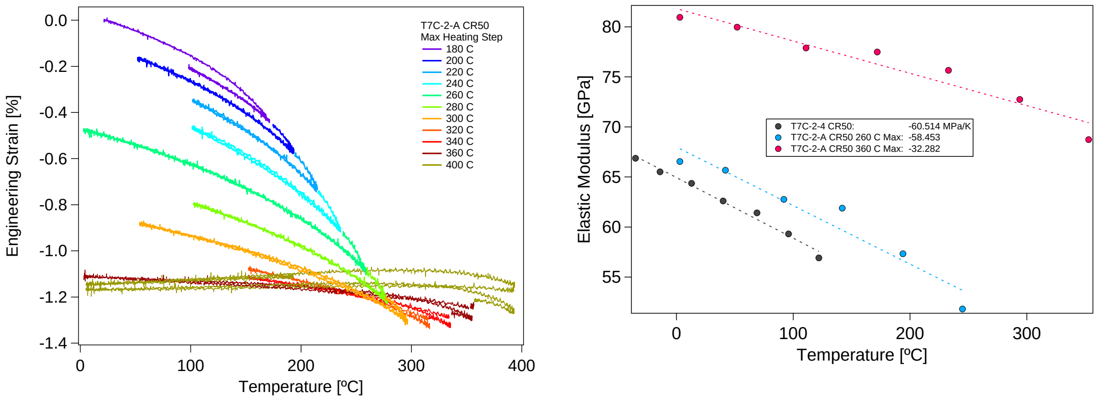

(a) **(b)**

Figure 10.4 The same stepwise heating approach illustrated by preliminary results in 50% cold rolled $TiNb_{21}$. (a) Strain response to temperature as the sample is heated to its new maximum temperature and subsequently cooled to capture the CTE. (b) Stepwise elastic modulus captured on the three cycles where it was attempted in this test.

The results of the second study in $TiNb_{21}$ are shown in Figure 11.4. Here again it can be seen that as the transformation is triggered and increased, the corresponding NTE of the cooling curve decreases. In this particular study it proved difficult to reach full transformation as the CTE is still close to 0 rather than positive even after heating by approximately 75 °C above the apparent A_F temperature based on the strain response. However, it does result in a heating/cooling curve after the 400 °C heating case with a net CTE very close to zero and a maximum operational temperature almost 275 °C higher than seen in Invar alloys. It is clear that the partial transformation results in some odd effects on the properties as seen in Figure 11.4(b). Here, three examinations of the stiffness as a function of temperature show that the base elastic modulus increases as the maximum temperature is raised (likely reflecting the increased austenite fraction), but at the same time the rate of change in the stiffness is also reduced, especially near the apparent A_S temperature relative to before transformation. This is significant, as it was shown previously that deformation-based attempts at manipulation of the elastic modulus in TiNb were generally middling or unsuccessful. It points to additional interactions in the material as a result of partial transformation and merits further study.

Ultimately while these two studies appear to prove that there is veracity to the concept of a temperature-driven partial transformation for the purposes of tailoring CTE, there are several additional questions raised by these results regarding the interaction of stiffness as a consequence of this heat treatment. On the whole, characterization and calibration of the material response to this above-A_S approach requires study of significantly more samples to examine not only if the preliminary results are prototypical for their particular materials, but also the effects of deformation amount, composition, and sample-to-sample variance. The next natural step is to examine a lower-temperature TiNb alloy such as 24% Nb, as well as highly cold rolled (>25%) NiTi, both of which were in preparation earlier this year.

10.4 Towards generating two-dimensional tailored thermal expansion

The large anisotropy which emerges because of linear deformation allows for high degrees of manipulation towards a desired, tailored value. However, it should be admitted that in many engineering applications the parts being used will require CTE which is isotropic either in two or three dimensions. Because the volume thermal expansion average is conserved, it is not possible to fully manipulate the 3-D CTE of these alloys without at least one direction having a quite different output value.

However, it should be entirely possible to generate a more uniform two-dimensional CTE response in alloys such as TiNb by varying the direction of the applied stress during deformation. The objective would be to generate an average texture which mixes the various anisotropy texture modes normally separated in linear deformation. The obvious approach for creating a planar response would be application of a uniform tension stress across the entire plane of the sample; however, as this is not a technique available here the closest simulacrum possible should be investigated.

This closest identified method was the application of ‘clock rolling,’ or rotation of the rolling axis. In a preliminary study, samples were assigned two axes of rolling: direction A in the usual rolling orientation, and direction B along what would be the linear transverse axis. To roll this material, 4 rolling directions were marked at 0, 90, 180, and 270 degrees orientation, and rolling was conducted by rotating 90 degrees after each rolling step, with the same <0.005” separation decrease between the rollers as applied in the linear TiNb rolling process. The advantage of this approach is to iterate small relative amounts of rolling deformation in each step, resulting in iterated small deformation amounts in both principle axes with ideally similar deformation responses. Two samples in $TiNb_{20}$ were produced using this method to 25 and 30% rolling deformation and their two principle directions were measured for strain response via TMA.

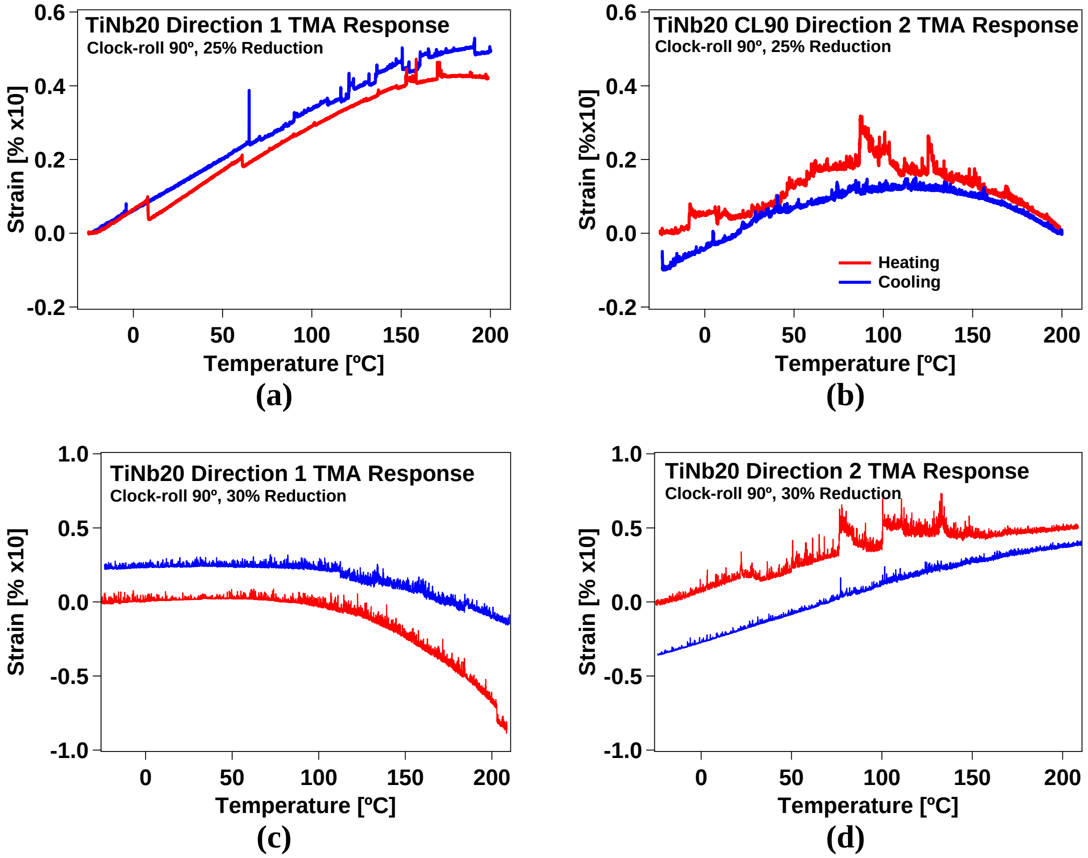

(a) (b)

(c) (d)

Figure 10.5 Summary of preliminary clock-rolling experiment. (a) and (b): TMA responses in the two directions of the 90° rotated clock rolled samples at 25% reduction. (c) and (d): TMA responses in the two directions of the 90° rotated clock rolled samples at 30% reduction.

The strain vs temperature results are illustrated in Figure 11.5(a-d). Generally, the strains witnessed in these samples are small, with some such as the B direction in 25% rolled material or the A direction in 30% rolled material displaying invar behavior within specific temperature ranges. The consequences of the mixed textures are evident in these results, however. The slopes of the strain verses temperature are not linear over much of the temperature range(s) examined. This is a result of the differential in nonlinear strain evolution between the a, b, and c axes of the martensite as was determined in Chapters V and VIII. Here, the relative lack of a-axis (due to the relatively high deformation) and comparatively constant PTE contribution from the c-axis causes the PTE component of the CTE to be mainly flat over the temperature range. This is in contrast to the b-axis, which as was previously established demonstrates an accelerating NTE value over the majority of the temperature range studied in this work. The result of this mixed microstructure is that the nonlinear contribution from the b-axis creates the variable CTE seen especially in Figure 11.5(b), where the instantaneous CTE value of the heating & cooling curves transitions from positive, to zero, to negative as a function of the temperature. It can further be postulated that the CTE below the temperature range studied would also be positive. The flatter low-temperature CTE for direction A in Figure 11.5(c) which is predicated on a larger b-axis contribution also results in a larger NTE response above 100 °C, which was the same temperature point where the CTE change occurred in the 25% rolled case for direction B. Note that when the b-axis contribution is increased in direction A, then the slope of the direction B curve is notably flatter, as can be seen when comparing Figures 11.5(a) and (d). Since both are rolled to levels well above the point where the majority of detwinning would occur, it is reasonable to assume that the differences between both samples and their directional behaviors represents mainly a difference in the balance of the b-axis contribution to each axis due to sample-to-sample variance, and not a result of different rolling amounts.

The overall performance of these clock-rolled samples is summarized and compared to linear rolled samples in Figure 11.6. The overall range of CTE observed in the clock-rolled samples is comparable to the average of the transverse and rolling directions in this composition. As previously observed, a larger NTE result would also yield a larger PTE result in the second axis. This appears to indicate that in the ideal ‘isotropic texture’ case, then the overall CTE of both axes would be slightly positive to 100 °C, and slightly negative when examined above that temperature. This is due to the necessary mixture of the b- and c-axis contributions and would likely be inherent to the response of this composition in TiNb. In $TiNb_{22}$ alloy, a single test sample prepared using the same methods outline above resulted in a slightly negative average CTE over the two directions, which seems to indicate that the ‘isotropic’ CTE value is composition rather than deformation dependent. The net CTE will, apparently, always be temperature dependent if the texture is remotely distributed evenly among all directions; this should always be a consideration in determining the suitability of such materials in future.

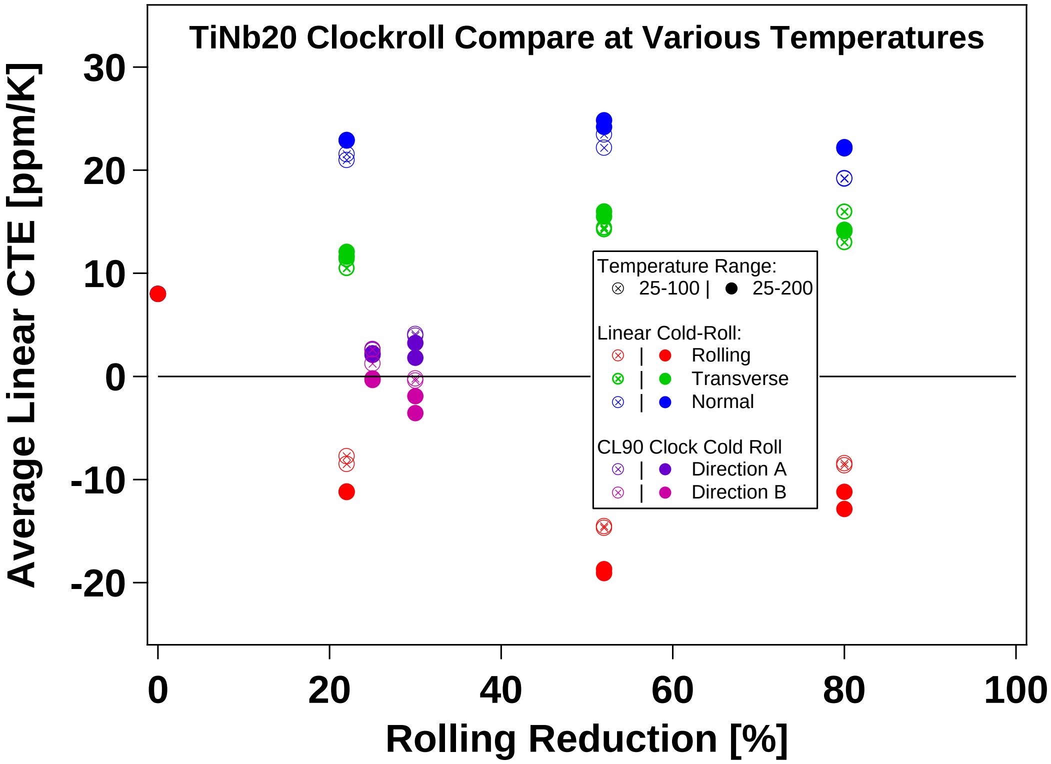

Figure 10.6 Summary for 75 and 175 °C temperature windows in the clock rolled samples compared with linear cold rolling in $TiNb_{20}$.

Other clock-rolling attempts dating from this same 2015 work using either more rolling angles or larger individual deformation steps to ease the processing requirements universally failed at producing any level of uniformity. At the time this was a mystery. However, the later tension examinations of TiNb shed light as to why this is. The rapidity of the CTE evolution observed in the linearly deformed TiNb alloys (Ch V) and low-rolled TiNb (Ch VIII) explains why only an extremely fine-step application of the most simply distributed deformation orientations is apparently the only method which results in such even distribution of the CTE. Even then, the samples demonstrated in this preliminary study have not achieved the targeted ‘isotropic’ texture evolution despite this effort. This points towards an inherent barrier in terms of ease of processing which will need to be further addressed, should the planar isotropic CTE be pursued further.

While the potential for achieving this ‘isotropic’ planar texturing of these materials appears possible, a significant amount of work is clearly required to produce consistent results. Additional examination towards a uniform planar CTE should examine two primary factors: whether there exists a more efficient method for applying relatively large deformation uniformly within a plane, and what the ultimate CTE resulting from such isotropic texture would be for multiple compositions. The most obvious area of examination for composition is the range of Nb in the TiNb system which responds well to texturability, tentatively from 17 to 25 at% Nb. However, it would additionally be informative to examine the response of NiTi with similarly ‘isotropic’ deformation, in order to determine whether the ultimate evolutions show similarity. Similar to the oriented cutting in Section 11.1, application of digital image correlation may speed analysis of the planar CTE after deformation in order to determine the responses more quickly.

REFERENCES

1. Takenaka, K., *Negative thermal expansion materials: technological key for control of thermal expansion.* Sci Technol Adv Mater, 2012. **13**(1): p. 013001.

2. Entel, P., E. Hoffmann, P. Mohn, K. Schwarz, and V.L. Moruzzi, *First-principles calculations of the instability leading to the Invar effect.* Physical Review B, 1993. **47**(14): p. 8706-8720.

3. Sumiyama, K., M. Shiga, M. Morioka, and Y. Nakamura, *Characterisitic magnetovolume effecs in Invar type Fe-Pt alloys.* Journal of Physics F: Metal Physics, 1979. **9**: p. 1665-1677.

4. Weiss, R.J., *The origin of the 'Invar' effect.* Proc. Phys. Soc., 1963. **82**: p. 281-288.

5. Kondorsky, E.I. and V.L. Sedox, *Antiferromagnetism of Iron in Face-Centered Crystalline Lattice and the Causes of Anomalies in Invar Physical Properties.* Journal of Applied Physics, 1960. **31**: p. 331-335.

6. Yokoyama, T., A. Koide, and Y. Uemura, *Local Thermal Expansions and Lattice Strains in Elinvar and Stainless Steel Alloys.* Physical Review Materials, 2018. **2**: p. 1-7.

7. Kaczkowski, Z., *Elinvar Properties of the Fe-Ni-Cr-Ti Alloys.* Physica B+C, 1988. **149**: p. 232-239.

8. Saburi, T. and C.M. Wayman, *Crystallographic Similarities in Shape Memory Martensites.* Acta Metallurgica, 1979. **27**: p. 979-995.

9. Gonzalez, C.H., N.F. de Quadros, C.J. de Araujo, and G. Guenin, *Coupled Stress-Strain and Electrical Resistivity Measurements on Copper Based Shape Memory Single Crystals.* Materials Research, 2004. **7**: p. 305-311.

10. Liu, Y., Y. Liu, and J.V. Humbeeck, *Two-way Shape Memory Effect Developed by Martensite Deformation in NiTi.* Acta Materialia, 1999. **47**: p. 199-209.

11. Liu, Y., Z.L. Xie, J.V. Humbeeck, and L. Delaey, *Effect of Texture Orientation on the Martensite Deformation of NiTi Shape Memory Alloy Sheet.* Acta Materialia, 1999. **47**: p. 645-660.

12. Lanba, A. and R.F. Hamilton, *The Impact of Martensite Deformation on Shape Memory Effect Recovery Strain Evolution.* Metallurgical And Materials Transactions A, 2015. **45**: p. 3481-3489.

13. Elmer, J.W., T.A. Palmer, S.S. Babu, and E.D. Specht, *In situ observations of lattice expansion and transformation rates of α and β phases in Ti-6Al-4V.* Materials Science and Engineering A, 2005. **391**: p. 104-113.

14. Kroeger, F.R. and C.A. Swenson, *Absolute Linear Thermal-Expansion Measurements on Copper and Aluminum from 5 to 320 K.* Journal of Applied Physics, 1977. **48**: p. 853-864.

15. Monroe, J.A., D. Gehring, I. Karaman, R. Arroyave, D.W. Brown, and B. Clausen, *Tailored thermal expansion alloys.* Acta Materialia, 2016. **102**: p. 333-341.

16. Ahadi, A., Y. Matsushita, T. Sawaguchi, Q.P. Sun, and K. Tsuchiya, *Origin of zero and negative thermal expansion in severely-deformed superelastic NiTi alloy.* Acta Materialia, 2017. **124**: p. 79-92.

17. Liu, Y., *The Superelastic Anisotropy in a NiTi Shape Memory Alloy Thin Sheet.* Acta Materialia, 2015. **95**: p. 411-427.

18. Qiu, S., B. Clausen, S.A. Padula II, R.D. Noebe, and R. Vaidyanathan, *On elastic moduli and elastic anisotropy in polycrystalline martensitic NiTi.* Acta Materialia, 2011. **59**: p. 5055-5066.

19. Brinson, L.C., *One-Dimensional Consititutive Behavior of Shape Memory Alloys: Thermomechanical Derivation with Non-Constant Material Functions and Redefined Martensite Internal Variable.* Journal of Intelligent Materials Systems and Structures, 1993. **4**: p. 229-242.

20. Friak, M., W.A. Counts, D. Ma, B. Sander, D. Holec, D. Raabe, and J. Neugebauer, *Theory-Guided Materials Design of Multi-phase Ti-Nb Alloys with Bone-Matching Elastic Properties.* Materials (Basel), 2012. **5**: p. 1853-1872.

21. Liu, Y. and H. Xiang, *Apparent Modulus of Elasticity of Near-Equiatomic NiTi.* Journal of Alloys and Compounds, 1998. **270**: p. 154-159.

22. Brill, T.M., *Elastic Properties of NiTi.* Journal of Physics : Condensed Matter, 1991. **3**: p. 9621-9627.

23. Hearmon, R.F.S., *The Elastic Constants of Anisotropic Materials.* Reviews of Modern Physics, 1946. **18**: p. 409-440.

24. Varshni, Y.P., *Temperature Dependence of the Elastic Constants.* Physical Review B, 1970. **2**: p. 3952-3958.

25. Wagner, M.F.-X. and W. Windl, *Lattice Stability, Elastic Constants and Macroscopi Moduli of NiTi Martensites from First Principles.* Acta Materialia, 2008. **56**: p. 6232-6245.

26. Cui, J. and X. Ren, *Elinvar Effect in Co-doped TiNi Strain Glass Alloys.* Applied Physics Letters, 2014. **105**: p. 1-4.

27. Wang, Y., J. Gao, H. Wu, S. Yang, X. Ding, D. Wang, X. Ren, Y. Wang, X. Song, and J. Gao, *Strain glass transition in a multifunctional β-type Ti alloy.* Scientific Reports, 2014. **4**: p. 1-5.

28. Zhang, L., D. Wang, X. Ren, and Y. Wang, *A new mechanism for low and temperature-independent elastic modulus.* Scientific Reports, 2015. **5**: p. 1-12.

29. Monroe, J.A., *Unusual Functionalities in Shape Memory Alloys.* 2013.

30. Wassermann, E.F., *The Invar Problem.* Journal of Magnetism and Magnetic Materials, 1991. **100**: p. 346-362.

31. Arvanitidis, J., K. Papagelis, S. Margadonna, K. Prassides, and A.N. Fitch, *Temperature-induced valence transition and associated lattice collapse in samarium fulleride.* Nature, 2003. **425**: p. 599-602.

32. Evans, J.S.O., T.A. Mary, T. Vogt, M.A. Subramanian, and A.W. Sleight, *Negative Thermal Expansion in ZrW2O8 and HfW2O8.* Chemistry of Materials, 1996. **8**: p. 2809-2823.

33. Mary, T.A., J.S.O. Evans, T. Vogt, and A.W. Sleight, *Negative thermal expansion from 0.3 to 1050 Kelvin in ZrW2O8.* Science, 1996. **272**: p. 90-92.

34. Sleight, A.W., *Thermal contraction.* Nature, 1997. **389**: p. 923-924.

35. Sleight, A.W., *Thermal Contraction.* Endeavour, 1995. **19**: p. 64-68.

36. Sleight, A.W., *Compounds that contract on heating.* Inorganic Chemistry, 1998. **37**: p. 2854-2860.

37. Schelling, P.K. and P. Keblinski, *Thermal expansion of carbon structures.* Physical Review B, 2003. **68**: p. 1-7.

38. Srikanth, V., E.C. Subbarao, D.K. Agrawal, C.-Y. Huang, and R. Roy, *Thermal Expansion Anisotropy and Acoustic Emission of NaZr2P3O12 Family Ceramics.* Journal of the Americal Ceramic Society, 1991. **74**: p. 365-368.

39. Qiu, S., V.B. Krishnan, S.A. Padula, R.D. Noebe, D.W. Brown, B. Clausen, and R. Vaidyanathan, *Measurement of the lattice plane strain and phase fraction evolution during heating and cooling in shape memory NiTi.* Applied Physics Letters, 2009. **95**(14): p. 141906.

40. Lloyd, L.T. and C.S. Barrett, *Thermal expansion of alpha uranium.* Journal of Nuclear Materials, 1966. **18**: p. 55-59.

41. Bourke, M.A.M., D.C. Dunan, and E. Ustundag, *SMARTS – a spectrometer for strain measurement in engineering materials.* Applied Physics A, 2002. **74**: p. 1707-1709.

42. Von Dreele, R.B., J.D. Jorgensen, and C.G. Windsor, *Rietveld refinement with spallation neutron powder diffraction data.* Journal of Applied Crystallography, 1982. **15**: p. 581-589.

43. Schlenker, J.L. and G.V. Gibbs, *Thermal-expansion coefficients for Monoclinic Crystals: A Phenomenological Approach.* The American Minerologist, 1975. **60**: p. 828-833.

44. Dogan, E., I. Karaman, N. Singh, A. Chivukila, H.S. Thawabi, and R. Arroyave, *The effect of electronic and magnetic valences on the martensitic transformation of CoNiGa shape memory alloys.* Acta Materialia, 2012. **60**: p. 3545-3558.

45. Kim, H.Y., Y. Ikehara, J.I. Kim, H. Hosoda, and S. Miyazaki, *Martensitic transformation, shape memory effect and superelasticity of Ti–Nb binary alloys.* Acta Materialia, 2006. **54**: p. 2419-2429.

46. Monroe, J.A., I. Karaman, D.C. Lagoudas, G. Bigelow, R.D. Noebe, and S. Padula, *Determining recoverable and irrecoverable contributions to accumulated strain in a NiTiPd high-temperature shape memory alloy during thermomechanical cycling.* Scripta Materialia, 2011. **65**(2): p. 123-126.

47. Bigelow, G., S.A. Padula II, A. Garg, D. Gaydosh, and R.D. Noebe, *Characterization of Ternary NiTiPd High-Temperature Shape-Memory Alloys under Load-Biased Thermal Cycling.* Metallurgical And Materials Transactions A, 2010. **41A**(3065-3079).

48. Bucsek, A.N., G.A. Hudish, G. Bigelow, R.D. Noebe, and A.P. Stebner, *Composition, Compatability, and the Functional Performances of Ternary NiTiX High-Temperature Shape Memory Alloys.* Shape Memory and Superelasticity, 2016. **2**: p. 62-79.

49. Rehman, S., M. Khan, N.A. Khan, S.H.I. Jaffery, L. Ali, and A. Mabashar, *Improvement in the Mechanical Properties of High Temperature Shape Memory Alloy (TiNiPd) by Copper Addition.* Advances in Materials Science and Engineering, 2015. **2015**: p. 1-7.

50. Atli, K.C., *Thermomechanical Cyclic Response of TiNiPd High-Temperature Shape Memory Alloys.* 2011.

51. Jefferson, G., T.A. Parthasarathy, and R.J. Kerans, *Tailorable thermal expansion hybrid structures.* International Journal of Solids and Structures, 2009. **46**(11-12): p. 2372-2387.

52. Khromova, L.P., N.B. Dyakonova, Y.L. Rodionov, G.V. Yudin, and I. Korms, *Martensitic transformations, thermal expansion and mechanical properties of titanium-niobium alloys.* J. Phys. IV France, 2003. **112**: p. 1051-1054.

53. Gehring, D., J.A. Monroe, and I. Karaman, *Effects of Composition on the Mechanical Properties and Negative Thermal Expansion in martensitic TiNb Alloys.* Scripta Materialia, 2019. **178**: p. 351-355.

54. Bonisch, M., A. Panigrahi, M. Stoica, M. Calin, E. Ahrens, M. Zehetbauer, W. Skrotzki, and J. Eckert, *Giant thermal expansion and alpha-precipitation pathways in Ti-alloys.* Nat Commun, 2017. **8**(1): p. 1429.

55. Panico, M. and L.C. Brinson, *A three-dimensional phenomenological model for martensite reorientation in shape memory alloys.* Journal of the Mechanics and Physics of Solids, 2007. **55**(11): p. 2491-2511.

56. Arghavani, J., F. Auricchio, R. Naghdabadi, A. Reali, and S. Sohrabpour, *A 3-D phenomenological constitutive model for shape memory alloys under multiaxial loadings.* International Journal of Plasticity, 2010. **26**(7): p. 976-991.

57. Sittner, P. and V. Novak, *Anisotropy of Martensitic Transformations in Modeling of Shape Memory Alloy Polycrystals.* International Journal of Plasticity, 2000. **16**: p. 1243-1268.

58. Bönisch, M., M. Calin, L. Giebeler, A. Helth, A. Gebert, W. Skrotzki, and J. Eckert, *Composition-dependent magnitude of atomic shuffles in Ti–Nb martensites.* Journal of Applied Crystallography, 2014. **47**(4): p. 1374-1379.

59. Liu, Z.-K., Y. Wang, and S.-L. Shang, *Origin of negative thermal expansion phenomenon in solids.* Scripta Materialia, 2011. **65**: p. 664-667.

60. Jones, Z.A., P. Sarin, P. Haggerty, and W.M. Kriven, *CTEAS: a graphical-user-interface-based program to determine thermal expansion from hightemperature X-ray diffraction.* Journal of Applied Crystallography, 2013. **46**: p. 550-553.

61. Alexander, S. and J. McTague, *Should All Crystals Be bcc? Landau Theory of Solidification and Crystal Nucleation.* Physical Review Letters, 1978. **41**(10): p. 702-705.

62. Bai, X.-M. and M. Li, *Calculation of solid-liquid interfacial free energy: A classical nucleation theory based approach.* J. Chem. Phys., 2006. **124**(124707): p. 1-12.

63. Hunt, J.D. and K.A. Jackson, *Nucleation of Solid in an Undercooled Liquid by Cavitation.* Journal of Applied Physics, 1966. **37**: p. 254-257.

64. Kibey, S., H. Sehitoglu, and D.D. Johnson, *Energy landscape for martensitic phase transformationin shape memory NiTi.* Acta Materialia, 2009. **57**: p. 1624-1629.

65. Zhang, J.M. and G.Y. Guo, *Microscopic Theory of the Shape Memory Effect in TiNi.* Physical Review Letters, 1997. **78**(25): p. 4789-4792.

66. Ye, Y.Y., C.T. Chan, and K.M. Ho, *Structural and electronic properties of the martensitic alloys TiNi, TiPd, and TiPt.* Physical Review B, 1997. **56**(7): p. 3678-3689.

67. Kim, H.Y., H. Satoru, J.I. Kim, H. Hosoda, and S. Miyazaki, *Mechanical Properties and Shape Memory Behavior of Ti-Nb Alloys.* Materials Transactions, 2004. **45**(7): p. 2443-2448.

68. Mainprice, D., R. Hielscher, and H. Schaeben, *Calculating anisotropic physical properties from texture data using the MTEX open-source package.* Deformation Mechanisms, Rheology and Tectonics: Microstructures, Mechanics and Anisotropy, 2011. **360**: p. 175-192.

69. Pelton, A.R., B. Clausen, and A.P. Stebner, *In Situ Neutron Diffraction Studies of Increasing Tension Strains of Superelastic Nitinol.* Shape Memory and Superelasticity, 2015. **1**: p. 375-386.

70. Paranjape, H.M., P.P. Paul, B. Amin-Ahmadi, H. Sharma, D. Dale, J.Y.P. Ko, Y.I. Chumlyakov, L.C. Brinson, and A.P. Stebner, *In Situ, 3D Characterization of the deformation mechanics of a superelastic NiTi shape memory alloy single crystal under multiscale constraint.* Acta Materialia, 2018. **144**: p. 748-757.

71. Ishida, A., M. Sato, T. Kimura, and S. Miyazaki, *Stress-strain curves of sputter-deposited Ti-Ni thin films.* Philosophical Magazine A, 2000. **80**(4): p. 967-980.

72. Karaman, I., H.E. Karaca, H.J. Maier, and Z.P. Luo, *The Effet of Severe Marforming on Shape Memory Characteristics of a Ti-Rich NiTi Alloy Processed Using Equal Channel Angular Extrusion.* Metallurgical And Materials Transactions A, 2003. **34A**: p. 2527-2539.

73. Liu, Y., Z. Xie, J. Van Humbeeck, and L. Delaey, *Asymmetry of Stress-Strain Curves Under Tension and Copression for NiTi Shape Memory Alloys.* Acta Materialia, 1998. **46**(12): p. 4325-4338.

74. Benafan, O., S.A. Padula, R.D. Noebe, T.A. Sisneros, and R. Vaidyanathan, *Role of B19' martensite deformation in stabilizing two-way shape memory behavior in NiTi.* Journal of Applied Physics, 2012. **112**(9): p. 093510.

75. Madangopal, K. and R. Banerjee, *THE LATTICE INVARIANT SHEAR IN NI-Ti SHAPE MEMORY ALLOY MARTENSITES* SCRIPTA METALLURGICA ET MATERIALIA, 1992. **27**: p. 1627-1632.

76. Zhang, J.X., M. Sato, and A. Ishida, *Deformation mechanism of martensite in Ti-rich Ti–Ni shapememory alloy thin films.* Acta Materialia, 2006. **54**: p. 1185-1198.

77. Ezaz, T., H. Sehitoglu, and H.J. Maier, *Energetics of twinning in martensitic NiTi.* Acta Materialia, 2011. **59**: p. 5893-5904.

78. Xie, Z., Y. Liu, and J. Van Humbeeck, *MICROSTRUCTURE OF NiTi SHAPE MEMORY ALLOY DUE TO TENSION±COMPRESSION CYCLIC DEFORMATION.* Acta Materialia, 1998. **46**: p. 1989-2000.

79. Nishida, M., S. Ii, K. Kitamura, T. Furukawa, A. Chiba, T. Hara, and K. Hiraga, *NEW DEFORMATION TWINNING MODE OF B19*MARTENSITE IN Ti-Ni SHAPE MEMORY ALLOY.* Scripta Materialia, 1998. **39**(12): p. 1749-1754.

80. Merklein, M. and A. Kuppert, *A METHOD FOR THE LAYER COMPRESSION TEST CONSIDERING THE ANISOTROPIC MATERIAL BEHAVIOR* International Journal of Material Forming, 2009. **2**: p. 483-486.

81. Zhuang, X., Z. Zhao, H. Li, and H. Xiang, *Experimental Methodology for Obtaining the Flow Curve of Sheet Materials in a Wide Range of Strains.* Steel Research International, 2013. **84**(2): p. 146-154.

82. Lee, H.-J. and A.G. Ramirez, *Crystallization and phase transformations in amorphous NiTi thin films for microelectromechanical systems.* Applied Physics Letters, 2004. **85**(7): p. 1146-1148.

83. Liu, Y. and D. Favier, *Stabilization of Martensite due to Shear Deformation via Variant Reorientation in Polycrystalline NiTi.* Acta Materialia, 2000. **48**: p. 3489-3499.

84. Abdel-Hady, M. and M. Morinaga, *Controlling the thermal expansion of Ti alloys.* Scripta Materialia, 2009. **61**: p. 825-827.

85. Hao, Y.L., H.L. Wang, T. Li, J.M. Cairney, A.V. Ceguerra, Y.D. Wang, Y. Wang, D. Wang, E.G. Obbard, S.J. Li, and R. Yang, *Superelasticity and Tunable Thermal Expansion across a WideTemperature Range.* journal of Materials Science and Technology, 2016. **32**: p. 705-709.

86. Kim, H.Y., L. Wei, S. Kobayakshi, M. Tahara, and S. Miyazaki, *Nanodomain structure and its effect on abnormal thermalexpansion behavior of a Ti–23Nb–2Zr–0.7Ta–1.2O alloy.* Acta Materialia, 2013. **61**: p. 4874-4886.

87. Wei, L.S., H.Y. Kim, and S. Miyazaki, *Effects of oxygen concentration and phase stability on nano-domainstructure and thermal expansion behavior of Ti–Nb–Zr–Ta–O alloys.* Acta Materialia, 2015. **100**: p. 313-322.

88. Huang, X., G.J. Ackland, and K.M. Rabe, *Crystal structures and shape-memory behaviour of NiTi.* Nature Materials, 2003. **2**: p. 307-311.

89. Sehitoglu, H., J. Jun, X. Zhang, I. Karaman, Y. Chumlyakov, H.J. Maier, and K. Gall, *SHAPE MEMORY AND PSEUDOELASTIC BEHAVIOR OF51.5%Ni–Ti SINGLE CRYSTALS IN SOLUTIONIZED AND OVERAGED STATE.* Acta Materialia, 2001. **49**: p. 3609-3620.

90. Ma, J., B. Kockar, A. Evirgen, I. Karaman, Z.P. Luo, and Y.I. Chumlyakov, *Shape memory behavior and tension–compression asymmetryof a FeNiCoAlTa single-crystalline shape memory alloy.* Acta Materialia, 2012. **60**: p. 2186-2195.

91. Evirgen, A., I. Karaman, R. Santamarta, J. Pons, and R.D. Noebe, *Microstructural characterization and shape memory characteristics of theNi50.3Ti34.7Hf15shape memory alloy.* Acta Materialia, 2015. **83**: p. 48-60.

92. Molnar, P., P. Sittner, V. Novak, and P. Lukas, *Twinning processes in Cu–Al–Ni martensite single crystals investigatedby neutron single crystal diffraction method.* Materials Science and Engineering A, 2008. **481-482**: p. 513-517.

93. Molnar, P., P. Sittner, P. Lukas, S.-P. Hannula, and O. Heczko, *Stress-induced martensite variant reorientation in magnetic shape memory Ni–Mn–Ga single crystal studied by neutron diffraction.* Smart Materials and Structures, 2008. **17**: p. 1-5.

94. Knezevic, M., L. Capoungo, C.N. Tome, R.A. Lebensohn, D.J. Alexander, B. Mihaila, and R.J. McCabe, *Anisotropic stress–strain response and microstructure evolutionof textureda-uranium.* Acta Materialia, 2012. **60**: p. 702-715.

95. Lebensohn, R.A. and C.N. Tome, *A self-consistent viscoplastic model: prediction of rolling textures of anisotropic polycrystals* Materials Science and Engineering A, 1994. **175**: p. 71-82.

96. Calhoun, C.A., E. Garlea, R.P. Mulay, T.A. Sisneros, and S.R. Agnew, *Investigation of the effect of thermal residual stresses on deformationofa-uranium through neutron diffraction measurements and crystalplasticity modeling.* Acta Materialia, 2015. **85**: p. 168-179.

97. Brown, D.W., M.A.M. Bourke, B. Clausen, R.C. Korzekwa, R.J. McCabe, T.A. Sisneros, and D.F. Teter, *Temperature and direction dependence of internal strain and texture evolutionduring deformation of uranium.* Materials Science and Engineering A, 2009. **512**: p. 67-75.

APPENDIX

ADJUSTMENT OF STRESS AND STRAIN IN ITERATED TENSION

Examining the approximate stress and strain experienced by the tension sample during discreet deformation (prestrain) steps is somewhat difficult. As the sample cannot be accessed, then it does not become possible to re-evaluate the new length and cross-sectional area of the sample after each deformation step. The only known dimension are the pre-deformed length and area measurements, but if these were to be used through the whole length of the sample's deformation (essentially, reporting all factors in engineering stress and strain terms), then this will fatally misreport the final CTE and elastic properties of the sample. In my literature review into this topic, I am aware of at least one peer-reviewed work on NiTi elastic properties which was published with this mistake baked-in [21]. The reason why such a mistake is so important is because (1) due to the longer sample, higher incremental change in extensometer separation occurs for a given % strain change and (2) the decreasing sample area means that the stress experienced for a given load is higher by some amount. If uncorrected, this will lead to the observed CTE being over-reported as the denominator in the strain term is too small; the engineering elastic modulus will also be much less than the real elastic modulus as the change in stress is less than actual, along with the change in strain in the denominator being too large.

As the sample's change in cross-section cannot be measured during deformation, to enable a usable estimate for the stress it has been assumed that the cross-sectional area of the sample decreases uniformly – that is to say that the proportions of the two dimensions in the cross-sectional plane will retain their original aspect ratio. Observation of post-fracture samples in NiTi and NiTiPdTa indicate that this assumption is reasonable for these alloys, while TiNb does not maintain a uniform cross section at strains above 20% where slip dominates. This problem is mitigated somewhat by the reduced interest in further pursuing measurement of elastic modulus in iteratively deformed TiNb (see Ch V addendum).

To derive new estimates for stress and strain, we begin with the fundamental forms of each equation, $\sigma = \frac{F}{A};\ \varepsilon = \frac{\Delta l}{l_0}$. To calculate CTE, the strain equation is modified by averaging the change in strain over the change in temperature, or $CTE = \frac{\Delta l}{l_0} * \frac{1}{\Delta T} = \frac{(l - l_0)}{l_0 \Delta T}$ where l is the instantaneous sample length. This represents the engineering CTE. To correct for the new sample length the amount of deformation should be factored in. This can be introduced with one of two forms: the prestrain amount (the maximum elastic + plastic deformation for that step), or the plastic strain (the total strain following unloading of the sample after deformation). While both can be valid for this approach, this author prefers and has used exclusively the stepwise plastic strain, as this is the starting value at which the heating/cooling steps will be applied. To integrate the new sample length, the sample length is multiplied by one plus the plastic strain value, yielding $\varepsilon_{LS} = \frac{(l - \{l_0 * [1 + \varepsilon_p]\})}{\{l_0 * [1 + \varepsilon_p]\}}$ and $CTE_{LS} = \frac{(l - \{l_0 * [1 + \varepsilon_p]\})}{\{l_0 * [1 + \varepsilon_p]\} \Delta T}$. LS is short for ‘linear strain,’ which reflects how the adjusted strain changes in linear proportion to the plastic strain value applied to the sample. Note that is not proportional to the true strain, which expects a monotonically increasing strain value. As seen in Figure B-1, the net effect of this model for CTE is a linear reduction compared to the engineering value which better reflects the current sample conditions, as otherwise the measured CTE would continue to increase infinitely.

To derive the corrected stress, the proportional-area assumption above is invoked in order to redefine the cross-sectional area as a function of the sample length, where the change in the area of the sample will also be proportional to the elongation of the sample due to conservation of volume. Therefore, the original area A is now redefined as A_0, and the area at any given value of plastic strain is now given as $A = \frac{A_0}{(1+\varepsilon_p)}$. Integrating into the stress equation above, this results in the corrected stress becoming $\sigma_{LS} = \frac{F*(1+\varepsilon_p)}{A_0}$, again using LS to denote that it is part of this same correction model.

To determine the elastic modulus measured from raw data, the Young's modulus equation $E = \frac{\sigma}{\varepsilon}$ must now be suitably modified. Combining the LS corrected terms for both stress and strain, the result becomes $E_{LS} = \frac{F*(1+\varepsilon_p)}{A_0} * \frac{\{l_0*[1+\varepsilon_p]\}}{(l-\{l_0*[1+\varepsilon_p]\})} = \frac{F l_0 (1+\varepsilon_p)}{A_0(l-\{l_0*[1+\varepsilon_p]\})}$, whose comparison with the engineering values measured in an experiment are also shown in Figure A.1. The adjusted elastic modulus relative to the engineering value will increase at a rate approximately of strain to the second power and reflects the influence of the rapidly decreasing cross-sectional area. Since no sample in this work exceeded 42% strain at failure, the maximum elastic modulus adjustment required in this work was a doubling of the measured engineering elastic modulus rather than the maximum quadrupling predicted for super-plasticity to 100% deformation strain.

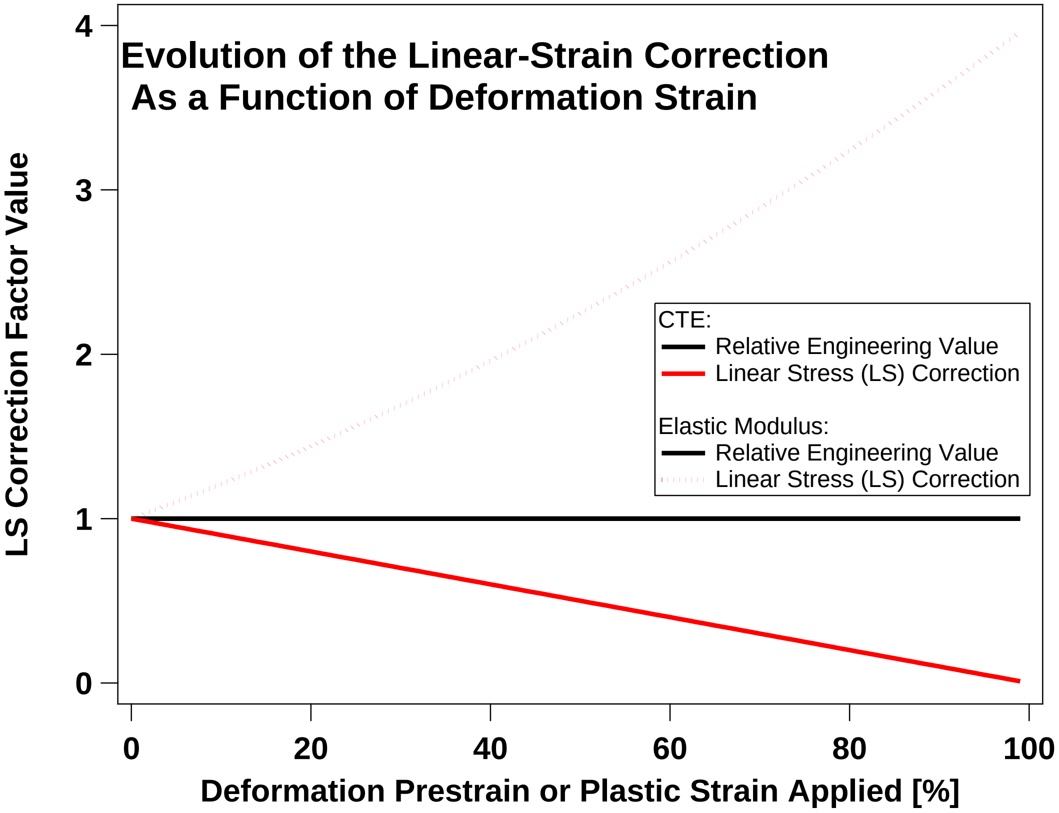

Figure A.1 Illustration of the relative difference between raw adjusted data.

One benefit to a sign change in the data is that this is not affected by the frame of reference, so that both zero CTE and NTE results are always so; the only real question that required addressing in this conversion is the ultimate magnitude of both NTE and PTE responses, as well as elastic modulus. The above work illustrates how the stress, strain, CTE, and elastic moduli were estimated from raw data in the iterative tension tests described in various chapters in order to compensate for changes in the sample dimensions, and thus allow for more accurate reporting.

VITA

Dominic F. Gehring is a recipient of a 2012 B.S. degree in nuclear engineering from Purdue University, West Lafayette, Indiana. He enrolled to study Materials Science and Engineering at Texas A&M University in 2014, moving from the M.S. pathway to a direct Ph.D course of study after invitation to perform research in the MESAM research group under Prof. Dr. Ibrahim Karaman. Mr. Gehring has in his time at Texas A&M worked under a variety of assistantships, including both research and teaching responsibilities. He has also been involved in the service towards and administration of several department- and university-level organizations. Notable accomplishments during this time include the publication of three peer-reviewed journal articles at time of dissertation submission with additional manuscripts in preparation, giving four conference presentations on his research, acceptance to perform tests at Argonne National Lab twice, participating in the course design for MSEN 302, and being invited to act as a graduate teaching fellow for MSEN/MEEN 222. His permanent address is:

Department of Materials Science and Engineering
c/o Dr. Ibrahim Karaman
Texas A&M University
College Station, TX 77843-3003
Email: dgehringne@gmail.com